Aquarius Salinity Retrieval Algorithm

Algorithm Theoretical Basis Document (ATBD)

End of Mission Version

Authors: Thomas Meissner[1], Frank Wentz[1] and David Le Vine[2]

[1]Remote Sensing Systems, Santa Rosa, CA

[2]Goddard Space Flight Center, Greenbelt, MD

Prepared for

Aquarius Data Processing System

Aquarius Science and Cal/Val Teams

Remote Sensing Systems

444 Tenth Street, Suite 200, Santa Rosa, CA 95401 (707) 545-2904

Aquarius Salinity Retrieval Algorithm

End of Mission ATBD

Thomas Meissner, Frank Wentz and David Le Vine

12/01/2017

Table of Contents

List of Figures

List of Tables

1. Introduction and Outline

This document provides the theoretical basis for the Aquarius Version 5.0 salinity retrieval algorithm. The inputs to the algorithm are the RFI filtered Aquarius radiometer antenna temperature measurements (called TF in the Aquarius Level 2 files), the Aquarius scatterometer backscatter measurements (σ_0) along with a number of operational oceanographic and meteorological products from NCEP and CMC (Canadian Meteorological Center) , land and sea ice masks and precomputed tables of space radiation coming from the galaxy and sun. The output is sea-surface salinity (SSS) and many intermediate variables required for the salinity calculation.

A large number of post-launch adjustments have been made since the pre-launch algorithm (Wentz and Le Vine, 2011). These are documented in a series of Addenda (Aquarius ATDB Addendum I – V) which were issued with the release of each version of the salinity product and describe the changes made and included in that version of the product. Because the Project has ended and because Version 5.0 will be the final product, it was decided to rewrite the ATBD to represent the final version, Version 5.0, of the salinity retrieval algorithm. That is this document. It is the end of mission version of the ATBD and describes the algorithm used to obtain the final salinity product under the Aquarius project, Version 5.0.

The salinity retrieval ATBD is organized as follows:

The Forward Model (Section 2) describes how the Aquarius antenna temperature (T_A) is calculated given as input the following information:

1. Footprint location: time, latitude, and longitude.
2. Pointing angles: Earth incidence and azimuth angles; sun and moon pointing vectors.
3. Antenna patterns.
4. The Aquarius scatterometer backscatter cross-section (σ_0), which is used to derive an ancillary Aquarius wind speed W for the surface roughness correction.
5. An external reference salinity field (see Section 4.8).

6. Operational fields from CMC (sea surface temperature), NCEP (wind direction, atmospheric profiles for pressure, temperature, humidity and liquid water), land mask and sea ice mask.
7. Solar flux values from radio astronomy observations.
8. Pre-computed tables giving the TA contribution of the galaxy and sun (the moon contribution is computed from an analytic expression).

The Retrieval Algorithm (Section 3) describes how the various components of the forward model are used to estimate salinity given the Aquarius T_A measurement. The algorithm is essentially a subtraction process in which the unwanted sources of signal (galaxy, sun, moon, Earth's ionosphere, Earth's atmosphere, and ocean surface roughness) are removed from the T_A measurement in order to obtain just the emission term from a flat ocean surface. A maximum likelihood estimator (MLE) then used to estimate salinity from the surface emission.

The ancillary data fields that are used in the forward model and in the salinity retrieval algorithm are listed and briefly discussed in Section 4.

Because of the complexity of the subjects we have devoted separate sections to the surface roughness correction and the reflection of galactic radiation from rough ocean surfaces.

Section 5 describes the details of the surface roughness correction, which is one of the most important parts in the forward modeling and in the salinity retrieval algorithm. One crucial component in the surface roughness correction is the derivation of an ancillary wind speed from Aquarius scatterometer observations.

Section 6 describes the details of the computation of the reflected galactic radiation from rough ocean surfaces.

The pre-launch instrument parameters (e.g. antenna pattern; noise diode effective temperature) were not known accurately enough for the level of calibration needed to retrieve salinity. Furthermore, especially in the early months of the mission, the Aquarius radiometers drifted slightly (partly due to outgassing). To address these issues, the average salinity over the global ocean provided by in situ sensors (e.g. Argo floats) was used as a calibration reference. This is described in Section 7.

Section 8 explains how formal uncertainty estimates are associated with the Aquarius salinity retrievals. The formal uncertainty estimation is based on:

1. Identification of the relevant sources of error in the salinity retrieval algorithm.
2. Calculation of the sensitivity of the Aquarius salinity retrieval to these sources of error.

2. Forward Model

The forward model begins with known salinity and external sources (e.g. Sun and Moon) and computes the Aquarius antenna temperature in terms of the antenna pattern G convolved with the surrounding brightness temperatures, T_B (Le Vine et al., 2011). The brightness temperature incident at the antenna is partitioned into a space segment (sources not on the Earth) and an Earth segment (Le Vine et al., 2011).

Figure 1 displays a schematic flow diagram for the forward model.

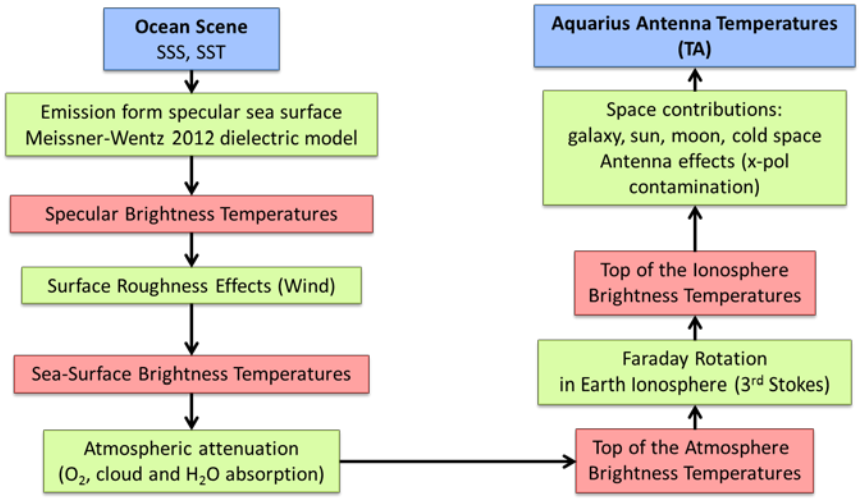

Figure 1: Schematic flow diagram for the forward model.

2.1 The Antenna Temperature Equation

In this subsection, we work in terms of the classical, rather than the modified Stokes parameters (i.e. Stokes parameters in brightness temperature, Randa et al., 2008; Piepmeier et al., 2008). The measurement vector $\mathbf{T}_{\mathbf{A},mea}$, which is called the antenna temperature vector, is then defined as:

$$\mathbf{T}_{\mathbf{A}.mea} \equiv \begin{bmatrix} T_{A1,mea} \\ T_{A2,mea} \\ T_{A3,mea} \\ T_{A4,mea} \end{bmatrix} = \begin{bmatrix} T_{Amea,V} + T_{Amea,H} \\ T_{Amea,V} - T_{Amea,H} \\ T_{Amea,+45} - T_{Amea,-45} \\ T_{Amea,left} - T_{Amea,right} \end{bmatrix} \tag{1}$$

where $T_{Amea,V}$, $T_{Amea,H}$, $T_{Amea,+45}$, $T_{Amea,-45}$, $T_{Amea,left}$, and $T_{Amea,right}$ are the V-pol, H-pol, plus 45°, minus 45°, left circular, and right circular polarization measurements. Aquarius only measures

$T_{Amea,V}$, $T_{Amea,H}$, $T_{Amea,+45}$, and $T_{Amea,-45}$, (Le Vine et al., 2007b) but the full Stokes formulation is included here for completeness. Likewise, brightness temperatures are defined as

$$\mathbf{T_B} \equiv \begin{bmatrix} T_{B1} \\ T_{B2} \\ T_{B3} \\ T_{B4} \end{bmatrix} = \begin{bmatrix} T_{B,V} + T_{B,H} \\ T_{B,V} - T_{B,H} \\ T_{B,+45} - T_{B,-45} \\ T_{B,left} - T_{B,right} \end{bmatrix} \tag{2}$$

The measurements represent an integration over the entire 4p steradians surrounding the antenna. We divide this integration into 2 components: the Earth field of view and the space field of view.

$$\mathbf{T}_{\mathbf{A},mea} = \mathbf{T}_{\mathbf{A},earth} + \mathbf{T}_{\mathbf{A},space} \tag{3}$$

$$\mathbf{T}_{\mathbf{A},earth} = \frac{1}{4\pi} \int_{Earth} \mathbf{G}(\mathbf{b}) \boldsymbol{\Psi}(\phi) \mathbf{T}_{\mathbf{B},toa} \frac{\partial \Omega}{\partial A} dA \tag{4}$$

$$\mathbf{T}_{\mathbf{A},space} = \frac{1}{4\pi} \int_{Space} \mathbf{G}(\mathbf{b}) \mathbf{T}_{\mathbf{B},space} d\Omega \tag{5}$$

The first integral is over the surface of the earth visible to the sensor, where the differential surface area is dA. The second integral is over space (everything else), where $d\Omega$ is the differential solid angle. The matrix **G** is a 4´ 4 matrix describing the antenna gain function (see Le Vine et al., 2007a for an example of the gain matrix in the case of the modified Stokes parameters and Piepmeier et al., 2008 in the case of classical Stokes parameters.). Each element in this matrix is a function of the look direction **b.** For the first integral, **b** is the unit vector pointing from the antenna to *dA.* For the second integral, **b** is the unit vector in the direction specified by $d\Omega$.

The term $\boldsymbol{\Psi}(\phi)$ in (4) is a rotation matrix defined by

$$\boldsymbol{\Psi}(\phi) = \begin{bmatrix} 1 & 0 & 0 & 0 \\ 0 & \cos 2\phi & -\sin 2\phi & 0 \\ 0 & \sin 2\phi & \cos 2\phi & 0 \\ 0 & 0 & 0 & 1 \end{bmatrix} \tag{6}$$

The rotation angle ϕ is the sum of the antenna polarization angle ϕ_{ant} and the Faraday rotation angle ϕ_f due to the ionosphere: $\phi = \phi_{ant} + \phi_f$. The angle ϕ_{ant} is the angle between the polarization vectors defined at the antenna and the polarization vectors defined for radiometry at the Earth surface where **b** intersects the surface. It is an implicit function of **b** as well as the attitude of the Aquarius spacecraft. The Faraday rotation angle ϕ_f is a function of **b** as well as the Earth's magnetic field vector **B** and the electron density along the path **b-** and to a good approximation (Le Vine and Abraham, 2002):

$$\phi_f = \frac{1.35493\times10^{-5}}{\nu^2}\cdot\left(-\mathbf{b}\cdot\mathbf{B}\right)\cdot N_e\cdot\frac{\partial b}{\partial h} \tag{6}$$

where n is frequency in GHz, N_e is vertically-integrated electron counts in TEC units, **B** is the Earth's magnetic field vector in nanotesla units at the mean height of the ionosphere, and the last term is the partial derivative of slant range to the vertical height, which converts N_e from a vertically-integrated value to a slant-range integrated value. For a flat Earth surface $\frac{\partial b}{\partial h} = \sec\left(\theta_i\right)$, where θ_i is the incidence angle. The rotation matrix (6) is not required for the space integration (5) because we assume the space radiation is unpolarized.

The ratio of the differential solid angle to the differential surface area is

$$\frac{\partial\Omega}{\partial A} = f_{lat}\frac{\cos\theta_i}{r^2} \tag{7}$$

where θ_i is the incidence angle and r is the range. For a spherical Earth, the leading term f_{lat} would be unity. However, the Earth is modeled as an oblate spheroid and as a consequence this term is a function of latitude, deviating about ±1% from unity.

The brightness temperature vector for Earth in equation (4) is

$$\mathbf{T}_{\mathbf{B},toa} = \begin{bmatrix} T_{BV,toa} + T_{BH,toa} \\ T_{BV,toa} - T_{BH,toa} \\ 0 \\ 0 \end{bmatrix} \tag{8}$$

where $T_{BV,toa}$ and $T_{BH,toa}$ are the V-pol and H-pol Earth brightness temperatures measured at the top of the atmosphere (TOA), but below the ionosphere. We have assumed that the 3rd and 4th Stokes parameters coming from the Earth are negligibly small at 1.4 GHz.

The brightness temperature vector for space is

$$\mathbf{T}_{\mathbf{B},space} = \begin{bmatrix} 2T_{Bspace} \\ 0 \\ 0 \\ 0 \end{bmatrix} \tag{9}$$

The space contribution consists of cosmic background radiation, galactic radiation, and direct rays from the sun and the moon. We assume the space radiation is unpolarized in which case only the 1st Stokes parameter is non-zero. Section 2.2 discusses this space contribution in more detail.

The Earth's limb also contributes to the radiation received by the antenna. The Earth's limb varies from 260 K at the surface to 11 K at 10 km. Above 40 km, the limb brightness temperature is less than 0.001 K. When integrated over the antenna pattern, the limb contributes only 0.006 K to the 1st Stokes and is essentially zero for the 2nd through 4th Stokes.

At this point in the analysis, we drop the 4th Stokes from the notation. Aquarius does not measure the 4th Stokes, and it does not need to be considered. So, hereafter, all $\mathbf{T_A}$ and $\mathbf{T_B}$ vectors now have just 3 components, and the antenna gain matrix and rotation matrix are 3 by 3.

2.2 Radiation from Space

Space radiation consists of celestial radiation (the cosmic microwave background CMB (2.73 K) and galactic and extra-galactic radiation), and radiation from the Sun and Moon. This radiation is received by the antenna in two ways: directly and via reflection and scattering from the Earth surface. The contribution of direct lunar radiation is negligible. However, lunar radiation reflecting off the ocean surface is not negligible because at certain times each month the reflected ray enters the antenna mainbeam (Dinnat et al. 2009).

These space radiation terms are denoted by:

1. Direct and reflected celestial radiation: $\mathbf{T}_{\mathbf{A},gal\_dir}$ and $\mathbf{T}_{\mathbf{A},gal\_ref.}$

2. Direct, reflected, and backscatter solar radiation: $\mathbf{T}_{\mathbf{A},sun\_dir}$, $\mathbf{T}_{\mathbf{A},sun\_ref}$, and $\mathbf{T}_{\mathbf{A},sun\_bak}$.

3. Reflected lunar radiation: $\mathbf{T}_{\mathbf{A},mon\_ref}$.

Because the solar radiation is so intense, one must consider both the specular reflected component that enters the sidelobes of the antenna and the backscatter component that enters the mainbeam of the antenna at certain times of the year when the footprint of the main beam is not in darkness (Dinnat and Le Vine 2008).

Given these 6 terms, equations (4) and (5) can be partitioned as

$$\mathbf{T}_{\mathbf{A},earth} = \mathbf{T}_{\mathbf{A},earth\_dir} + \mathbf{T}_{\mathbf{A},gal\_ref} + \mathbf{T}_{\mathbf{A},sun\_ref} + \mathbf{T}_{\mathbf{A},sun\_bak} + \mathbf{T}_{\mathbf{A},mon\_ref} \tag{10}$$

$$\mathbf{T}_{\mathbf{A},space} = \mathbf{T}_{\mathbf{A},gal\_dir} + \mathbf{T}_{\mathbf{A},sun\_dir} \tag{11}$$

where the term $\mathbf{T}_{\mathbf{A},earth\_dir}$ refers to radiation coming just from the earth (i.e., no space radiation reflections) and is the component containing the salinity signature. The inversion of Eqn. (4) (see Section 3.3) works best for a smoothly varying brightness temperature scene. Hence, it is better to separately compute the antenna temperatures of each of the space reflections using models for the sources and subtract them before trying before solving for $\mathbf{T}_{\mathbf{B},toa}$ in (4). For example, the galactic radiation field has sharp features that would present a problem in the application of the antenna pattern correction (Section 3.3). Therefore, it was decided to numerically compute the antenna temperatures for the various space reflections and store the results of the integrations as tables. The next subsections describe how the 6 space terms are computed.

2.2.1 Direct Galactic Radiation

The direct galactic radiation $\mathbf{T}_{\mathbf{A},gal\_dir}$ is computed by numerically evaluating the integral in (5),

$$\mathbf{T}_{\mathbf{A},gal\_dir} = \frac{1}{4\pi} \int_{Space} \mathbf{G}(\mathbf{b}) \mathbf{T}_{\mathbf{B},gal} d\Omega \tag{12}$$

$$\mathbf{T}_{\mathbf{B},gal} = \begin{bmatrix} 2T_{Bgal} \\ 0 \\ 0 \end{bmatrix} \tag{13}$$

where $T_{B gal}$ comes from a galactic map (Le Vine and Abraham, 2004) derived from radio astronomy measurements that has the cosmic background radiation of 2.73K added in. The pixel size in the Le Vine-Abraham map is 0.25^0 x 0.25^0, and the minimum pixel value is about 3K. We interpret the 3 K floor of the galactic map as the cosmic background radiation (2.73 K) plus radiation coming from distant galaxies.

The computation of $\mathbf{T_A}_{,gal\_dir}$ depends on the orbit position of the satellite and on the time of year because of the precession of the Aquarius orbit relative to the fixed galaxy every sidereal year (365.25636 days). A separate computation is done for each of the 3 radiometers because the antenna patterns are different. Tables of $\mathbf{T_A}_{,gal\_dir}$ are generated for 1441 positions within an orbit (every ¼°) and for 1441 periods during a sidereal year (about every 6 hours). These tables are specified by tagal_dir_tab(1441,1441,3,3), where the 4 dimensions correspond to time of sidereal year, orbit position, Stokes number, and radiometer number. Time is referenced to January 1, 2010, 00Z, and orbit position is referenced to the South Pole node. The South Pole node is the point in the orbit where the polar component of spacecraft velocity vector changes from pointing south to pointing north. The orbit position, which is also called *z*-angle, is the angle between a vector pointing from the Earth center to the South Pole node and a vector pointing from the Earth's center to the current position of the satellite. For example, 90° would correspond approximately to the satellite crossing the equator going south to north. The periodicity of the time variable is one sidereal year (365.25636 days). Even though it is assumed that the galactic T_B is unpolarized, antenna polarization mixing results in $\mathbf{T_A}_{,gal\_dir}$ having all four Stokes components. $\mathbf{T_A}_{,gal\_dir}$ is a small (0.3K), slowly varying term and the granularity size of the table is more than sufficient. During operational processing a bi-linear interpolation is used to look up tagal_dir_tab as a function of orbit position and time of year.

The calculation of $\mathbf{T_A}_{,gal\_dir}$ depends on the assumed ascending equator crossing time for Aquarius. A value of 5:59:59.16 pm was used to generate the pre-launch table tagal_dir_tab. The relative phase of the table can be adjusted via an input constant orbit_phase_dif that specifies the actual node time relative to 6:00:00 pm. The value of orbit_phase_dif has been set to 3.00 seconds based on post-launch analysis.

2.2.2 Reflected Galactic Radiation

The reflected galactic radiation $\mathbf{T_A}$,gal_ref can be large (5 K) and is the most difficult space term to deal with; and significant changes were made during the evolution of the retrieval algorithm (including the final version, V5.0) to deal with the effects of surface roughness. The structure described in this section assumes specular reflection and represents the pre-launch approach. A separate section (Section 6) has been devoted to the changes made to account for roughness.

To calculate $\mathbf{T_A}$,*gal_ref*, an integration over the Earth is done as follows

$$\mathbf{T}_{\mathbf{A},gal\_ref} = \frac{1}{4\pi} \int_{Earth} \mathbf{G}(\mathbf{b}) \boldsymbol{\Psi}(\phi) \mathbf{T}_{\mathbf{B},gal\_ref} \frac{\partial \Omega}{\partial A} dA \tag{14}$$

where $\mathbf{T_B}$,*gal_ref* is the brightness temperature of the reflected galactic radiation at the top of the atmosphere. For a specular surface, and since the incident galactic radiation is unpolarized, the reflected galactic radiation can be written as

$$\mathbf{T}_{\mathbf{B},gal\_ref} = \tau^2 \left(T_{Bgal} - T_{B\cos} \right) \mathbf{R} \tag{15}$$

$$\mathbf{R} = \begin{bmatrix} R_V + R_H \\ R_V - R_H \\ 0 \end{bmatrix} \tag{16}$$

where τ is the atmospheric transmittance and the vector **R** is the reflectivity for the 1st and 2nd Stokes in terms of the V-pol and H-pol reflectivity. As shown in Equation (15) the constant, T_{Bcos} = 3K, is subtracted from the galactic background before computing the reflected galactic radiation. Because T_{Bcos} is essentially constant in space it is convenient to include it in the Earth radiation calculation (see Section 2.3). Note that T_{Bcos} is actually the cosmic background (2.73 K) plus a constant (0.37 K) representing a mean "floor" of the celestial background radiation.

The approach outlined above in (16) only accounts for galactic reflections in the specular direction. In actuality, bistatic scattering from a rough ocean will scatter galactic radiation from many different directions into the mainlobe of the antenna. In effect, a rough ocean surface tends to add additional spatial smoothing to $\mathbf{T_A}$,*gal_ref*. The formulation for $\mathbf{T_B}$,*gal_ref* for a rough ocean surface is given in Section 6.

Tables of $\mathbf{T_A}_{,gal\_ref}$ are made. As was the case for the direct galactic radiation, $\mathbf{T_A}_{,gal\_ref}$ depends on the orbit position of the satellite and on the time of year. The tables have the same structure and format as the $\mathbf{T_A}_{,gal\_dir}$ except that one additional dimension is included for wind speed. The tables have the form tagal_ref_tab(1441,1441,3,3,5), where the first four dimensions are the same as described above for $\mathbf{T_A}_{,gal\_dir}$. The 5th dimension is wind speed going from 0 to 20 m/s in 5 m/s steps.

When computing tagal_ref_tab(1441,1441,3,3,5), the atmospheric transmittance τ is set to unity and the reflectivities R_V and R_H are set to ocean reflectivity values corresponding to a surface temperature and salinity of 20°C and 35 psu, respectively, and wind speeds equaling 0, 5, 10, 15, and 20 m/s. Also, the Faraday rotation angle is set to 0 when computing (14). During operational processing, adjustments are made to the values in the table to convert these nominal values to the actual values corresponding to a given observation. These adjustments are now discussed.

During operational processing, Aquarius scatterometer wind speeds (Section 5.2), as well as NCEP and other ancillary data (Section 4) are used to determine the actual values for τ and R_V and R_H. Also, the Faraday rotation angle ϕ_f is computed as discussed in Section 3.4. The values of $\mathbf{T_A}_{,gal\_ref}$ in the table are adjusted to correspond to the actual values of τ, R_V, R_H and ϕ_f as follows. First, the $\mathbf{T_A}_{,gal\_ref}$ table values are converted to brightness temperatures using the APC (equation (44) below). These classical Stokes T_B' s are converted to conventional V-pol and H-pol T_B. Then the following adjustment is made:

$$T'_{BP,gal\_ref} = \tau^2 \frac{R_P}{R_{0P}} T_{BP,gal\_ref} \tag{17}$$

where the prime sign denotes the adjusted value and subscript p denotes polarization (V or H). The value τ is the NCEP transmittance, R_{0P} is the reflectivity computed at the nominal of 20°C and 35 psu, and R_P is the reflectivity computed at the ancillary temperature and using an external 1st guess salinity obtained from the HYCOM ocean model (HYCOM 2012). T'_{BP,gal_ref} is then converted back to classical Stokes, Faraday rotation is applied, and the inverse APC equation (i.e. $\mathbf{A^{-1}}$) is applied to convert back to antenna temperature. Simulations showed that there was less error in doing the adjustment at the T_B level as compared to simply applying the adjustment to the T_A' s.

2.2.3 Direct Solar Radiation

The evaluation of (5) in the case of the direct solar radiation $\mathbf{T}_{\mathbf{A},sun\_dir}$ is relatively simple because the sun is a localized source, small compared to the scale of changes in the antenna pattern, and can be removed from the integral. Doing this, and assuming that the solar radiation is unpolarized, gives the following form for the Stokes parameters:

$$\mathbf{T}_{\mathbf{A},sun\_dir} = T_{B,sun}\,\frac{\Omega_{sun}}{4\pi}\mathbf{G}\left(\mathbf{b}_{sun\_direct}\right)\begin{bmatrix}2\\0\\0\\0\end{bmatrix} \tag{18}$$

where Ω_{sun} is the solid angle subtended by the sun and $\mathbf{b}_{sun\_direct}$ is the unit vector pointing from the spacecraft directly to the sun. The sun's brightness temperature is given by

$$T_{B,sun} = \frac{\lambda^2 F}{2k\Omega_{sun}} \tag{19}$$

where λ is the radiation wavelength, F is the solar flux, k is Boltzmann's constant, and Ω_{sun} is about $8.216\cdot10^{-5}$ steradians. This assumes an angular radius of 0.293^{o}, which is 10% greater than the optical angular radius (Wentz, 1978).

As with the direct galactic radiation, the computation of $\mathbf{T}_{\mathbf{A},sun\_dir}$ depends on the orbit position of the satellite and on the time of year. Tables of $\mathbf{T}_{\mathbf{A},sun\_dir}$ are generated in the same way as for $\mathbf{T}_{\mathbf{A},gal\_dir}$ and have the same structure and format, namely tasun_dir_tab(1441,1441,3,3). That is to say, tagal_dir_tab(1441,1441,3,3) and tasun_dir_tab(1441,1441,3,3) are completely analogous with one exception. For the sun table, a change in the ascending node time cannot be simply handled by an orbit phase change. Rather, it was necessary to regenerate this table after launch (a quick process that takes about an hour) when the true ascending node time was known.

In generating tasun_dir_tab(1441,1441,3,3), we set the flux value F to 1 solar flux. Then for operational processing, the table values are multiplied by the actual flux value obtained from radio astronomy measurements (Section 4.5) and the solar flux F is a standard component of Aquarius ancillary data. The mean noon-time solar flux is used in (19) and transient events associated with solar flares are identified with a flag.

An analysis of the effect of solar radiation on Aquarius is given in Wentz (2005, 2007), which provides maps showing how the solar contamination varies during the course of a year. Typical values for $\mathbf{T}_{\mathbf{A},sun\_dir}$ are 0.05 K or less.

2.2.4 Reflected Solar Radiation

The reflected solar radiation $\mathbf{T}_{\mathbf{A},sun\_ref}$ comes from the specular reflection of sunlight from a location on the Earth far away from the observation cell. The reflected sunlight enters into the far sidelobes of the antenna. Even though the gain of these far sidelobes is very small, the intensity of the sun at 1.4 GHz is large enough to make this a potential problem. The reflected solar component can be found following the logic above for the direct component. One obtains (also see Wentz (1978) and Le Vine et al., (2005), Dinnat and Le Vine (2008))

$$\mathbf{T}_{\mathbf{A},sun\_ref} = T_{B,sun}\frac{\Omega'_{sun}}{4\pi}\left\langle \tau^2 \mathbf{G}(\mathbf{b})\boldsymbol{\Psi}(\phi)\mathbf{R}\right\rangle_{ref} \tag{20}$$

where the prime sign on the sun solid angle Ω_{sun} indicates that the apparent solid angle of the sun reflecting off the spherical Earth is less than the solid angle when viewed directly. This effect is analogous to viewing an object through a convex mirror. The object will look smaller than it really is. This effect is discussed more in Section 2.2.6. The brackets in (20) denote an average over the neighborhood centered on the location of specular reflection, which is far removed from the observation footprint. The amount of averaging depends on surface roughness. For a specular (i.e., perfectly flat) surface, no averaging is required, and (20) can be evaluated for **b** pointing in the direction of the specular reflection. For high winds when the surface becomes rough, the antenna gain needs to be averaged over 5° to 10°. $\boldsymbol{\Psi}(\phi)$, R and τ are defined as in (14) - (16). In the sidelobe region, the terms τ^2, $\boldsymbol{\Psi}(\phi)$, and **R** vary more slowly than **G**(**b**), and (20) can be approximated by

$$\mathbf{T}_{\mathbf{A},sun\_ref} = T_{B,sun}\frac{\Omega'_{sun}}{4\pi}\tau^2_{ref}\overline{\mathbf{G}}(\mathbf{b})\boldsymbol{\Psi}\left(\phi_{ref}\right)\mathbf{R}_{ref} \tag{21}$$

where the subscript *ref* denotes the quantity is calculated assuming a perfectly specular reflection and the overbar on the antenna gain function denotes that the antenna gain has been smoothed over an angular range to account for surface roughness.

The calculation of $R_{V,ref}$, $R_{H,ref}$, and τ_{ref} at the remote sun reflection point adds additional complexity to the modeling and algorithm. All of the ancillary data are keyed to the observation footprint which can be thousands of kilometers away from the sun reflection point. Furthermore, simulations (Wentz, 2005; 2007) indicate $\mathbf{T_A}_{,sun\_ref}$ is very small, 0.01 K or less, and can probably be neglected. We have assumed that the reflectivity is that for a specular ocean surface at a temperature of 20°C and a salinity of 35 psu and the transmittance is set to unity.

Tables of $\mathbf{T_A}_{,sun\_ref}$ are generated in the same way as for $\mathbf{T_A}_{,sun\_dir}$ and have the same structure and format, namely tasun_ref_tab(1441,1441,3,3).

2.2.5 Backscattered Solar Radiation

Most of the time, the Aquarius main beam footprints will be entirely in the dark. However, at the higher latitudes in the summer, the sun will be visible near the horizon, and solar radiation will impinge onto the Aquarius footprint at a grazing incidence angle. In this case, a small portion of this sunlight can be backscattered into the mainlobe of the antenna. We denote this backscatter component as $\mathbf{T_A}_{,sun\_bak}$, and it has a magnitude on the order of 0.1 to 0.2 K when it does occur.

We use a model developed by Dinnat and Le Vine (2008) to specify $\mathbf{T_A}_{,sun\_bak}$. This model parameterizes $\mathbf{T_A}_{,sun\_bak}$ in terms of the sun's zenith angle and wind speed. $\mathbf{T_A}_{,sun\_bak}$ is tabularized as tasun_bak_tab(161,26,3,3), where the 4 dimensions corresponds to sun zenith angle, wind speed, Stokes number, and radiometer number. The zenith angle goes from 58° to 90° in steps of 0.2°, and the wind speed goes from 0 to 25 m/s in steps of 1 m/s. This table was generated assuming a solar flux, F = 264 solar flux units. For operational processing, the values from tasun_bak_tab(161,26,3,3) are multiplied by F/264, where F is the actual flux value obtained from radio astronomy measurements (RSTN noon time flux, Section 4.5).

The $\mathbf{T_A}_{,sun\_bak}$ tables are computed assuming a nominal surface temperature and salinity of 20°C and 35 psu, an atmospheric transmittance of unity, and no Faraday rotation, i.e., the same nominal conditions used for the $\mathbf{T_A}_{,gal\_ref}$ tables. During operational processing, an adjustment to the table values is made to convert these nominal values to the actual values corresponding to a given observation. This adjustment is described in (17) and is exactly the same as described above for the reflected galactic radiation. It should be pointed out that since $\mathbf{T_A}_{,sun\_bak}$ is a very small term (0.1 to

0.2 K), the adjustment done by (17) has negligible effect over the ocean. The only appreciable effect of the adjustment is that over land the ratio R_P/R_{0P} becomes very small because land has a much smaller reflectivity than ocean, thereby reducing the value of $\mathbf{T}_{\mathbf{A},sun\_bak}$ significantly.

2.2.6 Reflected Lunar Radiation

At certain times each month, moonlight reflected off the ocean surface enters the mainlobe of the antenna. This phenomenon is discussed by Dinnat et al. (2009) and is modeled here by using a simplified antenna gain function. A simplified approach can be used because the effect occurs rarely, only is significant near the mainbeam, and is small in magnitude (1 K or less). In particular, assuming the radiation is unpolarized, the following simplified gain pattern is adopted for the 1st and 2nd Stokes:

$$\tilde{\mathbf{G}} = \begin{pmatrix} G_{11} & G_{12} \\ G_{21} & G_{22} \end{pmatrix} 10^{-0.3\left(\frac{\xi}{\xi_0}\right)^2} \tag{22}$$

where ξ is the angle between the antenna boresight vector and the vector from spacecraft to moon specular reflection point. The angle ξ_0 is the half-power angle of the antenna pattern. Its values for the inner, middle, and outer horns are 3.04°, 3.17°, and 3.24°. The values for the boresight gains G_{ij} are given in Table 1. Equation (22) is a commonly used approximation for the gain over the mainlobe of the antenna.

The reflected lunar radiation is then given by

$$\mathbf{T}_{\mathbf{A},mon\_ref} = T_{B,moon} \frac{\Omega'_{moon}}{4\pi} \tau^2 \tilde{\mathbf{G}} \mathbf{R} \tag{23}$$

where the reflection vector **R** is given by (16) but in this case the last component, which is zero, is discarded and **R** is 2x2 to match the order of $\tilde{\mathbf{G}}$. No adjustment is made for Faraday rotation, because the effect of lunar radiation is already small. The terms **R** and τ are computed from the ancillary data for the observation. $T_{B,moon}$ is assumed to be 275K (Dinnat et al. 2009) and Ω'_{moon} is the apparent solid angle of the moon's reflection off the spherical earth. The relationship between the true solid angle Ω when viewed directly and the apparent solid angle Ω' when viewed as a reflection is modified by the curvature of the surface. At nadir one obtains:

$$\Omega' = \frac{\Omega}{\left(1+\frac{2s}{R_E}\right)^2} \tag{24}$$

where s is the slant path from the satellite to the point of reflection, and R_E is the Earth's radius. The expression changes slowly as a function of incidence and for the Aquarius inner, middle, and outer horns Ω' is 3.93e-05, 3.79e-05, 3.63e-05 steradians, respectively.

Table 1: This table gives the boresight gains used to compute reflected lunar radiation as specified by equation (22).

Horn	G_{11}	G_{12}	G_{21}	G_{22}
Inner	74.41968	-0.47552	-0.42802	74.36780
Middle	70.84354	0.13980	0.12591	70.82498
Outer	65.86123	-0.58609	-0.52414	65.78670

2.3 Earth-Only T_B Equation

The one remaining term to be specified in the forward model is $\mathbf{T}_{\mathbf{A},earth\_dir}$, which is the radiation coming just from the earth (i.e., no space radiation either direct or reflected). The one exception, the uniform cosmic background radiation that reflects off the Earth, is included in $\mathbf{T}_{\mathbf{A},earth\_dir}$. The radiation from the Earth can be written in the form:

$$\mathbf{T}_{\mathbf{A},earth\_dir} = \frac{1}{4\pi}\int_{Earth} \mathbf{G}(\mathbf{b})\boldsymbol{\Psi}(\phi)\mathbf{T}_{\mathbf{BE}}\frac{\partial\Omega}{\partial A}dA \tag{25}$$

where it is understood that $\mathbf{T}_{\mathbf{BE}}$ refers to the TOA brightness temperature for radiation coming just from the earth. When doing forward modeling (i.e. simulations), the integral in (25) is found by doing a precise integration over the Earth's surface at a spatial resolution of about 1 km over the mainlobe of the antenna (a coarser resolution is used outside the mainlobe). This section discusses the Earth-only brightness temperature, $\mathbf{T}_{\mathbf{BE}}$, that appears in the kernel of the integral.

2.3.1 Theoretical Formulation

The AMSR-E ATBD (Wentz and Meissner, 2000) gives a detailed description of the radiative transfer equation for $\mathbf{T}_{\mathbf{BE}}$. This formulation is also applicable to Aquarius (Le Vine et al., 2011). In this section, it is more convenient to work in terms of the modified Stokes parameters (i.e., V-pol and

H-pol) rather than the classical Stokes parameters. We are assuming that at 1.4 GHz, the 3rd and 4th Stokes parameters, which are the third and fourth elements of $\mathbf{T_{BE}}$, are zero. The V-pol and H-pol components of $\mathbf{T_{BE}}$ are given by

$$T_{BE,P} = T_{BU} + \tau\left[E_P T_S + T_{BP\Omega}\right] \tag{26}$$

where subscript P denotes polarization, either V or H. T_{BU} is the brightness temperature of the upwelling atmospheric radiation, τ is the atmospheric transmittance, E_P is the Earth surface emissivity, T_S is the Earth surface temperature (K), and T_{BPW} is the downwelling sky radiation that is scattered off the Earth surface in the direction of the observation.

The attenuation due to the atmospheric can be expressed in terms of the transmittance function $\tau(s_1,s_2)$

$$\tau\left(s_1, s_2\right) = \exp\left(-\int_{s_1}^{s_2} ds\ \alpha(s)\right) \tag{27}$$

which is the attenuation between points s_1 and s_2 along the propagation path s. The term $\alpha(s)$ is the atmosphere absorption due to oxygen, water vapor, and liquid water (Wentz and Meissner, 2000). The total transmittance τ in (26) is given by

$$\tau = \tau\left(0, S\right) \tag{28}$$

where S is the slant range from the surface to the top of the atmosphere. The upwelling and downwelling atmosphere emissions are given by

$$T_{BU} = \int_0^S ds\ \alpha(s)\ T(s)\ \tau(s,S) \tag{29}$$

$$T_{BD} = \int_0^S ds\ \alpha(s)\ T(s)\ \tau(0,s) \tag{30}$$

where $T(s)$ is the air temperature profile. In the case of a rough surface, the downwelling radiation T_{BU} reflected from the surface back toward the spacecraft is given by the scattering integral:

$$T_{BP\Omega} = \frac{\sec\theta_i}{4\pi}\int_0^{\pi/2}\sin\theta_s d\theta_s \int_0^{2\pi} d\varphi_s (T_{BD} + \tau T_{B\cos})\left[\sigma_{o,c}\left(\mathbf{k_s},\mathbf{k_i}\right) + \sigma_{o,\times}\left(\mathbf{k_s},\mathbf{k_i}\right)\right] \quad (31)$$

where θ_s is the zenith angle for the downwelling radiation impinging on the surface, and θ_i is the incidence angle for the upwelling radiation leaving the surface in the direction of the observation. The integral is over the 2π steradians of the upper hemisphere. The term $\sigma_{o,c}$ and $\sigma_{o,x}$ are the co-pol (i.e. polarization equal to *P*) and cross-pol (i.e. polarization orthogonal to *P*) bistatic normalized cross sections, which are functions of unit propagation vectors $\mathbf{k_i}$ and $\mathbf{k_s}$ that denote the direction of the upwelling and downwelling radiation, respectively. The angle j_s is the azimuth of $\mathbf{k_s}$ relative to $\mathbf{k_i}$. These cross sections specify what fraction of power coming from $\mathbf{k_s}$ is scattered into $\mathbf{k_i}$. T_{BD} is the brightness temperature of the downwelling atmospheric radiation, and T_{Bcos} is the cosmic background plus distant galaxies radiation and equals 3 K (see Section 2.2.2).

Assuming a uniform incident wave, one can define the reflectivity of a rough surface with an equation similar to (31):

$$R_P = \frac{\sec\theta_i}{4\pi}\int_0^{\pi/2}\sin\theta_s d\theta_s \int_0^{2\pi} d\varphi_s \left[\sigma_{o,c}\left(\mathbf{k_s},\mathbf{k_i}\right) + \sigma_{o,\times}\left(\mathbf{k_s},\mathbf{k_i}\right)\right] \quad (32)$$

Assuming equilibrium, the surface emissivity E_P is given by (Peake, 1959) Kirchhoff's law to be

$$E_P = 1 - R_P \quad (33)$$

To numerically compute $\mathbf{T_{BE}}$ from the above theoretical equations, a number of empirical models and approximations are used as described in the next sections.

2.3.2 Empirical Approach to Specifying Atmospheric Terms

The atmospheric upwelling and downwelling brightness temperatures T_{BU} and T_{BD}, and the atmospheric transmittance τ, are computed by numerically integrating equations (27) through (30). For operational processing, we use NCEP profiles of pressure, temperature, humidity, and liquid water to find profiles of $\alpha(s)$. The NCEP profiles are interpolated to the exact time and location of the Aquarius observations. For the oxygen absorption component of $\alpha(s)$ we use the model by Liebe et al. (1992). For the water vapor absorption component of $\alpha(s)$ we use the expressions given by Rosenkranz (1998) with the small modifications by Wentz and Meissner (2016). This

small modification was based on an analysis of WindSat and AMSR-E 7 GHz brightness temperatures. The cloud water absorption is calculated using the Rayleigh absorption formula and the dielectric constant model of Meissner and Wentz (2004) for pure water. For details see the AMSR ATBD (Wentz and Meissner 2000).

2.3.3 Empirical Approach to Specifying Emissivity

The theoretical modeling of the bistatic normalized cross sections is not sufficiently advanced to provide estimates of R_P and E_P (P=V, H) with the accuracy needed to retrieve sea surface salinity. Instead, we express the emissivity E_P in terms of a specular component E_{0P} (i.e. flat surface) and a wind-induced (rough) component $\Delta E_{rough,P}$:

$$E_P = E_{0,P} + \Delta E_{rough,P} \tag{34}$$

The specular component $E_{0,P} = 1 - R_{0,P}$ is computed using the Fresnel equations to obtain the reflectivity

$$R_V = \left| \frac{\varepsilon \cos\left(\bar{\theta}\right) - \sqrt{\varepsilon - \sin^2\left(\bar{\theta}\right)}}{\varepsilon \cos\left(\bar{\theta}\right) + \sqrt{\varepsilon - \sin^2\left(\bar{\theta}\right)}} \right|^2 \qquad R_H = \left| \frac{\cos\left(\bar{\theta}\right) - \sqrt{\varepsilon - \sin^2\left(\bar{\theta}\right)}}{\cos\left(\bar{\theta}\right) + \sqrt{\varepsilon - \sin^2\left(\bar{\theta}\right)}} \right|^2 \tag{35}$$

In (35), $\bar{\theta}$ is the gain weighted average Earth incidence angle defined in Section 3.2 Equation (42). ε is the dielectric constant of sea-water and it is computed from the model of Meissner and Wentz (2004, including the update 2012).

The computation of the wind-induced component $\Delta E_{rough,P}$ in the Aquarius V5.0 release is based on Meissner et al. (2014). It has been derived empirically from match-up sets between measured Aquarius T_B and wind speed measurements from WindSat (Wentz et al. 2013) and F17 SSMIS (Wentz et al. 2012). Some small changes have been made in the Aquarius V5.0 algorithm since the publication (Meissner et al. 2014). This is explained in detail in Section 5.

2.3.4 Empirical Approach to Specifying Reflected and Scattered Radiation

The remaining term that needs to be specified is the scattering integral for the downwelling radiation: $T_{BP\Omega}$. A primary reason for computing the space radiation terms separately, as described in

Section 2.2, is to facilitate the computation of $T_{BP\Omega}$. In the absence of sharply varying space terms, the integral (Eqn. (31)) now just contains $T_{BD} + \tau \cdot T_{Bcos}$, a small term that varies very slowly over angle. The bistatic cross section has a sharp peak in the specular direction (i.e. $\theta_i = \theta_s$ and $j_s = 180°$), and over this sharp peak $T_{BD} + \tau \cdot T_{Bcos}$ varies little and can be removed from the integral. The remaining integral is the surface reflectivity. Hence to a first approximation, one has

$$T_{BP\Omega} = (T_{BD} + \tau \cdot T_{B\cos}) \cdot R_P \tag{36}$$

and T_{BD} and τ conveniently have the same slant path angle relative to the surface as T_{BU}.

2.3.5 Empirical Approach to Handling Land and Sea-Ice Observations

Although our primary focus is observations over the ocean, the formulation we have presented applies equally well to land and sea-ice observations. The only exception is that the sea-surface emissivity E_P given by (34) needs to be replaced by a land or sea-ice emissivity as defined in (34) with reflectivity, R_P, appropriate for the surface. For observation of mixed surfaces, the following expressions are used

$$R_P = \lambda_{water} \cdot R_{P,water} + \lambda_{land} \cdot R_{P,land} + \lambda_{ice} \cdot R_{P,ice} \tag{37}$$

$$E_P \cdot T_s = \left(1 - R_{P,water}\right) \cdot \lambda_{water} \cdot T_{water} + \left(1 - R_{P,land}\right) \cdot \lambda_{land} \cdot T_{land} + \left(1 - R_{P,ice}\right) \cdot \lambda_{ice} \cdot T_{ice} \tag{38}$$

where λ denotes fractional area and T denotes surface temperature. The reflectivities for land and sea ice are discussed in Appendix B. Equation (38) is then substituted into (26). The fractional land λ_{land} is computed from a static 1-km land mask (Section 4.6). The fractional sea-ice λ_{ice} comes from the AMSR2 and SSMIS sea ice concentration maps (Section 4.7). The fractional water is then $\lambda_{water} = 1 - \lambda_{land} - \lambda_{ice}$. In Version 5.0 the gain weighted fractions g_{land} and g_{ice} are used for scenes over land, sea-ice or in waters near the coast or sea-ice edge. In the open ocean, far away from geographic interfaces like the coast or sea-ice edge, the unweighted fractions f_{land} and f_{ice} are used. To be specific:

$$\begin{aligned} &\lambda_{land} = g_{land} \text{ and } \lambda_{ice} = g_{ice} \quad \text{if} \quad g_{land} + g_{ice} \geq 0.002 \\ &\lambda_{land} = f_{land} \text{ and } \lambda_{ice} = f_{ice} \quad \text{if} \quad g_{land} + g_{ice} < 0.002 \end{aligned} \tag{39}$$

In the 2nd case, far away from land or sea-ice, the unweighted fractions f are very close to zero or exactly zero. The reason for using the 2nd case in (39) is to avoid errors in the calculation for scenes that are far away from land or sea-ice. There are many uncertainties in the model computation of land or sea-ice scenes. It should be noted that the forward model has only been validated over open ocean scenes.

3. Salinity Retrieval Algorithm

The salinity retrieval algorithm consists of a number of steps that are intended to remove the unwanted sources of radiation (galaxy, sun, moon, and Earth's atmosphere) in order to obtain just the Earth's surface emission term. A maximum likelihood estimator (MLE) is then used to estimate salinity from the surface emission. These steps include:

1. The radiation received from the galaxy, sun, and moon is subtracted from the T_A measurements.
    - Direct radiation from the galaxy (Section 2.2.1) and Sun (Section 2.2.3) is removed. Direct radiation from the Moon is small enough to be ignored.
    - Reflected radiation from the galaxy (Section 2.2.2), Sun (Section and 2.2.4 and 2.2.5) and Moon (Section 2.2.6) is removed. Faraday rotation is ignored.
    - The APC is applied and (46) is used to compute a first estimate of Faraday rotation.
    - This Faraday rotation is applied to reflected galactic and Sun glint signals which are given in tables at TOA.
    - An inverse APC is applied, and the two signals are subtracted from T_A TOI.
2. The antenna pattern correction (APC) is applied to the residual of step 1. It removes cross-polarization contamination and corrects for radiation from the sidelobes and backlobes. The APC converts the top-of-the-ionosphere (TOI) antenna temperature to a brightness temperature.
3. Faraday rotation is removed using the 2nd and 3rd Stokes parameters as described in Section 3.4. This provides the top-of-the-atmosphere (TOA) brightness temperature.
4. The atmospheric contributions to the TOA T_B are computed using NCEP operational fields and are removed from the TOA T_B (Section 3.5). The result is the surface emission $T_{BE,SUR}$ by itself.
5. The surface roughness correction (Section 5.3) is applied which removes the effect of wind roughening of the ocean surface. The result is the emission of a specular (flat) surface $T_{BE,SUR,0}$.
6. The salinity value is retrieved from the flat surface emission using a MLE.

Figure 2 shows a flow diagram of the major steps in the V5.0 Aquarius salinity retrieval algorithm.

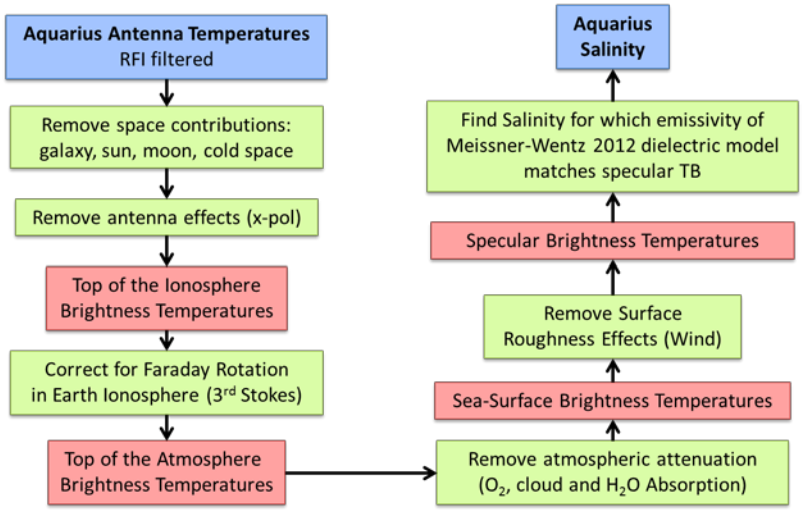

Figure 2: Flow diagram of the V5.0 Aquarius salinity retrieval algorithm.

Each of these steps is now described.

3.1 Removal of the Radiation Coming from Space

The first step in the salinity retrieval is to remove the contribution of radiation that originates from celestial sources (galaxy, sun, moon) from the calibrated radiometer output, $\mathbf{T}_{\mathbf{A},mea}$. Section 2.2 lists the 6 components of space radiation and describes how they are computed during operational processing. This subtraction is represented by

$$\mathbf{T}_{\mathbf{A},earth\_dir} = \mathbf{T}_{\mathbf{A},mea} - \mathbf{T}_{\mathbf{A},gal\_dir} - \mathbf{T}_{\mathbf{A},gal\_ref} - \mathbf{T}_{\mathbf{A},sun\_dir} - \mathbf{T}_{\mathbf{A},sun\_ref} - \mathbf{T}_{\mathbf{A},sun\_bak} - \mathbf{T}_{\mathbf{A},mon\_ref} \qquad (40)$$

After subtraction, we are left with the radiation coming from the Earth, $\mathbf{T}_{\mathbf{A},earth\_dir}$. Strictly speaking, it still contains the direct and reflected radiation from the cosmic microwave background (CMB) $T_{B\cos} = 3K$. The direct CMP radiation is constant (i.e. independent on location) and enters the antenna backlobes. It will be effectively removed in the antenna pattern correction (Section 3.3). The CMB radiation that is reflected from the surface has been lumped together with the downwelling atmospheric radiation (see (31) and (36)). The reflected cosmic microwave background CMB will be effectively removed with the removal of atmospheric effects (Section 3.5).

Subtracting the reflected celestial components presents a problem because after reflection they are polarized and therefore impacted by Faraday rotation which is not yet known at this step in the algorithm. As a compromise, T_{A,mon_ref} is subtracted ignoring Faraday rotation. The $T_{A,\ sun\_ref}$ and reflected galactic radiation are subtracted after making a first estimate of the Faraday rotation as described in steps 3 – 6 in the list above.

3.2 Definition of Reference Brightness Temperatures

At this point in the retrieval algorithm, it is necessary to define the brightness temperature that we seek to retrieve from $\mathbf{T_A}_{,earth\_dir}$. One possible choice is the T_B at boresight. However, it was decided to define the reference brightness temperature as an average over the 3-dB Aquarius footprint since this is closer to the actual output of the antenna. To be precise, the reference TOA T_B is defined as

$$\overline{\mathbf{T}}_{\mathbf{BE},toa} = \frac{\int\limits_{3dB\ footprt} \mathbf{T}_{\mathbf{BE},toa}(\theta_i)\, dA}{\int\limits_{3dB\ footprt} dA} \tag{41}$$

where the integral is over the 3-dB footprint. The 3-db footprint is defined as that part of the Earth integral for which the angle between the boresight vector $\mathbf{b_0}$ and the look vector $\mathbf{b}$ is less than 3.07°, 3.17°, and 3.24° for the inner, middle, and outer horns, respectively. We can define an effective incidence angle $\overline{\theta}_i$ so that when doing the footprint averaging (i.e. in Eqn. (41)), the incidence angle is held to a constant value $\overline{\theta}_i$, which is the gain-weighted average (over the 3 dB footprint) of the incidence angle and given by

$$\overline{\theta}_i = \chi\theta_{i,boresight} \tag{42}$$

where $\theta_{i,boresight}$ are the boresight incidence angles 29.36°, 38.44°, 46.29°, and c is 1.00177, 1.00186, 1.00148 for the inner, middle, and outer horns, respectively. This adjustment is so small that it is probably not needed, and one could simply use the boresight incidence angle for $\overline{\theta}_i$. By definition $\overline{\mathbf{T}}_{\mathbf{BE},toa}$ is a characteristic of the Earth scene being viewed (an average value) and is inde-

pendent of the radiometer antenna except that the regime of averaging is the 3db antenna footprint. This is the parameter that the algorithm is designed to retrieve.

Because Faraday rotation is important at L-band, there are two brightness temperatures that also must be defined: Brightness temperature at the top of the ionosphere (at the spacecraft) and at the top of the atmosphere. The top-of-the-ionosphere (TOI) reference brightness temperature is denoted by $\overline{\mathbf{T}}_{\mathbf{BE},toi}$ and is related to the brightness temperature at the top of the atmosphere, T_{BE_toa} by the Faraday rotation:

$$\overline{\mathbf{T}}_{\mathbf{BE},toi} = \mathbf{\Psi}\left(\phi_f\right)\overline{\mathbf{T}}_{\mathbf{BE},toa} \tag{43}$$

3.3 Estimation of Top-of-the-Ionosphere Brightness Temperature

Now that we have defined our reference T_B, we must estimate its value given the antenna temperature $\mathbf{T}_{\mathbf{A},earth\_dir}$. In principle we are seeking the solution of the integral in (25) for $\overline{\mathbf{T}}_{\mathbf{BE},toi}$ as defined in (43) given the measurement, $\mathbf{T}_{\mathbf{A},earth\_dir}$. Since it is not possible to directly invert the integral, other means are required. We use the following linear regression method:

$$\hat{\mathbf{T}}_{\mathbf{BE},toi} = \mathbf{A}\cdot\mathbf{T}_{\mathbf{A},earth\_dir} \tag{44}$$

where **A** is a 3 by 3 matrix called the antenna pattern correction (APC) matrix, and the 'hat' on $\mathbf{T}_{\mathbf{BE},toi}$ denotes that this is an estimated quantity as compared to the true value. It should be noted that (44) also effectively removes the antenna spillover. This is the direct radiation from the cosmic microwave background $T_{B\cos} = 3K$, which is constant in space and which enters the antenna backlobes.

As a first step the values of the matrix of **A** were determined from simulations using the forward algorithm and the Aquarius antenna patterns from the GRASP 2012 software (see Section 7.2). Simulations are performed to produce a year of simulated $\mathbf{T}_{\mathbf{A},earth\_dir}$. This represents about 25 million observations for each horn at intervals of 1.44 seconds. In addition to providing $\mathbf{T}_{\mathbf{A},earth\_dir}$, the simulation also provides the true value of $\overline{\mathbf{T}}_{\mathbf{BE},toi}$. The standard least-squares method (linear

regression) is used to find the APC matrix **A** that minimizes the mean square difference of $\hat{\mathbf{T}}_{\mathbf{BE},toi}$ - $\overline{\mathbf{T}}_{\mathbf{BE},toi}$.

When deriving the APC matrix, **A**, simulated observations that contain sea ice or that are a mixture of land and water are excluded. That is to say, regression (44) is only done for observations that are totally land or totally water. It was decided not to train the regression with mixed scenes, which pose many difficulties when trying to relate antenna temperatures to brightness temperatures.

Considering all complexities of the integral in Equation (25), it is not obvious if a simple regression like (44) will perform adequately. To evaluate its performance, we compute the RMS value of $\hat{\mathbf{T}}_{\mathbf{BE},toi}$ - $\overline{\mathbf{T}}_{\mathbf{BE},toi}$ using all the simulated observations. The comparison was done separately for all-ocean and all-land observations, but the same APC matrix was used for both. Over the ocean, the RMS for V-pol and H-pol ranged from 0.05 to 0.08 K. Over land, the RMS values were considerably higher, ranging from 1 to 2 K. The higher land values are due to the land T_B having more variability. A small number of land observations having very large variability show errors of 10-20 K, which have a great influence on the RMS statistics. These results show that the APC regression (44) works well for uniform scenes, like the ocean. Non-uniform scenes present a problem for the APC, which is probably unavoidable.

Experiments were made deriving the APC just with ocean observations since this is the primary focus. There was a slight improvement when the ocean-only APC was applied to the ocean observations, but the improvement was very small compared to the overall performance of 0.05 to 0.08 K, and a decision was made to stay with the ocean + land APC, which is trained over the full range of T_A.

The largest error in the APC is with respect to the 3rd Stokes parameter for the outer horn, for which the ocean-only observations exhibit an RMS of 0.2K. However, the 3rd Stokes parameter is just used for Faraday rotation correction, and the mapping of this error into the estimate of the top-of-the-atmosphere (TOA) T_B is very small.

The 0.05 to 0.08 K performance of the APC is of some concern, given the demanding requirements for Aquarius brightness temperature accuracy. Some experiments were made in an attempt to improve its performance, such as using an ocean-only APC, using separate APC for ascending and descending orbit segments, and adding higher order terms to (44). These attempts helped slightly, but not enough to warrant their implementation.

The post-launch adjustment of the APC matrix **A** is discussed in detail in Section 7.2. The computation of the APC used in Version 5.0 is based on the GRASP 2012 antenna patterns, but with several adjustments. An analysis (Meissner 2014a) showed that the Aquarius GRASP 2012 antenna patterns used to determine the APC overestimated the gain in the antenna backlobes. This resulted in unrealistic values for the T_B over land. The analysis (Meissner 2014a) also showed that some of the non-diagonal (cross-pol) matrix elements in **A** need to be adjusted. The final APC is given in Section 7.2.1 and the adjustments are described in Section 7.2.2.

3.4 Correction for Faraday Rotation

The next step in the retrieval is a correction for Faraday rotation. Faraday rotation is removed by applying the following expression:

$$\hat{\mathbf{T}}_{\mathbf{BE},toa} = \boldsymbol{\Psi}\left(-\phi_f\right)\hat{\mathbf{T}}_{\mathbf{BE},toi} \tag{45}$$

If one assumes that the 3rd and 4th Stokes parameters due to radiation from the Earth surface are negligibly small, one may set the 3rd Stokes parameter in $\overline{\mathbf{T}}_{\mathbf{BE},toa}$ to zero and obtain the Faraday rotation angle (Yueh, 2000) from

:

$$\phi_f = \frac{1}{2}\arctan\left(\frac{\hat{T}_{BE,toi,3}}{\hat{T}_{BE,toi,2}}\right) \tag{46}$$

where the last subscript denotes Stokes number. Using (46) and (6) one obtains the TOA T_B

$$\begin{aligned}\hat{T}_{BE,toa,1} &= \hat{T}_{BE,toi,1}\\ \hat{T}_{BE,toa,2} &= \sqrt{\left[\hat{T}_{BE,toi,2}\right]^2 + \left[\hat{T}_{BE,toi,3}\right]^2}\end{aligned} \tag{47}$$

3.5 Removal of Atmospheric Effects

In this subsection we switch over to using the modified Stokes parameters (V-pol and H-pol) rather than the classical Stokes parameters for $\hat{\mathbf{T}}_{\mathbf{BE},toa}$, and these two components are denoted simply as $T_{BE,P}$, where subscript P denotes polarization (either V or H). This step in the retrieval algorithm is intended to remove the effect of the atmosphere. This is done by inverting (26) to yield the surface emission $T_{BE,sur}$.

$$T_{BE,P,sur} \equiv E_P T_S = \frac{T_{BE,P} - T_{BU}}{\tau} - T_{BP\Omega} \tag{48}$$

Substituting (36) in (48) gives

$$T_{BE,P,sur} \equiv E_P T_S = \frac{T_{BE,P} - T_{BU}}{\tau} - (T_{BD} + \tau T_{B\cos}) R_P \tag{49}$$

Noting that $R_P = 1 - E_P$, (49) can be rewritten as:

$$T_{BE,P,sur} = \left[\frac{\frac{T_{BE,P} - T_{BU}}{\tau} - (T_{BD} + \tau T_{B\cos})}{T_S - (T_{BD} + \tau T_{B\cos})} \right] T_S \tag{50}$$

where the bracketed term is the surface emissivity.

The atmospheric terms for the upwelling and downwelling brightness temperature T_{BU} and T_{BD}, and the atmospheric transmittance τ are computed by numerically integrating equations (27) through (30) along the boresight ray. For operational processing, we use NCEP profiles of pressure, temperature, humidity, and liquid water to find profiles of $\alpha(s)$. The NCEP profiles are interpolated to the exact time and location of the Aquarius observations. See Sections 2.3.2 and 4.2 for details. The auxiliary SST field used is the CMC product (Section 4.1). The land surface temperature T_S comes from the NCEP daily, 0.25° product. T_{Bcos} is a constant 3 K (cosmic background plus a constant contribution from celestial sources). Given these ancillary data, (50) can be calculated to yield the surface emission brightness temperature. Note that this calculation of $T_{BE.P,sur}$ is done for all surface types (ocean, land, sea-ice, and mixed) as described in Section 2.3.5.

3.6 Removal of Surface Roughness Effects

The calculation and removal of surface roughness effect is described in detail in Section 5.3. It results in a brightness temperature $T_{BE.P,sur,0}$ of a specular (flat) ocean surface.

3.7 Estimation of Salinity Given Specular Surface Emission Brightness Temperature

The Aquarius sea surface salinity S is estimated from the values of $T_{BE.P,sur,0}$ of V-pol and H-pol. The basic idea is to obtain a best match between the observed values of $T_{BE.P,sur,0}$ with the calculation from the forward model. This is done by performing a maximum likelihood estimator (MLE), which minimizes the sum of squares:

$$\chi^2 = \frac{\left[T^{obs}_{BE,SUR,0,V} - T^{model}_{BE,SUR,0,V}\left(T_S, S\right)\right]^2}{\mathrm{var}\left(T_{BE,SUR,0,V}\right)} + \frac{\left[T^{obs}_{BE,SUR,0,H} - T^{model}_{BE,SUR,0,H}\left(T_S, S\right)\right]^2}{\mathrm{var}\left(T_{BE,SUR,0,H}\right)} \tag{51}$$

Equation (51) assumes that V-pol and H-pol channels are independent. The observed values of $T_{BE.P,sur,0}$ are obtained from the Aquarius T_A measurements after performing all the corrections explained in Sections 3.1 - 3.6. The forward model computation of $T_{BE.P,sur,0}$ uses the Fresnel equations for the reflection from a flat ocean surface, the Meissner Wentz (2004, with the 2012 update) dielectric constant of sea water and the ancillary SST field from CMC (Section 4.1). The 2 terms in (51) are weighted by the inverse expected variances of the V-pol and H-pol channels. These variances can be estimated from computing $T_{BE,sur,0}$ for typical ocean scenes with and without added typical errors that arise in the observation. The most important ones to consider are radiometer noise (NEDT), errors in the surface wind speed that is used in the roughness correction, errors in the ancillary SST and errors in the reflected galaxy. In the V5.0 retrievals we have decided to weigh V-pol and H-pol equally, i.e. $\mathrm{var}\left(T_{BE,SUR,0,V}\right) = \mathrm{var}\left(T_{BE,SUR,0,H}\right)$ in (51). This means effectively that in the MLE both denominators can be set to 1.

The goodness of fit in the MLE can be characterized by the root sum of squares of measured minus calculated TB, where in the model calculation the actual retrieved Aquarius salinity S_{ret} is used. We call this parameter $T_{B,consistency}$:

$$T_{B,consistency} = \sqrt{\left[T^{obs}_{BE,SUR,0,V} - T^{model}_{BE,SUR,0,V}\left(T_S, S_{ret}\right)\right]^2 + \left[T^{obs}_{BE,SUR,0,H} - T^{model}_{BE,SUR,0,H}\left(T_S, S_{ret}\right)\right]^2} \quad (52)$$

Large values for $T_{B,consistency}$ indicate a poor fit between observation. This can be caused for example by undetected RFI, contamination from land, inadequate roughness correction, and sea ice or celestial radiation that has not been properly removed. We use the value of $T_{B,consistency}$ as a quality control (Q/C) indicator for the salinity retrievals (Meissner, 2014b; Le Vine and Meissner 2014). Salinity retrievals are flagged if $T_{B,consistency}$ exceeds 0.4 K.

3.8 Reference Salinity and Calculation of Expected Antenna Temperature

Section 2.3 gives the formulation necessary to compute the 'earth-only' TOA T_B. The inputs to the formulation (SST, wind, atmospheric terms, etc.) are all described above with the exception of salinity, which in the above treatment was the retrieved variable (i.e. unknown). In order to compute an expected TOA T_B, we need to have some reasonable value for salinity. For V5.0 the monthly 1-degree gridded interpolated ARGO SSS field provided by Scripps (www.argo.ucsd.edu/Gridded_fields.html) is used for the reference salinity. An analysis has shown that it is more reliable than the HYbrid Coordinate Ocean Model, called HYOCM, salinity field (HYCOM 2012), which had been used in earlier versions. At high latitudes (above 65^o N/S) and very close to land where no ARGO data exist, V5.0 uses the HYCOM salinity as reference field.

Given this reference salinity value along with all the ancillary data needed to retrieve salinity, an expected TOA T_B is computed. Using the Faraday rotation angle computed using (46), the inverse of equation (45) is applied to convert the expected TOA T_B to an expected TOI T_B. The inverse $\mathbf{A^{-1}}$ of the APC matrix is then used to convert the TOI T_B to an expected antenna temperature value (44). Finally, all of the various space radiation terms are added back (40) thereby obtaining an expected T_A measurement denoted as $T_{A,exp}$.

If the forward model was correct and the retrieved salinity was used instead of the reference salinity field, $T_{A,exp}$ would closely match the measurement $T_{A,mea}$. The two are not exactly the same because the models for both V-pol and H-pol are not perfect and do not include things such as radiometer noise. But to a good approximation, the difference $T_{A,mea}$ - $T_{A,exp}$ is a mapping into T_A space of the difference of the retrieved salinity minus the reference field salinity. Although they

are not expected to be the same on a local basis (i.e. for each individual measurement) they should be close on global basis and over long time (weeks and months) because the Argo sampling should be more and more reasonable as the scale (time and space) gets larger. The $T_{A,mea}$ - $T_{A,exp}$ on a global scale is used in the calibration for determining calibration parameters and correcting the calibration drift (Section 7.1). It is also used in assessing degradation of the salinity retrievals (Meissner 2014b), determining Q/C flags (Le Vine and Meissner 2014) and estimating uncertainties of various components of the salinity retrieval algorithm (Section 8.3).

3.9 Correction for Radiation from Land Surfaces Entering the Antenna Sidelobes

A correction for land entering the antenna sidelobes when the Aquarius observation is close to land is found by running the Aquarius on-orbit simulator. Simulations have shown that the salinity retrieval degrades quickly as the footprint approaches land (closer than 400 km). This land-contamination error, which occurs because the land is much warmer than the ocean is described by Wentz (2006). The error due to land entering the sidelobes, is defined as

$$\Delta\mathbf{T}_{\mathbf{BE},toa} = \hat{\mathbf{T}}_{\mathbf{BE},toa} - \overline{\mathbf{T}}_{\mathbf{BE},toa} \tag{53}$$

which is the difference of the TOA T_B, estimated from the observed (i.e. measured) signal as given by equation (45), minus the true TOA T_B coming from the antenna main beam and defined by (41). The Aquarius simulator is used to compute $T_{BE,toa}$ and produce a table of $\mathbf{\Delta T_{BE}}$,toa. This table is stratified according to the spacecraft nadir longitude (2881 elements in 0.125° increment), the spacecraft position in orbit (i.e. z-angle) (2881 elements in 0.125° increment), month (12 elements), polarization (V-pol, H-pol), and horn (inner, middle, and outer) and takes the form Tb_land_correction(2881, 2881,12,2,3). $\mathbf{\Delta T_{BE}}$,toa is found by linearly interpolating the table to the exact spacecraft position. The interpolated value of $\mathbf{\Delta T_{BE}}$,toa is then subtracted from the actual TOA T_B coming from equation (45) in the retrieval, and then the retrieval process proceeds as usual. The third dimension of month is required to account for seasonal variability in the land brightness temperatures, although this effect is fairly minor. Note that the land correction tables do not consider sea ice. We do the land correction only when the antenna gain-weighted fractional land contamination g_{land} (Section 4.6) exceeds 0.0005 to avoid unnecessarily adding noise for observations very far from land. Also, it is to be emphasized that this "land correction" is only correcting for the

presence of land in the antenna sidelobes. When it approaches the main beam, a different type of correction is likely necessary.

The near-sidelobe correction for land contamination is implemented in the salinity retrieval algorithm after performing the APC (Section 3.3). In the computation of the expected antenna temperature (Section 3.8) it has not been added. The reason is that $T_{A,exp}$ is designed to be used (e.g. for calibration) over open ocean scenes, where the land contamination is negligible. This saved computational time which was an important consideration when Aquarius was operational.

4. Ancillary Fields

This section describes the sources and implementation of the ancillary fields that are used in the Aquarius V5.0 salinity retrieval algorithm.

4.1 Sea Surface Temperature

As part of the preparation for V5.0, an evaluation was made of the performance of the SSS retrieval algorithm with various ancillary SST fields (Meissner et al. 2016). The result of the analysis was that the best performance is obtained with the daily GHRSST (Gridded High-Resolution SST) Level 4 field from the Canadian Meteorological Center (CMC). It is gridded at 0.2^{o} resolution and available from the PO.DAAC web site (https://podaac.jpl.nasa.gov/dataset/CMC0.2deg-CMC-L4GLOB-v2.0). Version 5.0 uses this ancillary SST field. The CMC field is linearly interpolated in space and time to the boresight location of the Aquarius observation.

4.2 Atmospheric Profiles

The atmospheric profiles for pressure, temperature, relative humidity, and cloud water mixing ratio are obtained from the NCEP GDAS (General Data Assimilation System) 1-deg 6-hourly fields. They are available from http://nomads.ncep.noaa.gov/. Using the method described in Section 2.3.2 the fields for the atmospheric transmittance, τ, the upwelling atmospheric temperature T_{BU} and the downwelling atmospheric temperature T_{BD} are calculated from the atmospheric profiles. All fields are linearly interpolated in space and time to the boresight location of the Aquarius observation.

4.3 Wind Speed Background Field

The NCEP GDAS 1-deg, 6-hour scalar wind speed field is used as background field in the Aquarius wind speed retrievals (Section 5.2). It is available from http://nomads.ncep.noaa.gov/. It is linearly interpolated in space and time to the boresight location of the Aquarius observation.

4.4 Wind Direction

The NCEP GDAS 1-deg, 6-hour scalar wind direction field is used in the surface roughness correction (Section 5.3) and in the Aquarius wind speed retrievals (Section 5.2). It is available from http://nomads.ncep.noaa.gov/. It is linearly interpolated in space and time to the boresight location of the Aquarius observation.

4.5 Solar Flux

The daily values of the mean noon-time solar flux are needed in the computation of the direct, reflected, and backscattered solar radiation (Sections 2.2.3 - 2.2.5). They are obtained from the US Air Force Radio Solar Telescope sites using the values at 1415 MHz and are available from the NOAA Space Weather Prediction Center, www.swpc.noaa.gov.

4.6 Land Mask and Land Fraction

We use the static 1-km land/water mask from the OCEAN DISCIPLINE PROCESSING SYSTEM (ODPS). It is based on World Vector Shoreline (WVS) database and World Data Bank and was provided as courtesy of Fred Patt, Goddard Space Flight Center, frederick.s.patt@nasa.gov.

From the land mask two values of the land fraction are computed. The first one, called f_{land}, is defined as the fraction of land area within an antenna 3 dB footprint, where the land area consist of the sum of 1-km land pixels that fall within the footprint. Its value is not provided in the Level 2 files. A second land fraction, called g_{land}, is the fractional land area weighted by the antenna gain pattern, and the integration is taken over the whole Earth field of view. g_{land} is defined and computed as:

$$g_{land} = \frac{1}{4\pi}\int d\Omega \left[\frac{G_{VV}(\mathbf{b}) + G_{HH}(\mathbf{b})}{2}\right] \cdot F_{land}(\mathbf{b}) \tag{54}$$

See section 2.1 for details including the definitions of G and $\mathbf{b}$. The value of the kernel function $F_{land}(\mathbf{b})$ is 1 if the pointing vector $\mathbf{b}$ intersects the land mask, otherwise it is 0. In order to speed up processing, the salinity retrieval uses tables that were pre-computed computed from the orbit

simulator; the tables are structured like the tables for near-sidelobe correction from land surfaces (Section 3.9). In the case of the land correction $F_{land}(\mathbf{b})$ is the land model TB over land, and in case of gland it is either 1 or 0. The correction tables for g_{land} depend on the spacecraft nadir longitude, on spacecraft orbit position (z-angle) and on horn and thus have the dimension g_land (2881, 2881, 3).

The value of g_{land} is provided in the Level 2 files. It is used for quality control and flagging indicating the degradation of the salinity retrievals in the vicinity of land (Meissner 2014b; Le Vine and Meissner 2014). Note, that the value of g_{land} is never exactly zero, as even over the open ocean there is radiation from far sidelobes that comes from land surfaces.

4.7 Sea Ice Mask and Sea Ice Fraction

The ancillary product and the computation for the sea ice fractions have been updated in V5.0 to better match changes in Aquarius TB induced by sea ice entering the field of view (FOV). A summary of the changes is provided here. More details can be found in Dinnat and Brucker (2016).

The following data sets were used for creating the sea ice mask for V5.0:

1. AMSR-E Bootstrap algorithm : Time: 08-25-2011 – 10/04/2011. The data source is ftp://n5eil01u.ecs.nsidc.org/SAN/AMSA/AE_SI12.003/.
2. SSMIS Bootstrap algorithm. Time: 10/05/2011 – 07/02/2012, and 05/10/2013 – 05/14/2013. The data source is: ftp://sidads.colorado.edu/pub/DATASETS/nsidc0079_gsfc_bootstrap_seaice/.
3. AMSR2 Bootstrap algorithm. Time: 07/03/2012 – 06/07/2015, excluding 05/10/2013 – 05/14/2013. The data source is: gcom-w1.jaxa.jp.

Like for the land fraction, we compute a fractional sea ice area f_{ice} and an antenna gain weighted sea ice fraction g_{ice}, which is defined analogous to (54) with the difference that the kernel function is an ice fraction between 0 and 1 derived from the products listed above.

The value of g_{ice} is provided in the Level 2 files. As in the case of g_{land}, it is used for quality control and flagging to indicate the degradation of the salinity retrievals in the vicinity of sea-ice (Meissner 2014b; Le Vine and Meissner 2014).

4.8 Reference Salinity

The reference salinity field, S_{ref}, is not used in the salinity retrieval algorithm itself. It is used in the computation of the expected TA (Section 3.8), and the ocean target calibration (Section 7.1). The SSS_{ref} is used in the computation of TB for a flat ocean surface.

The reference salinity field for V5.0 is the monthly 1-degree gridded interpolated ARGO SSS field provided by Scripps (http://www.argo.ucsd.edu/Gridded_fields.html). It is linearly interpolated in space and time to the boresight location of the Aquarius observation. At high latitudes (above 65 N/S) and very close to land where no ARGO data existV5.0 uses the HYCOM salinity (HYCOM 2012) as reference field, after linearly interpolating in space and time to the Aquarius observation.

There is one place in the salinity retrieval algorithm, where an external 1st-guess salinity field is input. That is the calculation of the reflected galactic radiation (Section 2.2.2) and the reflected solar radiation (Section 2.2.4). It is needed to adjust the tabulated values, which were computed with a nominal salinity value of 35 psu, to the actual value at the time and location of the Aquarius observation. For this purpose, we use the space-time interpolated HYCOM salinity field.

4.9 Rain Accumulation Product and Rain Rate

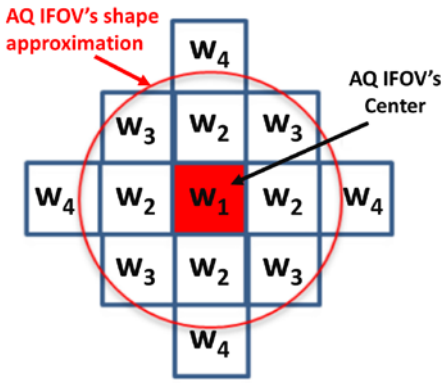

Figure 3: Spatial model used to calculate average instantaneous rain rate and rain accumulation over an Aquarius IFOV. Boxes are 0.25° lat/lon grid cells.

The Aquarius Rain Accumulation (RA) product (Santos-Garcia et al. 2014a, 2014b, 2016) is used to provide an ancillary data set that aids users of the V5.0 Aquarius Level 2 data to better understand the salinity stratification changes due to rain. This product provides the rain history over the 24 hours prior to the Aquarius measurement time and provides a quantitative estimate of the surface salinity stratification. This Aquarius RA product was an initiative that made possible the development of the Rain Impact Model (RIM) that was initially applied to Aquarius and further extended to other data sets such as SMOS (Santos-Garcia et al. 2014b, 2016). This RA data product is an overlay of the Aquarius L2 science data product (SSS retrieval) that contains relative probability of salinity stratification (PS), rain beam fraction (BF), instantaneous rain rate (IRR) averaged over the IFOV (Individual Field of View) and rain accumulation (RA) over the previous 24 hours. The product uses as input the surface rain rates from the NOAA CMORPH (CPC-Climate Prediction Center-Morphing technique) global precipitation data set (Joyce et al. 2004). The average instantaneous rain rate is calculated using a structure of 13 CMORPH pixels around the center of the Aquarius IFOV as is shown in Figure 13, where the weight associated with each pixel is based on the antenna gain. More detailed information about the dataset are found in the document "Readme file for the CFRSL – Rain Impact Model (RIM) v1.2 for Aquarius" associated with the RIM data set. A subset of essential RIM parameters is included in the Aquarius V5.0 L2 product, e.g. IRR, PSS, BF, rain impacted ancillary salinity (HYCOM) and the salinity change caused by rain at the surface (0.05 meters in depth) and at 1, 3 and 5 meters below surface.

None of the RA products are directly used in the salinity retrievals. The IRR is used as quality control in the ocean target calibration (Section 7.1) for rain filtering.

5. Wind Induced Surface Emissivity Model and Surface Roughness Correction

The wind induced emissivity model and surface roughness correction for the Aquarius salinity retrieval algorithm is described in Meissner et al. (2014). In V5.0 a few changes were implemented. The main reasons for the changes were changes in the geophysical model and changes in the ancillary fields (SST, ancillary SSS) implemented since the derivation of the wind induced emissivity used in earlier versions(Meissner et al. 2014). The wind induced emissivity is obtained by comparing the TB at the (rough) surface retrieved from the measurements with the TB computed for a flat ocean surface ($T_{Bsur,0}$). Particularly important changes of the geophysical model (i.e. the forward model for TB_expected) that affect the derivation of the wind induced emissivity are: 1) the change in the oxygen absorption model from Wentz and Meisner (2016) to Liebe et al. (1992), 2) the change of the external ancillary SSS field that is used in the computation of $T_{Bsur,0}$ from HYCOM to Scripps ARGO, and 3) the change in the ancillary SST that enters the computation of $T_{Bsur,0}$ from the NOA OI SST to the CMC SST. The following subsection describe the updates made since the description provided in Meissner et al. (2014).

5.1 Model for Wind Induced Surface Emissivity

5.1.1 Model Components

The model for the wind induced surface emissivity has two terms (Meissner et al., 2014):

$$\Delta E_{rough} = \Delta E_{W0}\left(W, \varphi_r, T_S\right) + \Delta E_{W1}\left(W, \sigma'_{0,VV}\right) \tag{54}$$

Here, W is the surface wind speed and T_S is the sea surface temperature. The wind direction, $\varphi_r = \varphi_W - \alpha$ where φ_W, is the geographical wind direction relative to North and α is the azimuthal look direction relative to North. An upwind observation has $\varphi_r = 0°$, a downwind observation has $\varphi_r = 180°$ and crosswind observations have $\varphi_r = +/-90°$. The value for φ_w comes from the ancillary NCEP GDAS field. The wind speed, W, is derived from Aquarius scatterometer HH-pol and radiometer H-pol measurements (Section 5.2).

The $\sigma'_{0,VV}$ is obtained from the observed VV-pol scatterometer cross-section $\sigma_{0,VV}$ after removing the wind direction effect:

$$\sigma'_{0,VV} \equiv \sigma^{meas}_{0,VV} - \left[B_{1,VV}\left(W_{HHH}\right)\cdot\cos\left(\varphi_r\right) + B_{2,VV}\left(W_{HHH}\right)\cdot\cos\left(2\cdot\varphi_r\right)\right] \tag{55}$$

See Appendix A for a description of the terms in brackets in (55). The 2nd order term $\Delta E_{W2}\left(W, SWH\right)$ included in Meissner et al. (2014), and which depends on significant wave height (SWH), has subsequently been found to be small and is omitted in the Version 5.0 algorithm.

The 1st term ΔE_{W0} on the right hand side of (54) has a weak dependence on SST which can be separate out as follows:

$$\Delta E_{W0,p} = \delta_p\left(W,\varphi_r\right)\cdot\rho_p\left(T_S\right) \quad p = V,H \tag{56}$$

The two terms in (56) are discussed separately below in Sections 5.1.2 and 5.1.3.

5.1.2 Harmonic Coefficients of Wind Induced Surface Emissivity Model

The model function $\delta_p\left(W,\varphi_r\right) \quad p = V,H$ in (56) can be expanded into an even 2nd order harmonic expansion in the relative wind direction φ_r (Meissner et al. 2014):

$$\delta_p\left(W,\varphi_r\right) = A_{0,p}\left(W\right) + A_{1,p}\left(W\right)\cdot\cos\left(\varphi_r\right) + A_{2,p}\left(W\right)\cdot\cos\left(2\cdot\varphi_r\right) \tag{57}$$

The harmonic coefficients $A_{k,p}, k = 0,1,2$ depend on surface wind speed *W*, polarization p =V, H, and Erath Incidence Angle EIA (i.e. different for each beam). $A_{k,p}\left(W\right)$ is fitted by a 5th order polynomial in *W*, which vanishes at *W = 0*:

$$A_{k,p}\left(W\right) = \sum_{i=1}^{5} a_{ki,p}\cdot W^i \tag{58}$$

The coefficients $a_{ki,p}$ {i=1, ...5} , k={0,1,2} p={V,H} have been determined empirically (Meissner et al., 2014) from a match-up data set consisting of the Aquarius radiometer T_B observations and wind speed measurements from WindSat (Wentz et al. 2013) and F17 SSMIS (Wentz et al. 2012).

Formatted ASCII files for the coefficients $a_{ki,p}$ are provided in the supplementary files (Appendix D).

For each $A_{k,p}$ there is a maximum wind speed $W_{k,p}^{\max}$ above which the values of $A_{k,p}(W)$ are calculated by linear extrapolation instead of (58). The values of $W_{k,p}^{\max}$ are also listed in the supplementary files (Appendix D).

5.1.3 SST Dependence of Wind Induced Surface Emissivity

The functional form of the SST dependence in (56) used in Version 5.0 has been updated from the one given in Meissner et al. (2014), and reads now:

$$\rho_p(T_S) = \left[\frac{E_{0,p}(T_S)}{E_{0,p}(T_{ref})} + \rho'_p(T_S) \right] \quad p = V, H \tag{59}$$

where the change from Meissner et al. (2014) is the addition of the term ρ'. The expressions $E_{0,p}(T_S)$ are the emissivities of the ideal half-space (air above flat ocean surface) and given by the Fresnel reflectivity as before. The reference temperature is $T_{ref} = 20^{\circ}C$.

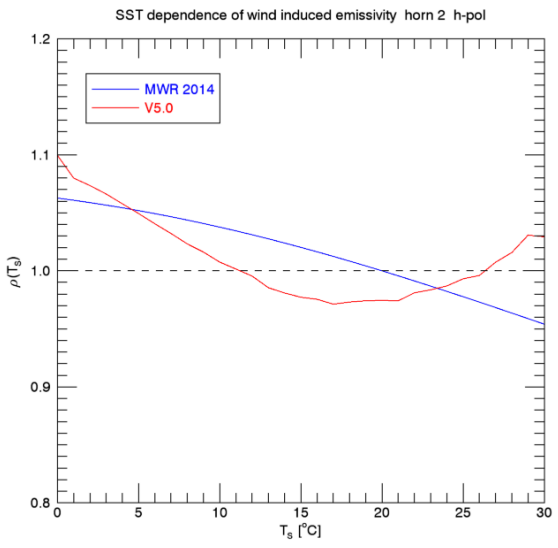

Figure 4: SST dependence of the wind induced emissivity for horn 2 H-pol. Black dashed line = no SST dependence. The blue line in the SST dependence from Meissner et al. (2014). The red curve is the SST dependence $\rho(T_S)$ in (59) that is used in V5.0.

The 1st term on the right-hand side of (59) is the same SST dependence of the wind induced emissivity that one would expect to find in the geometric optics (GO) model. The 2nd term can be regarded as an empirical correction to the SST dependence predicted by the GO model. The form of $\rho(T_S)$ for horn 2 H-pol is shown in Figure 4. Formatted ASCII tables for the functions $\rho'(T_S)$ for the 6 Aquarius channels are provided in the supplementary files (Appendix D).

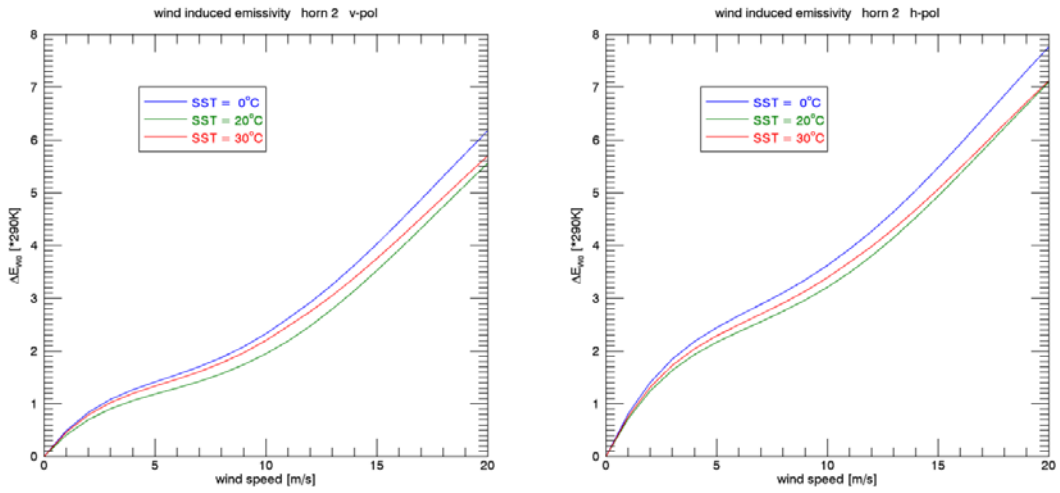

Figure 5: The wind induced emissivity ΔE_{W0} for horn 2 that is used in V5.0 as function of wind speed for 3 different SST values. Left: V-pol. Right: H-pol.

Making this modification to the SST dependence in the wind induced emissivity model from Meissner et al. (2014) is supported by the data for low and intermediate wind speeds $W < W_c = 11 \, m/s$. At high wind speeds $W \geq W_c = 11 \, m/s$ the value of the additional term in (59) is kept constant at its value at W_c, which is also supported by the data. That means that for high wind speeds $W \geq W_c$ the term $\Delta E_{W0,p}$ from equation (56) is given by:

$$\Delta E_{W0,p} = \delta_p(W, \varphi_r) \cdot \frac{E_{0,p}(T_S)}{E_{0,p}(T_{ref})} + \delta_p(W_c, \varphi_r) \cdot \rho'_p(T_S) \qquad (60)$$

and the slope of $\Delta E_{W0}(W_S)$ at high wind speeds is still the same for V5.0 as the one derived in Meissner et al. (2014). There are several physical mechanisms that can cause microwave emission from the wind roughened surface (tilted facets, Bragg scattering from capillary waves, emission from sea foam or sea spray, …). These mechanisms have different magnitudes in different wind speed regimes and it is possible that they also have different dependence on SST. That is to say, the SST dependence of ΔE_{W0} can be different at high winds than at low or intermediate winds as modelled here for V5.0.

Figure 5 compares the wind-speed dependence of ΔE_{W0} in V5.0 for horn 2 at 3 different SST values. All curves show reasonably smooth behavior as function of wind speed W.

5.1.4 Lookup Table for $\Delta E_{W1}(W_{HHH}, \sigma'_{0,VV})$

The lookup table for $\Delta E_{W1}(W_{HHH}, \sigma'_{0,VV})$ has been also been rederived for V5.0 and its values are slightly different from the ones in Meissner et al. (2014). The updated values are provided in the supplementary files (Appendix D).

5.2 Aquarius Wind Speed Retrievals

The surface roughness correction in Aquarius V5.0 uses wind speeds as input that are derived from Aquarius scatterometer and radiometer measurements (Meissner et al. 2014).

Two Aquarius wind speed products are retrieved:

1. HH wind speeds, which use the scatterometer σ_0 at HH-pol.
2. HHH wind speeds, which use the scatterometer σ_0 at HH-pol and the radiometer TB at H-pol.

The retrieval for both wind speed products is based on a maximum likelihood estimate (MLE):

The sum of squares (SOS) in the MLE for the HH wind speed algorithm is:

$$\chi^2_{HH}(W) = \frac{\left[\sigma^{measured}_{0,HH} - \sigma^{GMF}_{0,HH}(W, \varphi_r)\right]^2}{\mathrm{var}(\sigma_{0,HH})} + \frac{\left[W - W_{NCEP}\right]^2}{\mathrm{var}(W_{NCEP})} \quad (61)$$

The SOS in the MLE for the HHH wind speed algorithm is:

$$\chi^2_{HHH}(W) = \frac{\left[\sigma_{0,HH}^{measured} - \sigma_{0,HH}^{GMF}(W,\varphi_r)\right]^2}{\mathrm{var}\left(\sigma_{0,HH}\right)} + \frac{\left[\Delta T_{B,surf,H}^{measured} - \Delta T_{B,surf,H}^{GMF}(W,\varphi_r)\right]^2}{\mathrm{var}\left(T_{B,surf,H}\right)} + \frac{\left[W - W_{NCEP}\right]^2}{\mathrm{var}\left(W_{NCEP}\right)} \quad (62)$$

The radar cross sections, $\sigma_0^{measured}$ are the values observed by the scatterometer at the top of the atmosphere and available in the L2 data file as scat_X_toa. The value of $\Delta T_B^{measured}$ is obtained from the measured brightness temperature propagated to the surface (i.e. removing extraneous radiation and correcting for Faraday rotation and atmospheric attenuation). From this measured surface brightness temperature the brightness temperature of a specular (flat) ocean surface is subtracted in order to get $\Delta T_B^{measured}$.

The form of the geophysical model function $\sigma_{0,HH}^{GMF}(W,\varphi_r)$ is given in Appendix A. The form of the geophysical model function $\Delta T_{B,surf,H}^{GMF}(W,\varphi_r)$ is given by the expression for $\Delta E_{W0,p=H}$ in equation (56) multiplied by sea surface temperature T_S. The values of the expected variances $\mathrm{var}\left(\sigma_{0,HH}\right)$, $\mathrm{var}\left(T_{B,surf,H}\right)$ and $\mathrm{var}\left(W_{NCEP}\right)$ are listed in the supplementary files (Appendix D). For additional information see (Meissner et al. 2014).

For both the HH and HHH wind speed MLE we have found that assimilating the ancillary NCEP wind speed W_{NCEP} as background field into the MLE (i.e. the last term on the right in (61) and (62)) improves the skill at cross-wind observations, where the scatterometer cross section loses sensitivity. In both cases the wind direction $\varphi_r = \varphi_W - \alpha$ is obtained from the ancillary NCEP GDAS field φ_W .

In order to compute the value of $\Delta T_B^{measured}$ in Eqn. (62) we need to subtract the brightness temperature of the specular surface from the measured brightness temperature propagated to the surface. The computation of the specular part requires both values for the SST and a 1st guess field for SSS as input. For SST we take CMC SST (Section 4.1), which is already used as auxiliary input in the L2 algorithm. For V5.0, the 1st guess salinity field is a monthly 2° climatology of salinity maps that have been retrieved from Aquarius data using HH wind speeds in the roughness correction.

We have tested that including the scatterometer VV-pol or the radiometer V-pol into the MLE (61) or (62) does not lead to a significant improvement in the performance of either wind speed product or the final SSS product. But note that the scatterometer VV-pol measurement $\sigma_{0,VV}$ is used in the calculation of the wind induced emissivity (Section 5.1.4).

A validation study of the HH and HHH wind speeds (Meissner et al. 2014) shows that the quality of the Aquarius HHH wind speeds matches those of WindSat (Wentz et al. 2013) and F17 SSMIS (Wentz et al. 2012). We estimate its overall accuracy to about 0.6 m/s. The overall accuracy of the HH wind speed is slightly less. Major degradation of the HH wind speeds occurs at higher winds (> 15 m/s) due to the loss of sensitivity of the scatterometer HH-pol cross section to wind speeds. The radiometer H-pol TB keeps its sensitivity to wind speed even in high winds (Meissner et al. 2014).

It should be noted that the HH wind speed is different from the wind speed that is produced by the scatterometer algorithm (Yueh et al. 2013), which uses both VV-pol and HH-pol scatterometer observations.

5.3 Surface Roughness Correction

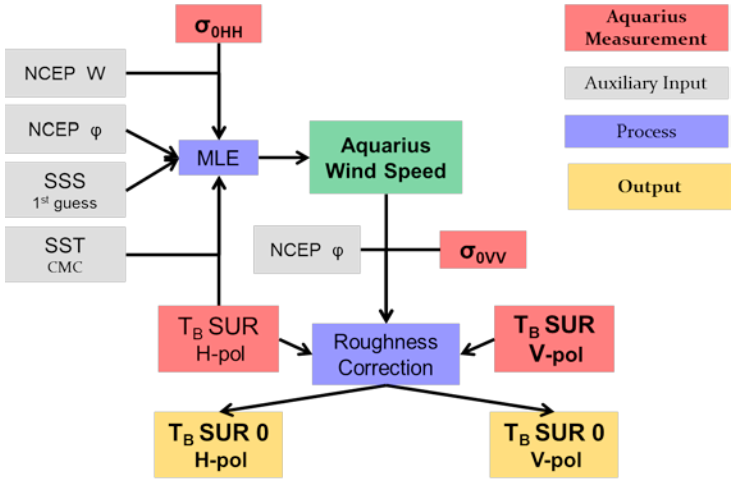

Figure 6: Flow diagram of Aquarius wind speed retrieval (section 5.2) and surface roughness correction (section 5.3).

The surface roughness correction removes the T_B of the wind induced emission from the Aquarius surface $T_{BE,sur}$ in order to get the $T_{BE,sur,0}$ that is emitted by a flat (specular) ocean surface:

$$T_{BE,sur,0} = T_{BE,sur} - \Delta E_{rough}\left(W, \varphi_r, T_S, \sigma'_{0,VV}\right) \cdot T_S \tag{63}$$

where ΔE_{rough} is given by (54).

In the L2 algorithm the HH wind speeds are used ($W=W_{HH}$) in (63) as auxiliary fields at stages where no well-calibrated radiometer measurement is yet available. This is the case for the calibration drift correction and also for the removal of reflected galaxy or solar radiation. The HHH wind speed ($W=W_{HHH}$) is used in (63) in the final surface roughness correction.

For many observations with high land contamination (antenna pattern weighted land fraction > 0.1) or high sea ice contamination (antenna pattern weighted land fraction > 0.1) neither the HH nor the HHH wind speed retrieval converge. If the land or sea ice fractions exceed 0.1, we do not retrieve HH or HHH wind speeds but use the NCEP wind speed in the surface roughness correction (that is $W=W_{NCEP}$ in (63)).

Figure 6 shows a schematic flow-chart of the Aquarius wind speed retrieval and surface roughness correction.

6. Reflection of Galactic Radiation from Rough Ocean Surfaces

This section gives the details of the calculation of the reflected galactic radiation (Section 2.2.2) from a rough ocean surface. In Section 2.2.2, the received reflected galactic radiation $\mathbf{T_{A,gal\_ref}}$ is given in (14) for a specular surface as an integral over the antenna pattern. Inside the integral is the term $\mathbf{T_{B,gal\_ref}}$ which represents the brightness temperature of the incident reflected galactic radiation at the top of the atmosphere. In the case of a rough surface, a first correction is made using Geometric Optics (GO), which models the rough ocean surface as a statistical ensemble of tilted facets (Section 6.1). The GO model is able to remove the reflected galactic radiation correctly to about 90%. The remaining 10% shows up as spurious signal in the Aquarius salinity retrieval and manifests itself in differences between the morning (descending) and the evening (ascending) swaths over the same ocean. The main reason for the (10%) deficiency in the galactic reflection model is the limitation of the analytical modeling of the rough surface. Aquarius version 5.0 uses several empirical corrections and adjustments to the GO calculation in order to mitigate this residual error. The 1st one is based on the difference between fore and aft observations from the Soil Moisture Active Passive (SMAP) mission and explained in Sections 6.2 and 6.3. The 2nd one is based on the expected equivalence of the salinity retrieved during the ascending and descending Aquarius swaths. This is discussed in Section 6.4.

6.1 Geometric Optics Calculation for the Reflected Galactic Brightness Temperature

The rough ocean surface is modeled as a collection of tilted facets, with each facet acting as an independent specular reflector. The formulation for this model is given by Wentz (1978). Equation (7) in Wentz (1978) can be rewritten as

$$T_B\left(\mathbf{k_s}, \mathbf{P_s}\right) = \tau^2 \iint d\Omega_i \, k_i^z \Gamma\left(\mathbf{k_i}; \mathbf{k_s}, \mathbf{P_s}\right) T_B\left(\mathbf{k_i}\right) \tag{64}$$

where $T_B(\mathbf{k_s}, \mathbf{P_s})$ is the top of the atmosphere scattered galactic radiation propagating in the direction of the unit vector $\mathbf{k_s}$ having polarization $\mathbf{P_s}$. The vector $\mathbf{k_i}$ is the downward propagation vector from the galaxy. $T_B(\mathbf{k_i})$ is the brightness temperature of the galaxy coming from direction $\mathbf{k_i}$. It comes from the Le Vine and Abraham (2004) map after subtraction of the 3 K floor (see Section 2.2.2). The term $\Gamma(\mathbf{k_i}; \mathbf{k_s}, \mathbf{P_s})$ is the scattering function defined below. The atmospheric transmit-

tance, τ, accounts for attenuation during propagation through the atmosphere. We assume that the transmittance is the same for the downwelling and upwelling radiation. The value of τ along the boresight ray is used and assumed to be the same at all points in the integral (e.g. over the footprint of the antenna). This assumption is dictated by the coarse spatial resolution (100 km) of the NCEP data used to compute τ

The integral is over differential solid angles $d\Omega_i$. In Wentz (1978) the differential solid angle was given in terms of the x,y,z components of $\mathbf{k_i}$.

$$d\Omega_i = \frac{dk_i^x \, dk_i^y}{dk_i^z} \tag{65}$$

where the z axis is aligned with the normal to the Earth's geoid. In doing the integration it is convenient to transform the integral using the following Jacobian (Wentz, 1978):

$$d\Omega_i = 4 \cdot \left(\mathbf{n} \cdot \mathbf{z}\right)^3 \left(\mathbf{k_s} \cdot \mathbf{n}\right) dz_u dz_c \tag{66}$$

where $\mathbf{n}$ is the unit surface normal vector for a particular facet, z_u and z_c and the two slopes of the facet in the upwind and crosswind directions, and unit vector $\mathbf{z}$ is the normal to the Earth's geoid.

$$T_B\left(\mathbf{k_i}, \mathbf{P_s}\right) = \tau^2 \iint dz_u dz_c \, 4 \cdot \left(\mathbf{n} \cdot \mathbf{z}\right)^3 \left(\mathbf{k_s} \cdot \mathbf{n}\right)\left(\mathbf{k_i} \cdot \mathbf{n}\right) \Gamma\left(\mathbf{k_i}; \mathbf{k_s}, \mathbf{P_s}\right) T_B\left(\mathbf{k_i}\right) \tag{67}$$

The scattering function is given by Wentz (1978):

$$\Gamma(\mathbf{k_i}; \mathbf{k_s}, \mathbf{P}_s) = \frac{P_z(z_u, z_c)}{4(\mathbf{k_s} \cdot \mathbf{z})(\mathbf{k_i} \cdot \mathbf{z})(\mathbf{n} \cdot \mathbf{z})^4} \Upsilon \tag{68}$$

$$\Upsilon = |\, \mathbf{P_s^*} \cdot \mathbf{H_s} \,|^2 |\, R_h \,|^2 + |\, \mathbf{P_s^*} \cdot \mathbf{V}_s \,|^2 |\, R_v \,|^2 \tag{69}$$

where P_z is the probability distribution function (pdf) for the facet slopes, and $\mathbf{V_s}$ and $\mathbf{H_s}$ are the local V-pol and H-pol unit vectors of a particular facet (defined with respect to k_i using the radiometer convention). The terms R_v and R_h are the V-pol and H-pol reflectivities for the facet. The superscript * denotes complex conjugate. For specifying R_v and R_h we use the Meissner and Wentz (2004, 2012) dielectric constant for the specular component and the 0^{th} harmonic term of the wind induced emissivity (see Section 5.1 of this ATBD), which is taken from Meissner et al. (2014). Note that there is a small inconsistency in doing this because the Meissner et al. (2014) wind-induced com-

ponent already includes to some degree the roughening effect due to facet tilting. Since the Meissner et al. (2014) wind-induced component also includes the effect of sea foam and Bragg scattering, it is difficult to separate all the effects and we thought it was better to include the wind-induced component as compared to simply using the specular reflectivity in (69). For computing the scattering of galactic radiation this issue is minor, having about a 2% effect on the computation, which translates to a worst-case uncertainty of 0.1 K or less.

Combining terms, we then get:

$$T_B\left(\mathbf{k_s},\mathbf{P_s}\right)=\tau^2\iint dz_u dz_c T_B\left(\mathbf{k_i}\right)\left(\mathbf{k_s}\cdot\mathbf{n}\right)\frac{P_Z\left(z_u,z_c\right)}{\left(\mathbf{k_i}\cdot\mathbf{n}\right)\left(\mathbf{k_s}\cdot\mathbf{n}\right)}\Upsilon \tag{70}$$

The brightness temperature classical stokes vector appearing in equation (14) is then given by

$$\mathbf{T}_{\mathbf{B},gal\_ref}=\begin{bmatrix}T_B\left(\mathbf{k_s},\mathbf{v}\right)+T_B\left(\mathbf{k_s},\mathbf{h}\right)\\T_B\left(\mathbf{k_s},\mathbf{v}\right)-T_B\left(\mathbf{k_s},\mathbf{h}\right)\end{bmatrix} \tag{71}$$

where **v** and **h** are the V-pol and H-pol vectors referenced to the Earth's geoid and $\mathbf{k_s}$ is in the direction of the differential solid angle for the integral shown in (14).

The key issue in computing $T_B(\mathbf{k_s}, \mathbf{P_s})$ is what to use for the facet slope pdf. The classic Cox and Munk (1954) experiment, which measured the ocean sun glitter distribution, clearly showed that to first order the slope pdf is Gaussian. Higher order pdf moments were also observed (skewness and peakedness), and the rms slopes in the upwind direction were found to be somewhat higher than the downwind direction. For L-band microwave observations the higher wavelength components of surface roughness, which are small relative to the L-band wavelength of 21 cm, do not contribute to the facet tilting. Thus, when applying the Cox and Munk results to low-frequency microwave observations, one must reduce the Cox and Munk rms slopes. This is a well-accepted fact and there have been many papers written on the subject, e.g. (Wentz 1983; Wilheit and Chang 1980). However, the exact value of the reduction factor and how it varies with radiation wavelength is still uncertain. For the AMSR-E Algorithm Theoretical Basis Document (Wentz and Meissner 2000), the following was used to specify the facet slope pdf:

$$P_z\left(z_u, z_c\right) = \frac{e^{-\frac{z_u^2+z_c^2}{\sigma^2}}}{\pi\sigma^2} \tag{72}$$

where an isotropic slope distribution was assumed. The total facet slope variance is given by

$$\begin{aligned} \sigma^2 &= 5.22\times10^{-3}W \qquad f \geq 37 \text{ GHz} \\ \sigma^2 &= 5.22\times10^{-3}W\left[1-0.00748\left(37-f\right)^{1.3}\right] \qquad f < 37 \text{ GHz} \end{aligned} \tag{73}$$

where f denotes frequency (GHz) and W is the 10-meter wind speed used elsewhere in this report. For frequencies above 37 GHz, the Cox and Munk clean surface slope variance is used. For frequencies below 37 GHz, the slope variance is decreased as explained in Wentz and Meissner (2000). More recently in Meissner and Wentz (2012), the above expression was replaced by a slightly different expression based on more analysis of satellite data.

$$\sigma^2 = 0.0029W\log_{10}\left(2f\right) \qquad f < 100 \text{ GHz} \tag{74}$$

This is the expression we use for calculating the tables of $\mathbf{T_B}$,gal_ref. At frequencies above 32 GHz, this expression gives a slope variance somewhat higher than Cox and Munk, consistent with the fact that the Cox and Munk value probably represents a lower bound on the true slope variance (Wentz 1978). For f = 1.41 GHz, both (73) and (74) represent approximately a 50% reduction in the Cox-Munk clean surface slope variance. This reduction is similar to the Cox and Munk oil-slick results. Oil was poured on the ocean surface to dampen out the capillary waves. The oil-slick results also indicated a slope distribution that was nearly isotropic, consistent with (72), as compared to the clean surface results that indicated an anisotropic distribution.

The above expressions are then used to compute the term $\mathbf{T_B}$,gal_ref that appears in the equation for reflected galactic radiation $\mathbf{T_A}$,gal_ref. This represents a four-fold integral that needs to be calculated with a numerical precision of better than 0.1 K. To compute all the T_A tables described in Section 2.2.2 required 48 3-GHz processors running for 2 months.

Note that the GO calculation above is only valid over water surfaces. For land, sea-ice, or mixed surfaces the formula (37) is used to compute the surface reflectivity. If the gain weighted land fraction g_{land} (see Section 4.6) exceeds 50%, then simple specular surface reflection of the galactic

radiation is assumed. The same prescription should have been applied if the gain weighted sea-ice fraction g_{ice} (see Section 4.7) exceeds 50%, but this was not implemented. One needs to be aware that the L2 values for the galactic reflection over land, sea-ice or mixed scenes are very rough approximations which have not been validated.

6.2 Analysis of SMAP Fore – Aft Observations

Observations from the SMAP (Soil Moisture Active and Passive) mission (Entekhabi et al., 2010, 2014; Piepmeier et al. 2016), that has been making passive L-band observation since April 2015, provide an opportunity to improve the correction for the reflected galactic signal. SMAP performs a full 360^o scan in less than 5 seconds and thus observes each location almost simultaneously in forward (fore) and backward (aft) direction. The (relatively) strong reflected radiation emanating from the plane of the galaxy can appear in both the forward and the backward look but usually not at the same time. Radiation from directions other than the plane of the galaxy are generally quite small (Le Vine and Abraham, 2004). If all other signals that depend on look direction (Faraday rotation, wind direction, solar and lunar radiation) have been accurately removed (Meissner and Wentz 2016), then taking the difference between fore and aft measured TA produces the galactic radiation:

$$T_{A,gal,ref}\left(\phi_{for}\right)-T_{A,gal,ref}\left(\phi_{aft}\right)=T_A\left(\phi_{for}\right)-T_A\left(\phi_{aft}\right) \tag{75}$$

This equation can be used to derive an empirical galactic correction separate for the SMAP fore and aft looks. For example, looking for cases where the signal from the aft look is small (< 2K) and assuming that the model (theory) for the SMAP aft look reflected galactic radiation is correct if it is smaller than 2 K, then the empirical correction for the fore look can then be obtained from (75) as:

$$T_{A,gal,ref,emp}\left(\phi_{for}\right)=T_{A,meas}\left(\phi_{for}\right)-T_{A,meas}\left(\phi_{aft}\right)+T_{A,gal,ref,model}\left(\phi_{aft}\right) \tag{76}$$

Likewise, assuming that the computed SMAP fore look galaxy model is correct if it is smaller than 2 K, then the empirical galaxy model for the aft look can then be obtained from (75) as:

$$T_{A,gal,ref,emp}\left(\phi_{aft}\right)=T_{A,meas}\left(\phi_{aft}\right)-T_{A,meas}\left(\phi_{fore}\right)+T_{A,gal,ref,model}\left(\phi_{for}\right) \tag{77}$$

When performing the analysis, observations were discarded for which the reflected solar radiation is not negligible. Reflected solar radiation differs between fore and aft looks and currently the correction for reflected solar radiation in the SMAP algorithm is not accurate enough to correct for the difference. It is possible to find observations for all times and orbit positions for which both the reflected solar radiation is negligible and either the TA galaxy of the fore or the aft look are less than 2 K. Therefore, it is possible to derive empirical galactic corrections for SMAP sensor for both look directions using equations (76) and (77). Separate derivations are performed for different wind speed regimes using 5 m/s intervals.

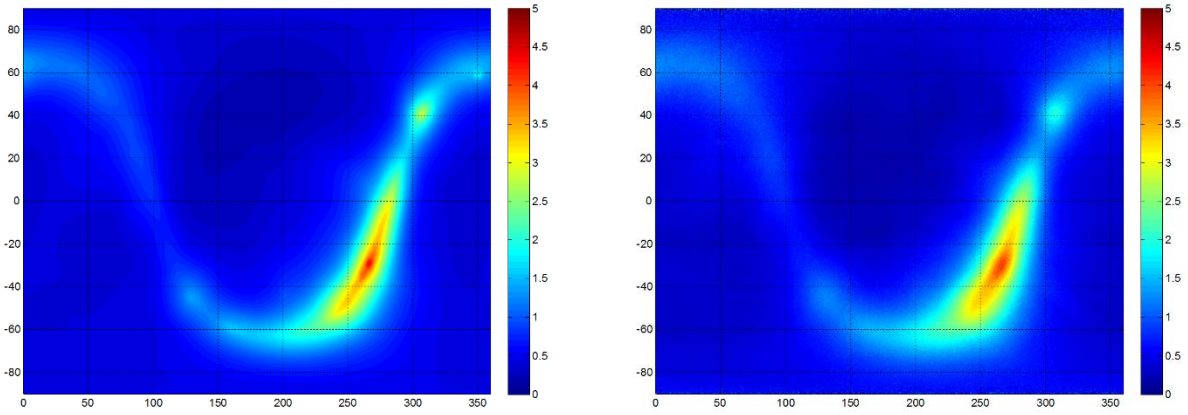

Figure 7: Left: GO model for the SMAP reflected galaxy (Section 6.1) . Right: Empirically derived SMAP reflected galaxy based on fore – aft analysis using equations (76) and (77). In obtaining these figures all observations were averaged together independent of wind speed.

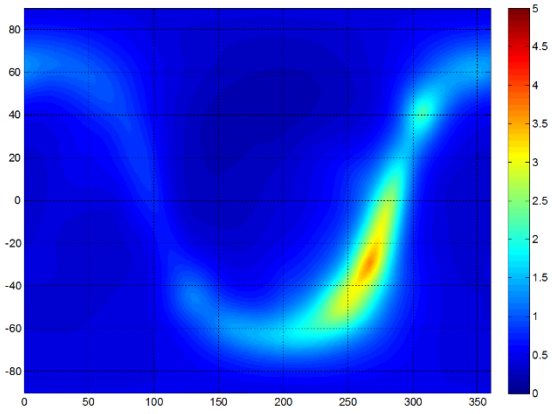

Figure 8: GO model for the SMAP reflected galaxy adding 2 m/s to the wind speed when calculating the slope variance.

The largest part of the SMAP fore – aft results can be reproduced using a tilted facet calculation as explained in Section 6.1 but adding 2 m/s to the wind speed W when calculating the RMS slope variance $\sigma^2(W)$ according to (74). The value of $\sigma^2(W)$ enters the tilted facet integration in the GO model in the facet slope pdf (74). The effective increase in slope variance increases the surface roughness at L-band frequencies and this increase brings the slope variance from equation (74) closer to the Cox-Munk value (73). The effect of this increase is shown in Figure 7, Figure 8 and Figure 9.

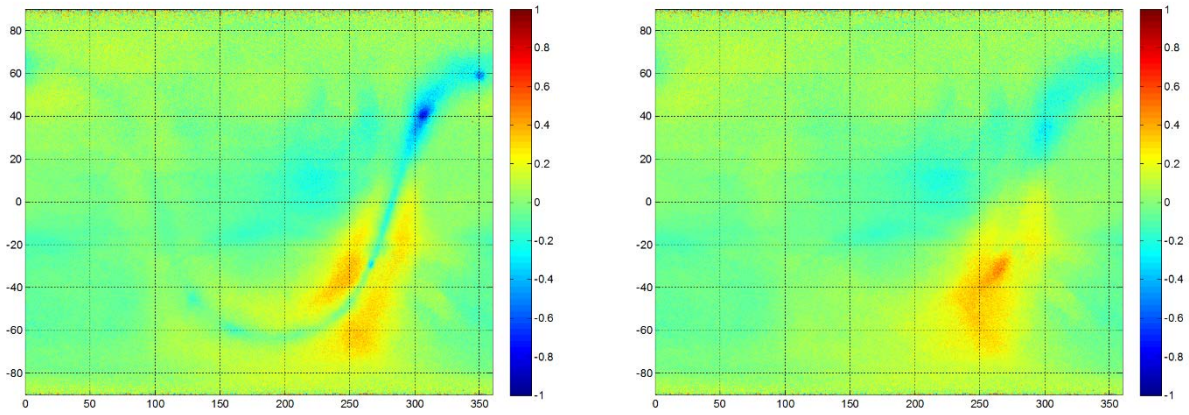

Figure 9: Left: Difference between the galactic map derived from SMAP fore – aft and the GO calculation (Section 6.1). Right: Difference between the galactic map derived from SMAP fore – aft and the modified GO calculation adding 2 m/s in the calculation of the RMS slope. In obtaining these figures all observations were averaged together independent of wind speed.

6.3 Implementation of the SMAP Fore – Aft Results into the Aquarius Algorithm

The first step in implementing the result from the SMAP fore – aft in the estimation of the Aquarius antenna temperature for the reflected galaxy ($T_{A,gal,ref}$) is to compute the geometric optics value ($T_{A,go}$). $T_{A,go}$ is a function of time (t = sidereal year), the intra-orbit position of the Aquarius spacecraft (ϕ), and sea-surface wind speed (W). Tables of $T_{A,go}(t, \phi, W)$ are pre-computed using the Aquarius on-orbit simulator. For operational processing, $T_{A,go}$ for a given observation is found from a tri-linear interpolation of the $T_{A,go}(t, \phi, W)$ table. There are nine separate tables corresponding to the 3 horns and the first 3 Stokes parameters. Sections 2.2.2 and 6.1 of this ATBD give the details of how this is done.

The next step to implement the SMAP-derived adjustments, 2 m/s is added to the wind when computing $T_{A,go}$ as described in the paragraph above. The SMAP results (Sections 6.2 and 6.3) indicated the smoothing of the galaxy radiation due to 1) the integration over the Aquarius antenna and 2) the scattering from the rough ocean surface was greater than predicted by the geometric optics model. Adding 2 m/s to the input wind speed mitigated this problem.

After adding the 2 m/s, there is still some residual differences between the SMAP derived galaxy and $T_{A,go}$. To remove the residuals, adjustment tables are computed. These tables are a function of the galactic longitude α, galactic latitude β, and wind speed W. The tables are denoted by $\Delta T_{A,go}(\alpha, \beta, W)$, and there are separate tables for V-pol and H-pol.

Let $T_{A,gal,ref,smap}$ be the reflected galactic T_A found directly from the fore-minus-aft SMAP differences. Let $T_{A,go}(t, \phi, W+2)$ be the reflected T_A from the geometric optics model with 2 m/s added to the wind. The adjustment table $\Delta T_{A,go}(\alpha, \beta, W)$ is then found by averaging over a year of SMAP observations.

$$\Delta T_{A,go}(\alpha,\beta,W) = \left\langle T_{A,gal,ref,smap} - T_{A,go}(t,\phi,W+2) \right\rangle_{\alpha,\beta,W} \tag{78}$$

where the brackets indicated a one-year average into 0.25^o α-bins, 0.25^o β-bins, and 5 m/s wind bins. The reflected galactic T_A used for Aquarius processing is then

$$\tilde{T}_{A,gal,ref} = T_{A,go}(t,\phi,W+2) + \Delta T_{A,go}(\alpha,\beta,W) \tag{79}$$

An additional constraint is applied to this procedure. Results indicated that the polarization ratio (V-pol/H-pol) for $T_{A,gal,ref,smap}$ was somewhat noisy. Accordingly, we constrain the polarization ratio of the SMAP-derived reflected galaxy to be the polarization ratio predicted by geometrics optics. The following scaling accomplishes this:

$$T_{A,gal,ref,smap,v} = T_{A,gal,ref,smap,h} \frac{T_{A,go,v}(t,\phi,W+2)}{T_{A,go,h}(t,\phi,W+2)} \tag{80}$$

Thus, we rely just on the H-pol $T_{A,gal,ref,smap}$ to characterize galactic reflections. The surface reflectivity of H-pol is about twice that of V-pol, and hence H-pol has the stronger galactic signal (i.e. greater signal-to-noise).

The changes in the Aquarius reflected galaxy based on the SMAP fore – aft data are shown in Figure 10 for horn 2 as an example.

These changes are applied in the calculation of the reflected galaxy radiation. The calculation of the direct galaxy radiation has not been changed from Section 2.2.1 of this ATBD and is still using the original galactic maps of Le Vine and Abraham (2004) and Dinnat et al. (2010).

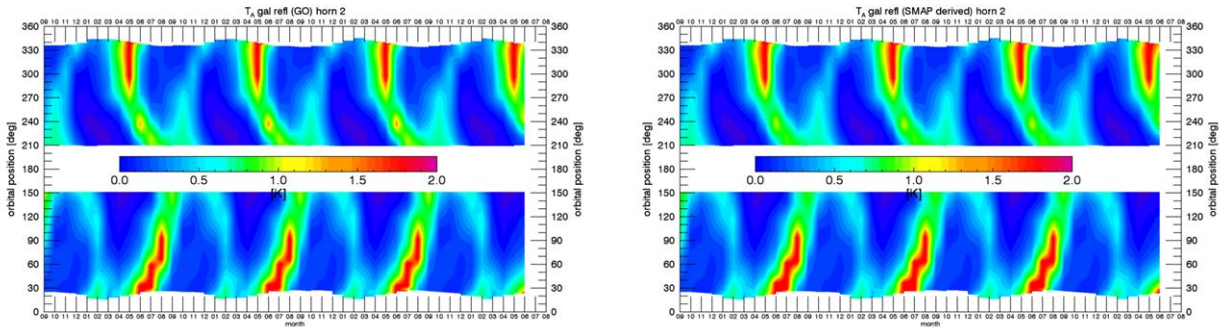

Figure 10: Reflected galaxy for Aquarius horn 2. Left: GO calculation as specified in ATBD, Version 2. Right: GO calculation after the adjustments based on the SMAP fore – aft look.

In order to evaluate the improvement of the SMAP derived adjustments to the reflected galaxy, the Aquarius salinity retrievals were run first with the correction based on GO alone (Section 6.1) and then with the SMAP derived adjustments. The improvements in TA measured minus expected are shown in Figure 11.

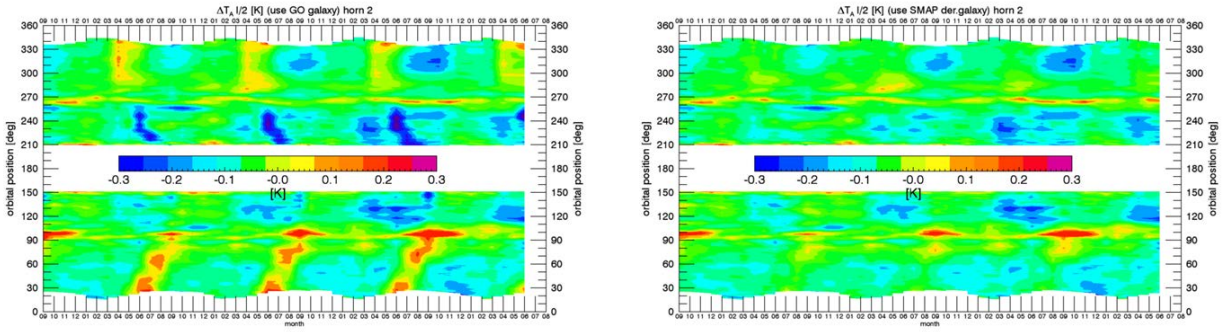

Figure 11: Measured minus expected TA for Aquarius horn 2. Left: GO calculation (Section 6.1). Right: GO calculation after the adjustments based on the SMAP fore – aft look. For the calculation of TA expected in this figure we have used HYCOM as reference SSS.

6.4 Empirical Symmetrization

Another important metric for the assessment of the accuracy of the galactic correction is the differences between ascending and descending swaths. The results are shown in Figure 12. The new model clearly reduces the difference between ascending and descending passes over the same ocean. However, some residual ascending – descending biases still remain even with the improved galaxy model. The remaining differences are removed empirically using a zonal symmetrization correction, which is described in this section.

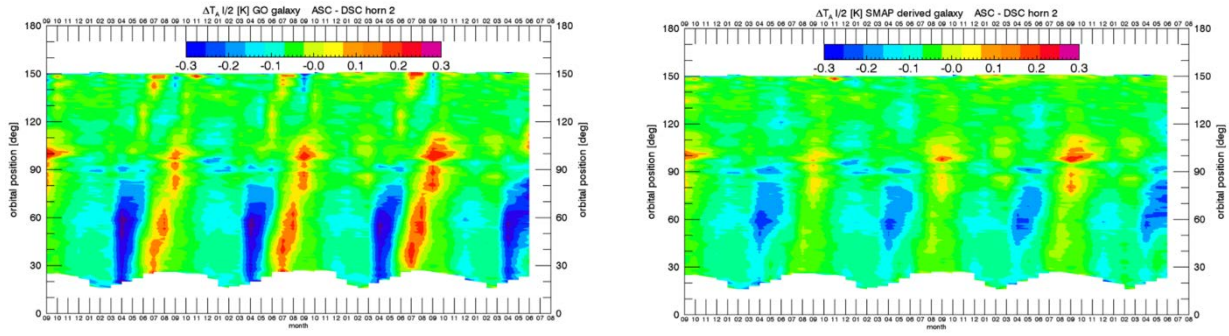

Figure 12: Left: The difference in ascending and descending orbits of the difference between measured and expected TA for Aquarius horn 2 using reflected galaxy from the GO model in Section 6.1. Right: The same double difference for Aquarius horn 2 using reflected galaxy from the updated reflected galaxy model based on the SMAP fore – aft results (Sections 6.2 and 6.3).

There are several possible reasons for the remaining inaccuracies:

1. The value of the variance of the slope distribution (74) is not completely correct, even after effectively increasing the roughness by adding 2 m/s to the wind speed based on the SMAP fore – aft results (Sections 6.2 and 6.3).
2. Errors in the antenna gain patterns used to derive the tables of the GO model (Section 2.2.2).
3. Other ocean roughness effects, which cause reflection of galactic radiation but cannot be modeled with an ensemble of tilted facets (e.g. Bragg scattering at short waves, breaking waves and/or foam, and net directional roughness features on a large scale).

4. The galactic tables themselves, which were derived from radio astronomy measurements (Le Vine and Abraham, 2004). For example, there is a small polarized component and Cassiopeia A is very strong and variable.

Such effects are very difficult or impossible to model. We have therefore decided to derive and use a purely empirical correction for the reflected galactic radiation, which is added to the GO calculation. The danger in doing this is that other geophysical issue (i.e. not associated with reflected radiation from the galaxy) could be masked. But, it was decided to accept this risk for V5.0.

This empirical correction is based on symmetrizing the ascending and the descending Aquarius swaths.

The basic assumptions are:

A. There are no zonal ascending – descending biases in ocean salinity on weekly or larger time scales.

B. The residual zonal ascending – descending biases that are observed are all due to the inadequacies (either over or under correction) in the GO model calculation for the reflected galactic radiation.

C. The size of the residual ascending – descending biases is proportional to the strength of the reflected galactic radiation.

Assumption A is based on current understanding of the structure of the salinity field for which there no known physical processes that would cause such a difference. Assumption B results from analyses of the salinity fields and known limitation of the GO model. Assumption C is based on theory for scattering from rough surfaces and the assumption that the source of any difference is reflected galactic radiation and the fact that the source and surface are independent. It is expected to hold in some mean sense over the footprint.

A symmetrization of the ascending and descending Aquarius swaths is done on the basis of a zonal average. According to Assumption C above the symmetrization weights will be determined by the strength of the reflected galactic radiation.

For the time being, only the 1st Stokes parameter $I = (T_{Bv} + T_{Bh})$ is considered which is the sum of the brightness temperatures at the ocean surface and will be denoted by T_B. In the equations below, $\langle \ldots \rangle$ denotes the zonal average and the variable z denotes the orbital angle (z-angle). If z lies in the ascending swath, then $-z$ (or $360^\circ - z$) lies in the descending swath and vice versa. $T_B(z)$ is first Stokes parameter as measured by Aquarius at the surface at z. $T_{A,gal,ref}(z)$ is the value of the reflected galactic radiation received by Aquarius as computed based on the SMAP fore – aft results (Section 6.3). The symmetrization term, $\Delta(z)$, which is the basis of the empirical correction, is given as:

$$\begin{aligned}
\Delta(z) &= \left[p \cdot \langle T_B(z) \rangle + q \cdot \langle T_B(-z) \rangle \right] - \langle T_B(z) \rangle \\
p &= \frac{\langle T_{A,gal,ref}(-z) \rangle}{\langle T_{A,gal,ref}(z) \rangle + \langle T_{A,gal,ref}(-z) \rangle} \\
q &= \frac{\langle T_{A,gal,ref}(z) \rangle}{\langle T_{A,gal,ref}(z) \rangle + \langle T_{A,gal,ref}(-z) \rangle}
\end{aligned} \tag{81}$$

The probabilistic channel weights p and q add up to 1: $p + q = 1$. The symmetrized surface T_B called T_B' is given by:

$$T_B'(z) \equiv T_B(z) + \Delta(z) \tag{82}$$

It is not difficult to see that this symmetrization has the following features:

1. Assume that z lies in the ascending swath and therefore $-z$ lies in the descending swath. If there is no reflected galactic radiation in the ascending swath, i.e. $\langle T_{A,gal.ref}(z) \rangle = 0$, then $p = 1$ and $q = 0$. That means that the symmetrization term and thus the whole empirical correction $\Delta(z)$ vanishes, and therefore: $T_B'(z) = T_B(z)$.

2. If, on the other hand, there is no reflected galactic radiation in the descending swath, i.e. $\langle T_{A,gal.ref}(-z) \rangle = 0$, then $p = 0$ and $q = 1$. That implies $\Delta(z) = \langle T_B(-z) \rangle - \langle T_B(z) \rangle$ and thus $\langle T_B'(z) \rangle = \langle T_B(-z) \rangle$.

3. The zonal average of $T_B{}'$ is symmetric: $\left\langle T_B{}'(z)\right\rangle = \left\langle T_B{}'(-z)\right\rangle$.

4. If the reflected galactic radiation is the same in ascending and descending swaths $\left\langle T_{A,gal.ref}(z)\right\rangle = \left\langle T_{A,gal.ref}(-z)\right\rangle$, then $p = q = \frac{1}{2}$ and thus the global average (sum of ascending and descending swaths) does not change after adding the symmetrization term: $\left\langle T_B{}'(z)\right\rangle + \left\langle T_B{}'(-z)\right\rangle = \left\langle T_B(z)\right\rangle + \left\langle T_B(-z)\right\rangle$.

5. If the zonal T_B averages are already symmetric $\left\langle T_B(z)\right\rangle = \left\langle T_B(-z)\right\rangle$, then the symmetrization term and thus the whole empirical correction $\Delta(z)$ vanishes, and therefore: $T_B{}'(z) = T_B(z)$. That means that we do not introduce any additional ascending – descending biases that were not already there.

An important feature of this symmetrization procedure is the fact that it is derived from Aquarius measurements only and does not rely on or need any auxiliary salinity reference fields such as ARGO or HYCOM.

The correction for the galaxy radiation (Section 2.2.2) is done at the TA rather the TB level. The symmetrization correction Δ for the 1st Stokes was derived at the TB level. It can be lifted to the TA level by dividing it by the spillover factor, which is the II component of the APC matrix (Section 3.3):

$$\Delta_{A,I}(z) \approx \frac{\Delta_I(z)}{A_{II}} \tag{83}$$

It is assumed that the galactic radiation itself is unpolarized and polarization occurs only through the reflection at the ocean surface. Ignoring Faraday rotation of the galactic radiation in the empirical correction term, its 2nd and 3rd Stokes component are:

$$\begin{aligned} \Delta_{A,Q} &\approx \frac{R_V - R_H}{R_V + R_H} \cdot \Delta_{A,I} \approx \frac{T_{A,gal,ref,Q}}{T_{A,gal,ref,I}} \cdot \Delta_{A,I} \\ \Delta_{A,U} &\approx 0 \end{aligned} \tag{84}$$

In (84) $R_{V,H}$ are the reflectivity for V and H polarization of an ideal (i.e. flat) surface. In the correction algorithm the reflected galactic radiation is subtracted from the measured $\mathbf{T}_A$ to get the contribution $\mathbf{T}_{A,Earth}$ that comes from the Earth only. This means that the full correction for the reflected galactic radiation in V5.0 is given by:

$$T_{A,gal,ref,P} = \tilde{T}_{A,gal,ref,P} - \Delta_{A,P} \quad P = I,Q,U \tag{85}$$

In (85) $\tilde{T}_{A,gal,ref,P}$ is the reflected galactic correction (79) based on the SMAP fore – aft results.

In the implementation of the empirical correction in the algorithm code, the term $\Delta_{A,P}$ is cast in form of a lookup table as it has been described in Section 2.2.2. The dimensions of the lookup table for $\Delta_{A,P}$ are (1441, 1441, 3,3), referring to time of the sidereal year, orbit position (z-angle), polarization (Stokes number) and radiometer (horn) number. We have not stratified the empirical correction $\Delta_{A,P}$ by wind speed and therefore the lookup table does not have a wind speed dimension. For the derivation of the lookup table we have used 3 years of Aquarius measurements from September 2011 – August 2014.

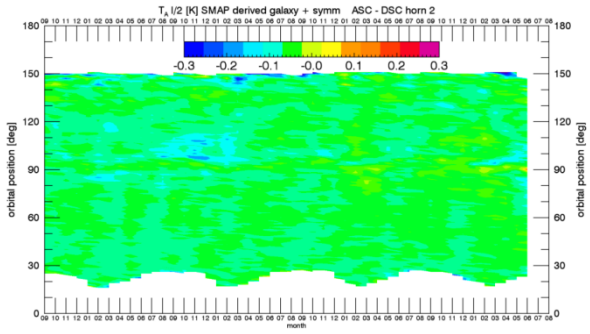

Figure 13: Same as Figure 12 but after applying the empirical symmetrization correction.

After applying the empirical symmetrization (85), the ascending – descending biases are basically eliminated (Figure 13).

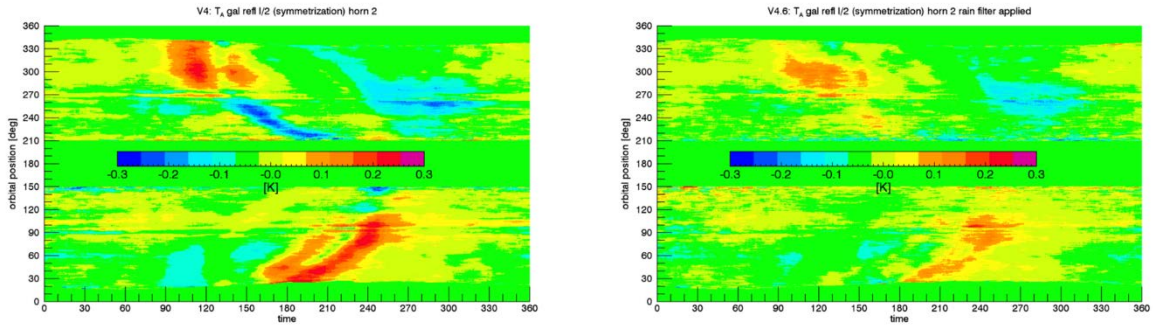

Figure 14: Empirically derived symmetrization correction $\Delta(z)$. Left: Based on the GO model (Section 6.1). Right: Based on the improved galactic model using the SMAP fore – aft results (Sections 6.2 and 6.3).

Figure 14 compares the size of the empirical symmetrization $\Delta(z)$ if it was derived from the GO calculation without implementing the SMAP fore -aft results (Section 6.1) with the one derived after adding the SMAP fore – aft results (Sections 6.2 and 6.3). It demonstrates that the improved galactic model that was derived from the SMAP fore – aft results reduces the need for the empirical symmetrization and cuts the size of this empirical correction roughly by about 50% (i.e. reduction in the red areas in the map at the left).

The Aquarius V5.0 Level 2 files contain both the values of the reflected galaxy TA from the GO calculation as given in Section 6.1, called rad_galact_Ta_ref_GO_X (X = V,H), and the final values that are used in the V5.0 algorithms after all the effective and empirical adjustments (SMAP fore – aft results and the empirical symmetrization, Sections 6.2 - 6.4), called rad_galact_Ta_ref_X (X = V,H).

7. Determination of Instrument and Calibration Parameters

7.1 Ocean Target Calibration

The Aquarius radiometer uses a reference load and noise diode injection as internal calibration targets (Piepmeier 2004, Piepmeier et al. 2005). The calibration is performed at each Level 2 report interval, which lasts 1.44 seconds. Unfortunately, the accuracy of the pre-launch values for the noise diode injection temperature T_{ND} was not sufficient for retrieving salinity. Moreover, immediately after launch it was evident that the value of T_{ND} was drifting (probably outgassing) and also other components of the instrument change over time. It is therefore necessary to have a stable and well-known calibration target over long time scales (weekly – monthly) for determining the value of T_{ND} and its time dependence. The global average of the ocean was adopted for this purpose. The calibration using the ocean is described in this section.

7.1.1 Basic Method

The ocean target calibration uses a 7-day (103 orbit) running TA average, denoted by $\langle \ldots \rangle_{OT}$ over the global ocean as calibration target. The goal of the calibration is to tune the calibration parameters, essentially gain and offset, so that for each Aquarius channel:

$$\left\langle T_{A,cal} - T_{A,\exp} \right\rangle_{OT} = 0 \tag{86}$$

$T_{A,cal}$ are the Aquarius TA measurements after the calibration adjustments are performed. $T_{A,\exp}$ are the expected TA and calculated as described in Section 3.8. The crucial input in its calculation is the reference salinity field, which is taken from Scripps ARGO (Section 4.8). That means essentially that the ocean target calibration forces the retrieved Aquarius salinity to the Scripps ARGO reference salinity on a global 7-day average. The average (86) is calculated for each orbit. The 7-day averaging window is chosen, because the Aquarius orbit repeat cycle is 7 days.

Note, that the calculation of $T_{A,\exp}$ for the ocean target calibration needs to use the HH-wind speed, which takes only observations from the Aquarius scatterometer as input. The HHH-wind speeds that are used for the salinity retrieval are not yet available at this stage as the calibrated radiometer TA does not yet exist. For details see Section 5.2.

It is crucial that both the measured and expected TA in the average $\langle \ldots \rangle_{OT}$ of the ocean target calibration, which determine the instrument calibration parameters, are of the highest possible quality and as much as possible free of errors. Therefore, a number of rigorous quality control checks are applied when calculating $\langle \ldots \rangle_{OT}$. Observations are excluded if one or more of the following conditions apply (Meissner 2014b; Le Vine and Meissner 2014):

1. The instrument pointing is degraded, indicated by the ACS mode variable in the Level 1 file.
2. The difference between RFI filtered antenna temperature (called T_F) and the unfiltered TA exceeds 0.3 K for either V-pol or H-pol, which indicates the presence of RFI and avoids the potential that the radiometer observation maybe contaminated by RFI.
3. The scatterometer observation is flagged for RFI.
4. The HH-wind speed algorithm (Section 5.2) did not converge.
5. The gain weighted land fraction g_{land} (Section 4.6) exceeds 0.001.
6. The gain weighted sea-ice fraction g_{ice} (Section 4.7) exceeds 0.001.
7. The reflected galactic radiation (average of V-pol and H-pol) exceeds 2.8 K.
8. The HH-wind speed is less than 3.0 m/s and the reflected galactic radiation (average of V-pol and H-pol) exceeds 1.8 K.
9. The reflected lunar radiation (average of V-pol and H-pol) exceeds 0.25 K.
10. The SST is colder than 5^{o}C.
11. The HH-wind speed exceeds 15 m/s.
12. The observation is in one of the areas that have been identified as being potentially contaminated by undetected RFI. This is based on unacceptably large observed salinity differences between ascending and descending swaths (Meissner 2014b).
13. The instantaneous rain rate IRR (Section 4.9) exceeds 0.25 mm/h. This rain filter is being applied to avoid mismatch between Aquarius and ARGO salinity due to possible salinity gradients in the upper ocean layer created by precipitation (Boutin et al., 2016). Aquarius measures surface salinity within the upper few centimeters of the ocean layer and in the case of a stratified

upper ocean layer and the presence of precipitation, the Aquarius SSS are fresher than those from ARGO, which measures at 5-meter depth.

7.1.2 Post-Launch Values for Noise Diodes

The initial post-launch values of the noise diode injection temperatures $T_{ND,0}$ obtained from (86) during the first week of operation are listed in Table 2:

Table 2: Values for the noise diode injection temperatures during the 1st week of operation of the Aquarius radiometer.

Channel	1V	1H	2V	2H	3V	3H
$T_{ND,0}$ [K]	638.09	667.77	656.54	687.25	705.80	679.92

7.1.3 Calibration Drift and Correction

The Aquarius calibration changes over time. Two major drift components have been identified and analyzed, which have different time scales and different origin.

The first one is a gain drift, most likely caused by out-gassing of the noise diodes. Its time scale is on the order of a couple months to 1 year. It is well modeled as an exponential time dependence of T_{ND}:

$$T_{ND}\left(n_{orbit}\right) = T_{ND,0}\cdot\left(1-c\right) \qquad c = A - B\cdot\exp\left(-D\cdot n_{orbit}\right) \tag{87}$$

The coefficients *A*, *B* and *D,* which specify the exponential fit, are determined once using the current history of measurements (all of them for V5.0). Then, the T_{ND} is adjusted for each orbit using this exponential fit as indicated in (86). The coefficient *c* is saved in the metadata of L2 files as delta_TND_V_coefficient and delta_TND_H_coefficient for each the 3 beams. The new value for TND is now used in the radiometer counts-to-TA conversion algorithm (Piepmeier et al. 2005). The orbit number n_{orbit} in (87) starts at launch (June 10, 2011) but (87) is applied starting when Aquarius was turned on (August 25, 2011), which corresponds to $n_{orbit} = 1110$.

The second type calibration drift manifests itself in pseudo-periodic oscillations in $T_{A,meas} - T_{A,\exp}$, which are superimposed on the exponential drift and occur on the time scales of weeks – months. The oscillations are termed "pseudo" because the calibration anomaly is not periodic in nature and only has a rough appearance of periodicity. One of the root cause for this oscillation was determined to be a locking issue in the backend Voltage to Frequency Converter (VFC), which impacts all counts of the radiometer including the reference load (Long Accumulation, or LA). A correction for the pseudo-periodic oscillations ("wiggles") has been developed and implemented that uses a hardware-based model that only requires inputs from the Aquarius radiometer and does not depend on the ocean or an external salinity reference field (Misra and Brown 2017). However, this correction scheme does not remove the "wiggles" completely and it is necessary to remove the residual to achieve the very high level of accuracy necessary for retrieving ocean salinity. An analysis of cold space maneuvers showed similar oscillations in several channels (Dinnat and Le Vine 2017). This indicates that these residual oscillations are not predominantly caused by the errors in the geophysical model used in the salinity retrievals but are likely an instrument issue whose root cause is currently not known. Therefore, it is warranted to remove them in the instrument calibration process. It was decided for the V5.0 L2 Aquarius science data to use the ocean target calibration to remove the residual wiggles and guarantee that (86) holds to a level of about 0.01 K. In order to remove the residuals, an offset correction is performed at each orbit to obtain the final calibrated TA:

$$T_{A,cal} = \tilde{T}_A - \left\langle \tilde{T}_A - T_{A.,\exp} \right\rangle_{OT} \tag{88}$$

Here, $\tilde{T}_A$ is the antenna temperature that is obtained *after* the exponential drift correction has been applied and the average is over 7 days. The values of the offsets are saved in the metadata of L2 files as radiometer_offset_correction for each of the radiometer channels. It is planned for future releases to explore if the 7-day (103 orbits) time average in the offset correction (88) can be relaxed to longer time scales.

7.1.4 Closure Between Sensor Calibration and Salinity Retrievals

Because the calibration is based on the difference between expected and measured TA one would expect that on a global basis, the two would be equal; and because the transformation of TA to brightness temperature at the surface is essentially the forward algorithm for expected TA used in reverse, one would expect the same to be true of the measured and expected TB at the surface. However, small inconsistencies exist between the calculation of the differences between measured and expected TA and the calculation of the differences between measured and expected $T_{Bsur,0}$ which result in small residuals. (The $T_{Bsur,0}$ is the TB at a flat ocean surface after the surface roughness correction.) In the calculation of TA expected the HH-wind speed needs to be used because calibrated Aquarius TB are not yet available at that stage of the algorithm. The surface roughness correction in the salinity retrieval algorithm uses HHH-wind speeds. The HHH and HH-wind speeds do not exactly match and thus sensor calibration and retrieval do not exactly match either. This results in small biases of about 0.003 K - 0.013 K between the measured and expected values of $T_{Bsur,0}$. The values of the biases are channel dependent. Other small biases of the same size between the measured and expected values of $T_{Bsur,0}$ are caused by the correction for land intrusion (Section 3.9). The correction is applied in the salinity retrieval algorithm when the antenna weighted land fraction exceeds 0.005. In the forward model calculation of TA expected this correction has not been applied at all.

As a consequence of the small biases between the measured and expected values of $T_{Bsur,0}$ there are also small biases in the retrieved Aquarius SSS when compared to ARGO. The SSS bias increases with decreasing SST. In V5.0 closure between calibration and retrieval is enforced by subtracting the observed small biases in $T_{B\,sur,0,meas} - T_{B\,sur,0,exp}$ from the measured $T_{B\,sur,0,meas}$ before the MLE of the salinity retrieval algorithm is performed (Section 3.7). The values of these biases are listed in Table 3. They are different for each channel and are constant in time. There was some debate about how to make this correction (e.g. to apply it to salinity) or even if it should be made at all. Its effect is small in any case.

Table 3: In V5.0 the values in this table are subtracted from *TB sur,0 measured* in order to enforce closure between sensor calibration and salinity retrievals.

Channel	1V	1H	2V	2H	3V	3H
Bias [K]	-0.013	-0.015	-0.021	-0.023	-0.020	-0.018

7.2 Post-Launch Adjustment of Antenna Patterns and Antenna Pattern Correction

The antenna patterns enter the salinity retrieval algorithm at many places. They are used to derive the corrections for the galactic, solar and lunar radiation (Section 2.2), the calculation of the APC coefficients (Section 3.3), and also in the derivation of the near-sidelobe correction for land contamination (Section 3.9).

7.2.1 GRASP 2012 Antenna Patterns

Aquarius V5.0 is mainly based on simulated antenna patterns that were created in 2012 from the GRASP (General Reflector Antenna Software Package) software (www.ticra.com/products/software/grasp) and provided by J. Vacchione from the *JPL Spacecraft Antennas Group*.

The APC matrix $\mathbf{A}_{\mathbf{ij}}^{\mathbf{GRASP,2012}}$ was computed following the method from Section 3.3 using the GRASP 2012 patterns. Its components in the Stokes vector (I, Q, U) basis (Piepmeier et al. 2008) are given in (89):

$$\mathbf{A}_{horn\,1}^{\mathbf{GRASP,2012}} = \begin{pmatrix} 1.04484 & -0.03827 & -0.00387 \\ -0.00297 & 1.07860 & 0.03089 \\ -0.00009 & -0.02582 & 1.07551 \end{pmatrix}$$

$$\mathbf{A}_{horn\,2}^{\mathbf{GRASP,2012}} = \begin{pmatrix} 1.04967 & -0.03432 & -0.00737 \\ -0.00063 & 1.05936 & -0.01558 \\ -0.00272 & 0.01112 & 1.05553 \end{pmatrix} \quad (89)$$

$$\mathbf{A}_{horn\,3}^{\mathbf{GRASP,2012}} = \begin{pmatrix} 1.05800 & -0.03435 & -0.01157 \\ -0.00036 & 1.04848 & 0.00708 \\ -0.00324 & -0.01480 & 1.04885 \end{pmatrix}$$

7.2.2 Empirical Adjustment of the APC Matrix Elements

Based on the analysis of Meissner (2014a) and Dinnat et al. (2015) it is warranted to adjust several elements of the APC matrix $\mathbf{A_{ij}}$ in (89). To discuss the issues, it is convenient to introduce the cross-polarization contamination χ_p and the spillover η_p for p = V, H -pol:

$$\chi_p \equiv \frac{\left[\mathbf{A^{-1}}\right]_{\mathbf{pq}}}{\left[\mathbf{A^{-1}}\right]_{\mathbf{pp}}} \qquad \eta_p \equiv 1-\left[\mathbf{A^{-1}}\right]_{\mathbf{pp}} \cdot \left(1+\chi_p\right) \quad p=V,H \quad q=H,V \tag{90}$$

The changes can be summarized as:

1. The GRASP 2012 antenna patterns overestimate the antenna backlobes, which receive radiation from the cosmic background $T_{B\cos}$. That results in an overestimate of the spillover η_p. As a consequence, the TB over hot radiometric scenes (e.g. land, sea-ice) that are obtained after applying the APC (44) become unrealistically large. For example, the V-pol and H-pol TB over the Amazon and Congo rain forests were found to be about 3 - 4 K larger than what is expected when comparing sensors that operate at higher frequencies (WindSat, AMSR, GMI , SSMIS) and when comparing with radiative transfer calculations. It was decided to reduce the spillover by about 0.015, or equivalently reduce the sizes of the diagonal matrix elements $\mathbf{A_{II}}$ and $\mathbf{A_{QQ}}$ by about 1.5% for all 3 horns. The spillover correction was also quantified using measurements of the cold sky during a transit of the spacecraft between ocean and land (Dinnat et al., 2015). This approach relies on the homogeneity of the sky scene in the main beam and the large TB gradient between land and ocean as seen by the backlobes. The uncertainty on land TB is mitigated as it is of second order compared to the TB difference between land and water.
2. The asymmetry in the spillover values η_p between V-pol and H-pol needed to be slightly increased for horn 2 and slightly decreased for horn 3. The purpose of that was to get realistic values for the difference between V-pol and H-pol $Q = T_{BV} - T_{BH}$ over the rain-forest sites. The expectation is that this difference is in the order of 2 – 3 K and that increases monotonously with increasing incidence angle.

3. The values for the cross-polarization contamination χ_p was left unchanged from the GRASP 2012 values.

4. The value for the 3rd Stokes diagonal element $\mathbf{A_{UU}}$ was left unchanged from the GRASP 2012 values. A good way to check $\mathbf{A_{UU}}$ are spacecraft pitch maneuvers. During those maneuvers there occurs a large dynamical change of the polarization basis alignment between spacecraft and Earth, which results in a dynamical large change in the value of the 3rd Stokes parameter. The change in the polarization basis alignment ϕ_{ant} can be computed from geometry based on the spacecraft attitude (Meissner and Wentz 2006; Meissner et al. 2012). It exceeds by far the polarization rotation due to Faraday Rotation in the Earth ionosphere ϕ_f (Section 3.4). We have found very good agreement between the measured and computed 3rd Stokes TB during the spacecraft pitch maneuvers (Figure 15).

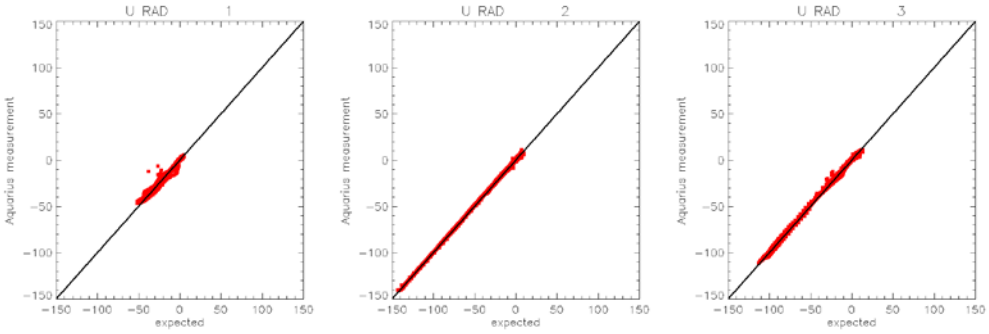

Figure 15: TOI measured versus expected 3rd Stokes during the pitch maneuvers. The outliers in horn 1 are due to land contamination.

5. The values of the couplings $\mathbf{A_{IU}}$ and $\mathbf{A_{QU}}$ from the 3rd Stokes parameter U into the 1st Stokes parameter I and the 2nd Stokes parameter Q were adjusted for horn 2 and horn 3. This was based on the observation of spurious crosstalk when stratifying the measured minus expected TOI TB for I and Q as function of U. Ideally, assuming that the Faraday rotation has been removed correctly, $T_{B,meas,I} - T_{B,\exp,I}$ and $T_{B,meas,Q} - T_{B,\exp,Q}$ should be flat when plotted as function of U. A slope indicates that the couplings $\mathbf{A_{IU}}$ and $\mathbf{A_{QU}}$ are incorrect. See for example Figure 16.

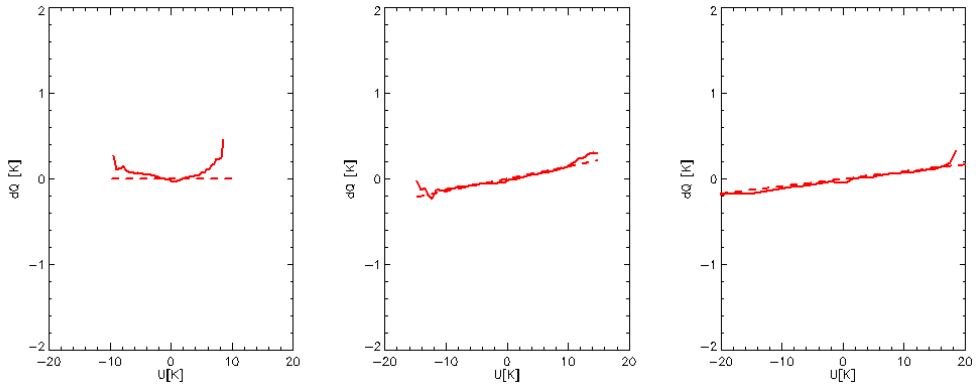

Figure 16: TOI *Q measured – expected* as function of *U* for the 3 Aquarius horns. In order to get the curves flat the values for $\mathbf{A}_{\mathbf{QU}}$ were slightly adjusted. The dashed lines indicate linear fits.

The adjusted APC matrix $\mathbf{A}_{\mathbf{ij}}^{\mathbf{V5}}$ that is used in the Aquarius V5.0 retrieval algorithm is given in (91) (in the I ,Q, U basis):

$$\mathbf{A}_{horn\,1}^{\mathbf{V5}} = \begin{pmatrix} 1.0300 & -0.0350 & 0.0500 \\ 0.0001 & 1.0641 & 0.0300 \\ 0.0000 & -0.0258 & 1.0755 \end{pmatrix}$$

$$\mathbf{A}_{horn\,2}^{\mathbf{V5}} = \begin{pmatrix} 1.0337 & -0.0304 & 0.0000 \\ 0.0027 & 1.0435 & -0.0144 \\ -0.0006 & 0.0211 & 1.0555 \end{pmatrix} \qquad (91)$$

$$\mathbf{A}_{horn\,3}^{\mathbf{V5}} = \begin{pmatrix} 1.0420 & -0.0326 & 0.0250 \\ 0.0011 & 1.0328 & 0.0215 \\ 0.0000 & -0.0148 & 1.0489 \end{pmatrix}$$

Table 4 lists the TOI TB over the Amazon rain forest calibration site using the V5.0 APC coefficients.

Table 4: TB TOI over the Amazon rain forest site. The location is [52W-59W] and [1S-3N]. We have only used observations from the descending (morning) swath as its TB are less affected by diurnal effects.

TB TOI [K]	horn 1	horn 2	horn 3
I/2 = (V+H)/2	279.7	279.6	277.3
Q = V-H	2.0	2.5	3.4

7.2.3 Hybrid Antenna Patterns

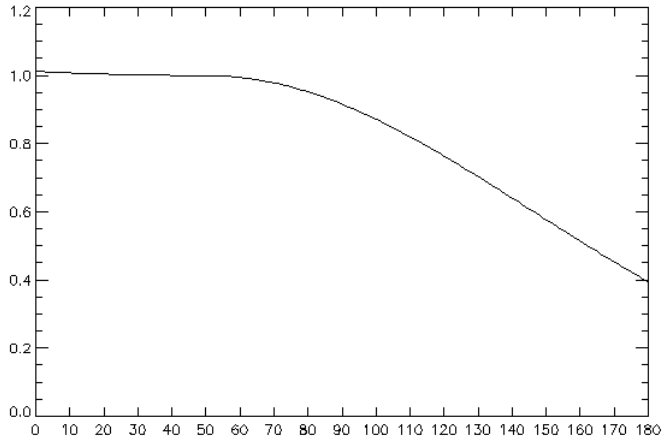

Figure 17: Scaling of the antenna gain as function of the polar angle θ (x-axis, in deg) that is used in the construction of the hybrid antenna patterns.

Hybrid antenna patterns have been constructed for all 6 Aquarius channels. The goal is to create antenna patterns that are consistent with the empirically adjusted APC coefficients for V-pol and H-pol as explained in Section 7.2.2). The hybrid antenna patterns are designed to have the same cross-polarization values χ_p as in the GRASP June 2012 model patterns but spillover values η_p that match closely the spillover values of the patterns (91) that are used Aquarius V5.0. These spillover values are about 0.015 smaller than the GRASP 2012 spillover values.

Table 5: Values for the constants α and β in the AP scaling (92) for each Aquarius channel.

Channel	α	β
1V	0.500E-5	5.500E-5
1H	0.800E-5	8.200E-5
2V	0.480E-5	6.000E-5
2H	0.820E-5	11.500E-5
3V	0.430E-5	6.300E-5
3H	0.670E-5	9.300E-5

In order to construct these patterns a scaling procedure has been developed that transfers power from the antenna backlobes into the main lobe and near-sidelobes (Figure 17). The scaling de-

pends on the polar angle θ (zero at antenna boresight). The value for the transition angle where the value of the scaling function is 1.0 was set to $\theta_c=50^o$, which is consistent with a similar analysis that was performed by Dinnat et al. (2015) using observation of the cold sky.

The form of our scaling function is:

$$s(\theta)=\begin{cases}\exp\left[+\alpha\cdot(\theta-\theta_c)^2\right], & \theta\le\theta_c\\ \exp\left[-\beta\cdot(\theta-\theta_c)^2\right], & \theta>\theta_c\end{cases} \tag{92}$$

The value of the polar angle θ is in degrees. The values for the constants α and β for each channel are listed in Table 5.

In the V5.0 processing the hybrid antenna patterns are used for deriving the antenna gain weighted fractions for land g_{land} (Section 4.6) and sea ice g_{ice} (Section 4.7) as well as the correction tables for land intrusion (Section 3.9) and the direct (Section 2.2.3) and reflected (Section 2.2.4) solar intrusions. This improves the consistency between these parameters and the APC matrix. The corrections for the direct (Section 2.2.1) and reflected (2.2.2) galactic radiation in V5.0 use the GRASP 2012 antenna patterns and not the hybrid antenna patterns.

7.3 Non-Linear IU- Coupling

Prior Aquarius data releases have exhibited a spurious coupling from the 3rd Stokes parameter U into the 1st Stokes parameter *I*, which results in an error in the retrieved salinity that is correlated with the value of the 3rd Stokes parameter U. These observed biases have also been observed and reported by the University of Hawaii group (Hacker et al. 2014) within an EOF (empirical orthogonal functions) analysis of the spatial and temporal patterns of SSS Aquarius – ARGO.

The full lines in Figure 18 shows the observed biases in TB measured – expected of the $I/2 = (T_{BV}+T_{BH})/2$ at the TOI as function of the 3rd Stokes TA for the 3 Aquarius horns. For a given value of the 3rd Stokes TA the bias increases with decreasing incidence angle. That means it is smallest for the outer horn and largest for the inner horn.

The bias curves in Figure 18 are non-linear. It is currently not understood what the root cause of the observed bias is, and it is also not clear if it is caused by the instrument or some deficiency in

the algorithm that transforms the measured antenna temperatures into the TOI TB. If the coupling from 3rd Stokes U_A into the 1st Stokes I was linear, as it is the case for the coupling of U into the 2nd Stokes Q, could be explained by an inaccuracy of the APC coefficients and thus be absorbed into and adjustment of the APC matrix (Meissner 2014a). This is not the case for a non-linear behavior of the IU coupling as is shown in Figure 18.

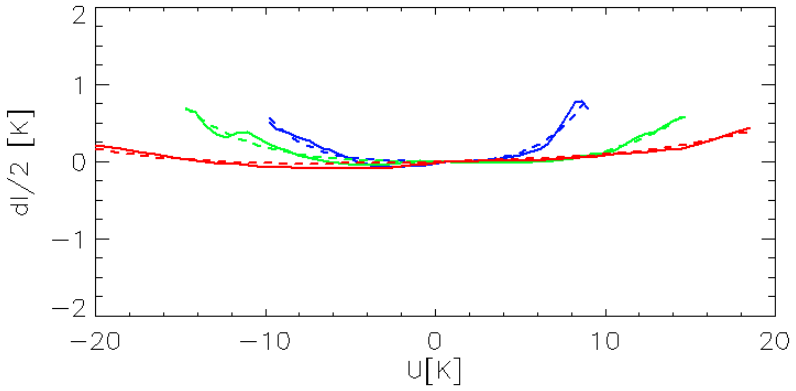

Figure 18: TB measured – expected for I/2 = (V+H)/2 as function of antenna temperature 3rd Stokes U_A for the three Aquarius horns. Blue = horn 1, green = horn 2, red = horn 3. Full lines = observations, dashed lines = 4th polynomial fits.

For the V5.0 processing an empirical correction was implemented in order to account for the observed spurious biases. We have fitted 4th order polynomials (dashed curves in Figure 18) to the observed bias curves (full lines in Figure 18):

$$\frac{\Delta I\left(U_A\right)}{2} = \sum_{k=1}^{4} \zeta_k \cdot U_A^k \tag{93}$$

Table 6: Numerical Values for the Coefficients $\zeta_k, k = 1,\ldots 4$ in equation (93) for the three Aquarius horns.

k	1	2	3	4
horn 1	-1.58755100e-003	1.71341502e-003	3.18569692e-004	7.46477289e-005
horn 2	-2.35805891e-003	4.11458555e-004	-1.00910563e-006	1.22936368e-005
horn 3	5.25833641e-003	2.56355465e-004	6.95031563e-006	1.47258597e-006

In the V5.0 processing the computed value of $\Delta I\left(U_A\right)$ from equation (93) gets subtracted after the APC from the 1st Stokes at the TOI I_{TOI}. The numerical values for the polynomial coefficients ζ_k, $k=1,\ldots 4$ are listed in Table 6 .

8. Uncertainty Estimates

Each Level 2 and Level 3 Aquarius salinity retrieval is associated with a formal uncertainty value. In this section we present a method for formally assessing random and systematic uncertainties in the Aquarius salinity retrievals. The method is based on performing multiple retrievals by perturbing the various inputs to the retrieval algorithm and calculating the sensitivity of the Aquarius salinity to these inputs. Together with an error model for the uncertainties in the input parameters it is possible to calculate the uncertainty in the retrieved SSS. It is important to distinguish between random uncertainties, which get suppressed when computing weekly or monthly averages and systematic uncertainties, which do not get suppressed by taking averages.

8.1 Formal Assessment of Uncertainties

The basic approach to formally assess an uncertainty of the Aquarius salinity retrieval $S(x_i,\ldots)$ to a parameter x_i is to calculate the sensitivity of S to x_i. This is done by running the standard Aquarius Level 2 algorithm after perturbing the input x_{i0} by a small amount $\pm\Delta x_i$. The sensitivity is then computed as the change:

$$\frac{\partial S}{\partial x_i}(x_{i0}) \approx \frac{S(x_{i0}+\Delta x_i)-S(x_{i0}-\Delta x_i)}{2\cdot\Delta x_i} \tag{94}$$

In the limit of small Δx_i, this is a derivative and assuming that we have an uncertainty estimate $\Delta x_i(x_{i0})$ for the parameter, x_i, then the corresponding uncertainty in S is given by:

$$\Delta S_i(x_{i0}) \approx \frac{\partial S}{\partial x_i}\cdot\Delta x_i \tag{95}$$

The assessment of the uncertainty in S consists therefore in two parts:

1. The computational/algorithm part, i.e. running each retrieval algorithm with the perturbed parameter values.
2. Obtaining a realistic error model for all the uncertainties that are involved. This part is done offline and its results are fed into the perturbed retrievals.

When running the algorithm for a perturbed variable, all the other variables are left unperturbed. Performing the uncertainty estimation this way takes into account that a given uncertainty in one of the input parameter can translate to very different uncertainties in the retrieved salinity depending on the environmental scene. For example, the same error in the input wind speed that is used in the surface roughness correction or in the reflected galactic radiation will result in a much larger uncertainty in salinity in cold water where the sensitivity of the T_B to salinity is low than it would in warm water where the sensitivity is higher. The SST of the scene is a major driver in the size of the salinity uncertainty.

8.2 Propagation of Uncertainties

8.2.1 Random and Systematic Uncertainties

We need to assign uncertainties to both the Level 2 (L2) and to the Level 3 (L3) Aquarius salinity products. The propagation of the uncertainties from the 1.44 sec measurements (L2) to the L3 averages is not straightforward, as the uncertainties have both random and systematic components. Whereas the random components are getting suppressed by a factor $1/\sqrt{N}$ when averaging over N samples, the systematic components do not but the uncertainty of the average remains simply the average of the individual uncertainties. As a consequence, it is necessary to separately assess a random uncertainty Δx_i^{ran} and a systematic uncertainty Δx_i^{sys} for each parameter x_i. This separation is also not straightforward and not unambiguous. As a general guideline:

1. Uncertainties that fluctuate on larger time and spatial scales (1 month, > 100 km) are treated as systematic uncertainties.
2. Uncertainties that fluctuate on shorter time and length scales are treated as random uncertainties.

Every L2 salinity retrieval and every L3 map cell will contain two uncertainty values: a random uncertainty ΔS^{ran} and a systematic uncertainty ΔS^{sys}. The total RMS uncertainty is given by:

$$\Delta S = \sqrt{\left(\Delta S^{sys}\right)^2 + \left(\Delta S^{ran}\right)^2} \tag{96}$$

In the following we address the error propagation of both random and systematic uncertainties for the L2 retrievals and the creation of the L3 maps.

8.2.2 Uncertainty Propagation within the L2 Algorithm

The retrieved salinity $S(x_i)$ depends on a number of parameters $x_i, i = 1,\ldots M$, which all have separate uncertainties $\Delta x_i, i = 1,\ldots M$. Our error model will assume that all of these uncertainties are mutually independent. However, the retrieval algorithm and the geophysical model function can introduce correlations between the different horns and polarizations. For example, radiometer noise (NEDT) is uncorrelated in all channels, whereas an uncertainty in SST or the in the reflected galaxy results in certain correlations among the different channels (V-pol and H-pol). The following prescriptions are used for uncertainty propagation:

1. Random uncertainties add in the root mean square (RMS) sense:

$$\Delta S^{ran}(\mathbf{x_0}) = \sqrt{\sum_{i=1}^{M}\left[\frac{\partial S}{\partial x_i}(\mathbf{x_0})\cdot \Delta x_i^{ran}(\mathbf{x_0})\right]^2} \tag{97}$$

The vector $\mathbf{x_0}$ stands for the set of unperturbed parameters $x_{i0}, i = 1,\ldots M$.

2. The conservative method for the propagation of systematic errors would be to add them in an absolute sense:

$$\Delta S^{sys}(\mathbf{x_0}) = \sum_{i=1}^{M}\left|\frac{\partial S}{\partial x_i}(\mathbf{x_0})\cdot \Delta x_i^{sys}(\mathbf{x_0})\right| \tag{98}$$

Frequently, the RMS addition (97) is also used for the propagation of systematic errors. This is based on the assumption that the various systematic errors have different signs and thus cancellation can occur in a similar way as for random errors. For the Aquarius L2 error propagation we have adopted the RMS addition (97) when computing systematic errors.

8.2.3 Uncertainty Propagation in L3 Averaging

Assuming we have $j = 1,\ldots N$ L2 salinity retrievals S_j at a certain cell with individual random errors, ΔS_j^{ran}, individual systematic errors, ΔS_j^{sys}, and individual total RMS error

$\Delta S_j = \sqrt{\left(\Delta S_j^{sys}\right)^2 + \left(\Delta S_j^{ran}\right)^2}$. The starting point for the Aquarius L3 product is a binned product (there is also a smoothed product) which in general can be formed as weighted average:

$$\overline{S} = \frac{\sum_{j=1}^{N}\left[w_j \cdot S_j\right]}{\sum_{j=1}^{N} w_j} \tag{99}$$

with weights $w_j, j = 1,\ldots N$. For the computation of the uncertainty of the L3 product, we have adopted the binned format with standard weighting, which is to set $w_j = 1$ for all j, which is adopted in Aquarius V5.0.

The following rules apply for calculating the systematic error ΔS^{sys} and the random error ΔS^{ran} of the L3 product in V5.0 in the case of equal weighting $w_j, j = 1,\ldots N$:

The systematic uncertainty of the L3 product is computed as:

$$\Delta\overline{S}^{sys} = \frac{1}{N} \cdot \sum_{j=1}^{N}\left[\left|\Delta S_j^{sys}\right|\right] \tag{100}.$$

This means that when going from L2 to L3 we apply the conservative method (98) for propagation of systematic errors and do not allow error cancellation.

The random uncertainty (standard deviation) of the L3 average is computed as:

$$\Delta\overline{S}^{ran} = \frac{\Delta S^{ran}}{\sqrt{N}} \tag{101}$$

8.3 Error Modeling

This section discusses the major error sources of the Aquarius salinity retrieval algorithm and the quantitative assessment of their uncertainty.

8.3.1 NEDT

The radiometer noise (NEDT) is approximately the standard deviation of the noise in each 10 ms sample. The effective noise for salinity retrieval is the noise in the basic 1.44 sec Aquarius data block used in processing. This effective noise (NEDT) is computed as the standard deviation of the RFI filtered antenna temperatures (TF) in each 1.44 second cycle divided by the square root of the number of short accumulations within that cycle used in the computation of TF (i.e. assuming all samples are independent). This error (effective NEDT) is treated as random. We compute the effective NEDT and the resulting error in the salinity for all 3 channels: V-pol, H-pol and the 3rd Stokes parameter. It is assumed that these 3 components are independent and that the resulting errors in the salinity can be added as root sum squares.

8.3.2 Sensor Pointing Errors

In order to estimate the magnitude of the sensor pointing knowledge error we compute the Earth Incidence Angle difference between nominal pointing (i.e. assuming that the S/C z-axis is pointing to nadir) and the actual pointing that is computed from the measured S/C attitude. This value is the combination of both pointing knowledge and control errors and it thus can be regarded as an upper limit for the pointing knowledge error (F. Patt, personal communication, 2015). This error is treated as random. It turns out that its size and contribution to the total uncertainty in retrieved salinity is less than 0.01 psu and thus neglected.

8.3.3 Errors in Surface Wind Speed and Direction

The estimated random component (dashed red line in Figure 19) is based on running perturbed Aquarius HHH wind speed retrievals (Meissner et al. 2014). The major error sources are the noise in the L2 radiometer (NEDT) and scatterometer (Kp-value) observations and errors in the auxiliary NCEP wind speed that is used as background field.

The full red line in Figure 19 depicts the standard deviation of the wind speed difference between the Aquarius HHH wind speed and collocated WindSat wind speed (Meissner et al. 2014) after dividing by $\sqrt{2}$. The division by $\sqrt{2}$ accounts for the fact that part (about half) of the observed random difference comes from errors in the Aquarius wind speeds and the other part comes from er-

rors in the WindSat wind speed. This assumption is supported by a triple point analysis of Aquarius, WindSat and buoy wind speeds (Meissner et al. 2014). We have checked that using the full red line as error model for the random component in the uncertainty analysis would indeed result in uncertainty estimates for the Aquarius salinities that are too large when comparing with ground truth observations. This applies in particular at high wind speeds. The dashed line from Figure 19, which is the formal error estimate for the Aquarius HHH wind speed, results in a more realistic uncertainty estimate for the retrieved Aquarius salinity. This indicates that the random error in the Aquarius HHH wind speed estimated from the ground truth comparison (full red line in Figure 19) might be too large, in particular at high winds despite dividing the standard deviation of the difference between Aquarius and WindSat by $\sqrt{2}$. A possible explanation is that sampling mismatch between Aquarius and WindSat observation might also contribute to the observed value of the standard deviation. This sampling mismatch error is expected to increase with wind speed.

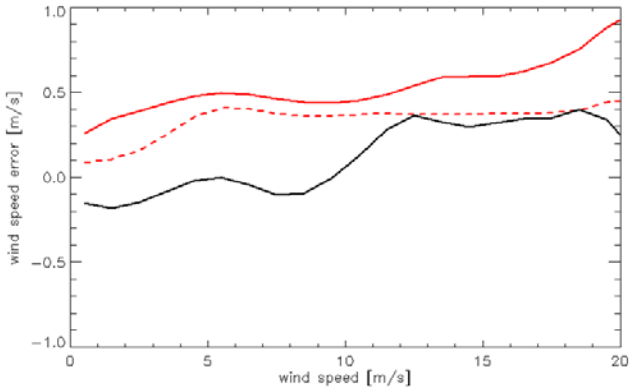

Figure 19: Estimated error of surface wind speed that is used in the Aquarius SSS retrieval: Dashed red line: Estimated random error from perturbed HHH wind speed retrieval. This curve is used as error model in the uncertainty estimation of the SSS retrievals. Full red line: random difference between Aquarius HHH and WindSat wind speed divided by $\sqrt{2}$. Black line: Estimated systematic error from Aquarius HHH – WindSat comparison.

The estimate of the systematic component of this error is based on computing the bias between Aquarius HHH and WindSat wind speeds as a function of wind speed (black line in Figure 19). As was the case for the random error in the Aquarius HHH wind speed, it can also be assumed that part of the observed systematic error is due to the WindSat wind speed. One should regard the systematic uncertainty in the Aquarius HHH wind speed obtained from the full black curve in Figure 19 as an upper limit.

For the error in the auxiliary NCEP wind direction field we assume 10° and treat it as random error.

8.3.4 Errors in Ancillary SST Input

The estimated uncertainty in the auxiliary SST is treated as systematic. To obtain a typical value for the SST uncertainty, we compared, at each Aquarius L2 observation, the NOAA OI (Optimum Interpolated) SST (that had been used in the Aquarius SSS retrievals up to Version 4.0; It was decided, given the similarity with the CMC product, to not repeat the computation) with weekly SST averages from WindSat.

Figure 20 shows the monthly difference between Reynolds and WindSat SST.

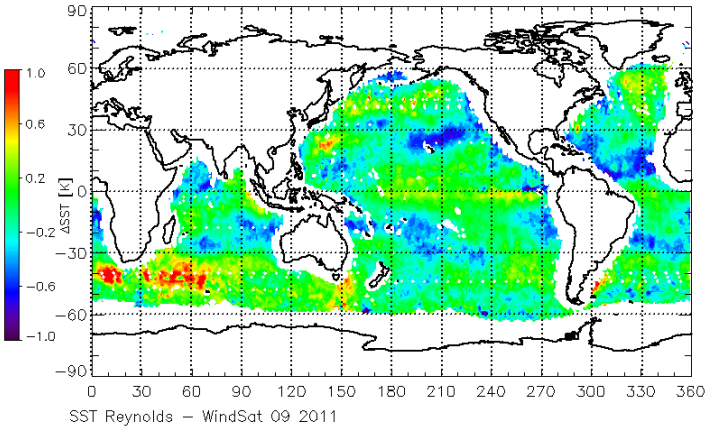

Figure 20: Monthly average of SST difference between SST from Reynolds and WindSat for September 2011.

8.3.5 Errors Due to Non-Linear IU-Coupling

Aquarius V5 applies an empirical correction for the observed non-linear IU coupling (Section 7.3). We have included the size of the coupling (i.e. the change in the first Stokes parameter, I) as a systematic error in the uncertainty estimate.

8.3.6 Errors in Reflected Galactic and Lunar Radiation

The estimated uncertainty in the correction for the reflected galactic radiation are treated as systematic and based on the bias of $T_{Ameas} - T_{Aexp}$ as a function of $T_{A,gal,ref}/2$ and Aquarius wind speed (Figure 21), where it is assumed $T_{Ameas} - T_{Aexp}$ characterizes the degradation of the salinity retriev-

als. For the purpose of uncertainty estimation we are using the HYOCM SSS as reference salinity. The uncertainty for the reflected lunar radiation is based on stratifying $T_{Ameas} - T_{Aexp}$ versus $T_{A,moon,ref}$ (Figure 22).

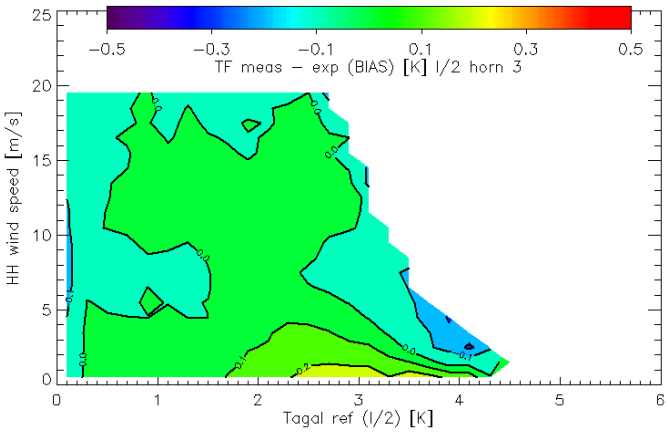

Figure 21: Bias of $T_{Ameas} - T_{Aexp}$ stratified as function of reflected galactic radiation and Aquarius HH wind speed.

In the uncertainty estimate we use Figure 21 and Figure 22 as lookup tables in order to estimate the systematic uncertainties $\Delta T_{AI,gal,ref}/2 = (\Delta T_{AV,gal,ref} + \Delta T_{AH,gal,ref})/2$, i.e. the average of V-pol and H-pol TA. Figure 21 and Figure 22 depict the values for the biases of the differences $T_{Ameas} - T_{Aexp}$ as function of the reflected galaxy and lunar radiation. The corresponding plots for the standard deviations give small values compared with the bias values. We therefore use only the biases for the uncertainty estimates.

It is assumed that the galactic radiation itself is unpolarized and polarization occurs only through the reflection at the ocean surface. The uncertainty in the 2nd Stokes parameter $\Delta T_{AQ,gal,ref} = \Delta T_{AV,gal,ref} - \Delta T_{AH,gal,ref}$ associated with the reflected galactic radiation can then be approximately calculated based on the reflectivity ratio:

$$\Delta T_{AQ,gal,ref} \approx \frac{R_V - R_H}{R_V + R_H} \cdot \Delta T_{AI,gal,ref} \approx \frac{T_{AQ,gal,ref}}{T_{AI,gal,ref}} \cdot \Delta T_{AI,gal,ref} \qquad (102)$$

That means that the uncertainties in the 1st and the 2nd Stokes parameters associated with the reflected galactic radiation are correlated. As a consequence, the uncertainties in the V-pol and H-pol TA of the reflected galaxy are correlated as well. We set the uncertainty in the 3rd Stokes of the galactic radiation to zero. The same rules apply when estimating the uncertainty in the reflected

lunar radiation. When performing the perturbed retrievals, it is important to treat these channel correlations properly. That means in the case for the reflected galaxy that the when running the perturbed salinity retrieval algorithm, both V-pol and H-pol are perturbed at the same time.

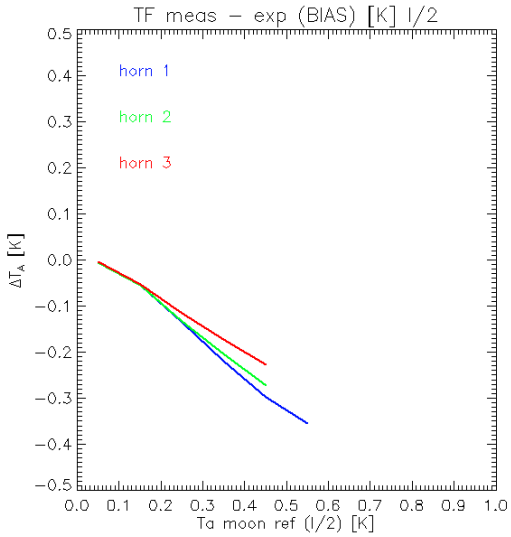

Figure 22: Bias of $T_{Ameas} - T_{Aexp}$ stratified as function of reflected moon radiation.

8.3.7 Intruding Radiation from Land and Sea Ice

The estimated uncertainty due to intrusion of radiation from land and sea ice surfaces into the sidelobes of the Aquarius antenna is treated as systematic and its estimation is based on the RMS of $T_{Bmeas} - T_{Bexp}$ as a function of the gain-weighted fractions of land g_{land} and sea ice g_{ice} (Figure 23). The RMS of $T_{Bmeas} - T_{Bexp}$ is the root sum square of bias and standard deviation and both of them give a significant contribution to the whole RMS. As was the case for the reflected galaxy and lunar radiation, our uncertainty estimates for the intrusions from land and sea ice are based on studying the degradation of the retrieval algorithm by comparing with reference observations, which are again HYCOM SSS. When computing the variance $\sigma^2(T_{Bmeas} - T_{Bexp})$ as function of g_{land} and g_{ice} we have subtracted the *noise floor*, which is the value for $\sigma^2(T_{Bmeas} - T_{Bexp})$ over the open ocean. i.e. if g_{land} and g_{ice} are close to 0, because we consider only the uncertainty in $T_{Bmeas} - T_{Bexp}$ that arises from the degradation due to intruding radiation from land and sea ice surfaces. Curves as shown in Figure 23 are produced for all three horns and for both V-pol and H-pol T_{Bmeas}

– T_{Bexp}. When running the perturbed retrievals, we look up the values for $T_{Bmeas} - T_{Bexp}$ in all of the channels based on the actual values of g_{land} and g_{ice}. As it was the case in section 8.3.6, this results in correlated uncertainties for V-pol and H-pol T_B for each horn.

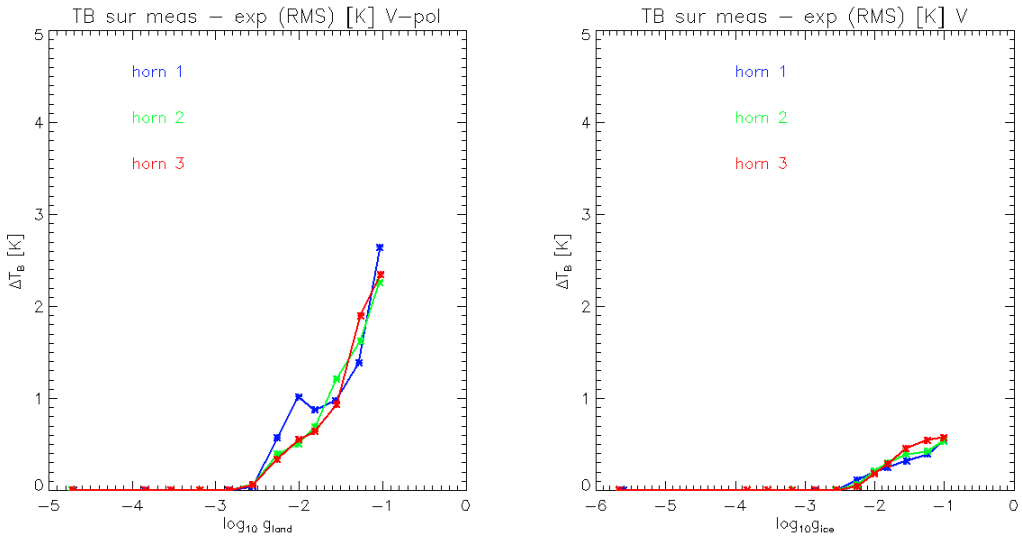

Figure 23: RMS of $T_{Bmeas} - T_{Bexp}$ for the V-pol stratified as function of the gain weighted land fraction g_{land} (left) and gain weighted sea ice fraction g_{ice} (right).

8.3.8 Undetected RFI

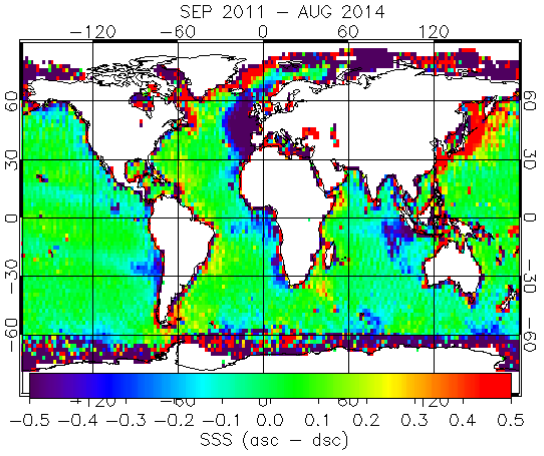

Figure 24: Map of the salinity difference between ascending and descending Aquarius swaths for SEP 2011 – AUG 2014.

The uncertainty from undetected RFI can be estimated from the SSS differences between ascending and descending Aquarius swaths. It is treated as systematic uncertainty. For the formal uncertainty estimate we first create a static 3-year map of the difference between ascending (PM) and descending (AM) Aquarius SSS summing over all three horns (Figure 24). The next step is to create a mask of areas where undetected RFI is likely present. This can be done by creating peak hold maps of RFI filtered – unfiltered TA separately for ascending and descending swaths, mask cells where this difference exceeds a threshold (0.2 K) and then extend this mask by a certain amount (+/- 4°) in order to account for the fact that the undetected RFI can also affect adjacent footprints.

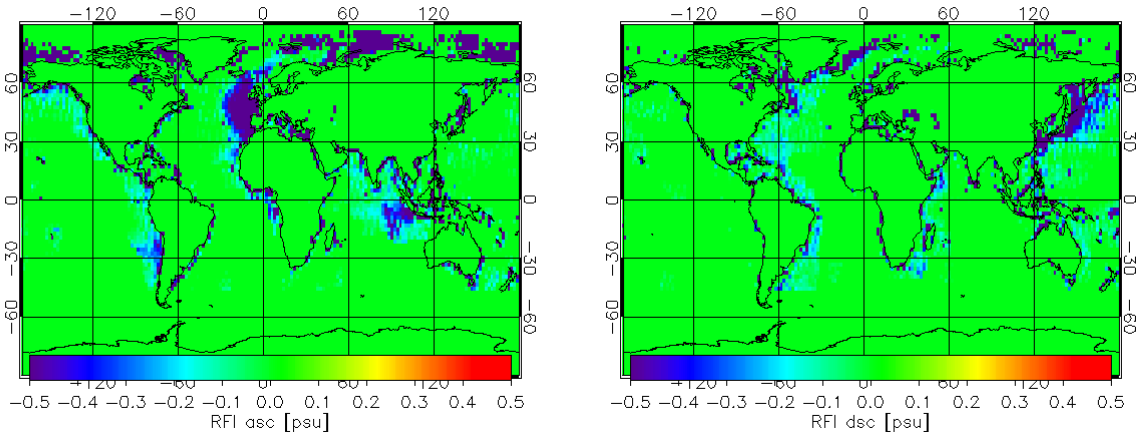

Figure 25: Estimated uncertainty in the retrieved Aquarius salinity due to undetected RFI for the ascending swath (left) and the descending swath (right) after averaging over all 3 horns.

The final step is to look for the overlap in these maps. Because undetected RFI always results in a low salinity value, we create maps for the ascending swaths where $SSS_{asc} - SSS_{dsc} < 0$ and for the descending swaths where if $SSS_{asc} - SSS_{dsc} > 0$ and look for the overlap with the RFI masks from the previous step. This results in the two maps of Figure 25 which show the uncertainty (difference in SSS). Unlike all other uncertainties, the uncertainty estimate due to RFI is done directly on the salinity level. The uncertainty maps are static, i.e. we assume the same values for the whole Aquarius mission and we are averaging over all three horns, i.e. the uncertainties are not horn specific.

8.3.9 Uncertainties that are Not Considered or Neglected

The V5.0 error calculation does not address the uncertainties listed in Table 7, because they are either estimated to be negligible or because it is not possible to make a realistic assessment of their sizes.

Table 7: Error sources that are not considered or neglected in the uncertainty estimate.

Error Source	Reason for not considering
Atmospheric temperature	Estimated to be small. The estimated sensitivity of the retrieved salinity to the average value of the atmospheric temperature is less than 0.05 psu/K. Assuming similar uncertainties in the values of the ancillary atmospheric temperatures as the ones in the ancillary SST (Figure 20) will result in small or negligible errors in the retrieved salinity.
Atmospheric vapor	Very small signal and therefore very small uncertainty.
Atmospheric liquid cloud water	Difficult to estimate as long as ancillary NCEP liquid cloud water profiles are used in the retrieval algorithm. When comparing with cloud water values from microwave radiometer (SSMIS, WindSat) or CMORPH, the cloud water values from NCEP are statistically compatible with zero. Calculating the cloud water absorption from the ancillary NCEP liquid cloud water profile is merely a placeholder in the V5.0 algorithm. It is planned in the future to use a realistic ancillary field (e.g. CMORPH) for computing the liquid cloud water absorption.
Solar intrusion (direct, reflected, backscattered)	Very small signal and therefore very small uncertainty.
Direct galaxy + cold space	Difficult to estimate.
Instrument calibration	We assume perfect ocean target calibration, i.e. and absolute calibration of the Aquarius TA to the GMF as explained in Section 7.1. We assume that all residual biases have been corrected in the updated GMF and that the dielectric and atmospheric absorption models have no error.
APC coefficients	
GMF for specular surface and wind emission and atmospheric absorption	

8.4 Error Allocations at L2 and L3

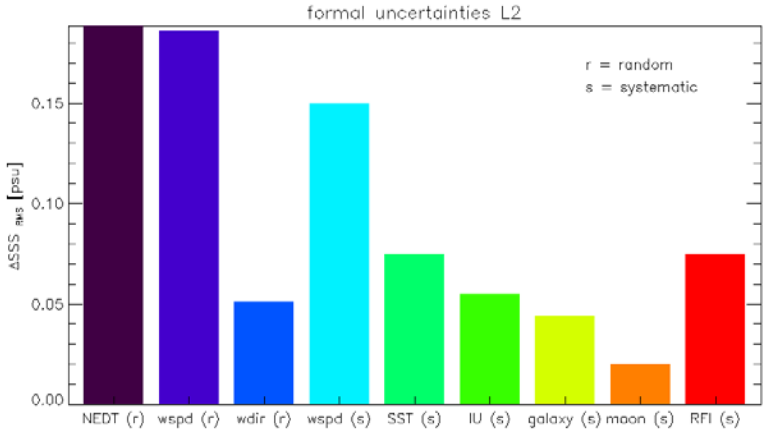

Figure 26: Contribution of the various uncertainties to the total estimated uncertainty for the Aquarius L2 salinity that is observed at the 1.44 sec cycle for open ocean scenes.

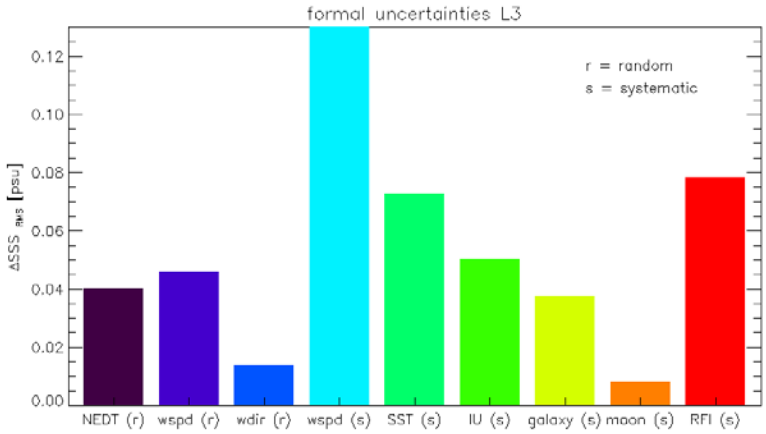

Figure 27: Contribution of the various uncertainties to the total estimated uncertainty for the monthly 1° Aquarius L3 salinity maps for open ocean scenes.

Figure 26 and Figure 27 show the contributions of the various components of the error model (Section 8.3) to the total formal uncertainty estimate for the Aquarius L2 product (1.44 sec) and the monthly 1° L3 salinity products respectively. The dominant contributions at the 1.44 sec are the NEDT and the random and systematic uncertainties in the wind speed that is used in the surface roughness correction algorithm. At the monthly 1° Level 3 product all the random uncertainties including the NEDT get reduced to low levels.

9. Acronyms and Abbreviations

In the following we list some frequently used acronyms and abbreviations.

AMSR	Advanced Microwave Scanning Radiometer
APC	Antenna Pattern Correction
asc	ascending swath
ATBD	Algorithm Theoretical Bases Document
Cal/Val	Calibration and Validation
CMB	Cosmic Microwave Background
CMC	Canadian Meteorological Center
CMORPH	Climate Prediction Center Morphing
dsc	descending swath
EIA	Earth Incidence Angle
GDAS	General Data Assimilation System
g_{ice}	sea-ice fraction (weighted by antenna gain)
g_{land}	land fraction (weighted by antenna gain)
GMF	Geophysical Model Function
GMI	Global Precipitation Mission Microwave Imager
GO	Geometric Optics
GRASP	General Reflector Antenna Software Package
HH-wind	Aquarius wind speed retrieved from scatterometer HH-pol observation
HHH-wind	Aquarius wind speed retrieved from radiometer H-pol and scatterometer HH-pol observation
H-pol	horizontal polarization
HYCOM	Hybrid Coordinate Ocean Model
I	1st Stokes parameter: I = (V+H)
IRR	Instantaneous Rain Rate
L1, L2, L3	Level 1, Level 2, Level 3
MLE	Maximum Likelihood Estimator
NCEP	National Centers for Environmental Prediction
NEDT	Noise Equivalent Delta Temperature
OT	Ocean Target
psu	practical salinity unit
Q	2nd Stokes parameter: Q = (V-H)

RA	Rain Accumulation
RFI	Radio Frequency Interference
RMS	Root Mean Squared
SMAP	Soil Moisture Active Passive
SSMIS	Special Sensor Microwave Imager and Sounder
SSS, S	Sea Surface Salinity
SST, T_S	Sea Surface Temperature
TA, T_A	Antenna Temperature(s)
$T_{A\,exp}$	Expected TA (result of geophysical model calculation)
TB, T_B	Brightness Temperature
T_{BE}	Brightness Temperature coming from the Earth only
$T_{B\,exp}$	Expected TB (result of geophysical model calculation)
$T_{B,surf}$	Brightness Temperature at the ocean surface (before surface roughness correction)
$T_{B,surf,0}$	Brightness Temperature at the flat ocean surface (after surface roughness correction)
TF	RFI-Filtered Antenna Temperature
TOA	Top of the Atmosphere
TOI	Top of the Ionosphere
U	3rd Stokes parameter = difference between +45° and -45° polarized TB
V5.0	Version 5.0
V-pol	vertical polarization

10. References

Boutin, J. et al. (2016), Satellite and In Situ Salinity: Understanding Near-Surface Stratification and Subfootprint Variability. Bull. Amer. Meteor. Soc., 97, pp 1391 – 1407, doi: 10.1175/BAMS-D-15-00032.1.

Channan, S., K. Collins and W.R. Emanuel (2014), Global mosaic of the standard MODIS land cover type date. University of Maryland and the Pacific Northwest National Laboratory, College Park, Maryland, USA.

Cox, C., and W. Munk (1954), Measurement of the roughness of the sea surface from photographs of the sun's glitter, J. Opt. Soc. Amer., 44(11), pp 838 – 850.

Didan, K., A. Barreto Munoz, R. Solano and A. Huerte (2015), MODIS Vegetation Index User's Guide (MOD13 Series) Version 3.00, Collection 6.

Dinnat, E.P. and D.M. Le Vine (2008), Impact of sun glint on salinity remote sensing: An example with the Aquarius radiometer, IEEE Transactions on Geoscience and Remote Sensing, 46(10), pp 3137 – 3150.

Dinnat, E. P., S. Abraham, D. M. Le Vine, P. de Matthaeis and D. Jacob (2009), Effect of emission from the moon on remote sensing of sea surface salinity: An example with the Aquarius radiometer, IEEE Geoscience and Remote Sensing Letters, 6(2), pp 239 – 243.

Dinnat, E. P., D. M. Le Vine, S. Abraham, and N. Floury (2010), Map of Sky Background Brightness Temperature at L-Band [Online].

Dinnat, E, D. Le Vine, J. Piepmeier, S. Brown and L. Hong (2015), Aquarius L-band radiometers calibration using cold sky, IEEE Journal of Selected Topics in Applied Earth Observations and Remote Sensing, vol. 8(12), pp 5433 – 5449.

Dinnat, E. P., and L. Brucker (2016), Improved Sea Ice Fraction Characterization for L-Band Observations by the Aquarius Radiometers, IEEE Transactions on Geoscience and Remote Sensing, doi:10.1109/TGRS.2016.2622011.

Dinnat, E. P., and D. M. Le Vine (2017), Cold Sky Calibration (CSC) Biases and Time Series with Hardware-only Wiggle Correction, presentation at the Aquarius Cal/Val Meeting, January 9 – 11, 2017, Santa Rosa, CA. Available at https://aquarius.umaine.edu/cgi/meetings.htm.

Dobson, M.C., F.T. Ulaby, M.T. Hallikainen, and M.A. El-Rayes (1985), Microwave dielectric behavior of wet soil-part II: dielectric mixing models, IEEE Transactions on Geoscience and Remote Sensing, GE-23, pp 35 – 45.

Entekhabi, D., et al. (2010), The Soil Moisture Active Passive (SMAP) Mission. Proc. IEEE, 98(5), 704-716, doi: 10.1109/JPROC.2010.2043918.

Entekhabi, D., et al. (2014), SMAP Handbook. National Aeronautics and Space Administration. [Available online at smap.jpl.nasa.gov/].

FAO/IIASA/ISRIC/ISSCAS/JRC (2012), Harmonized World Soil Database (version 1.2). FAO, Rome, Italy and IIASA, Laxenburg, Austria.

Hacker. P, O. Melnichenko, N. Maximenko, and J. Potemra (2014), Aquarius SSS Space/Time Biases with Respect to Argo Data, presentation at the Aquarius Science Team Meeting, November 12, 2014, Seattle, WA. Available at https://aquarius.umaine.edu/cgi/meetings.htm.

HYCOM (2012), The Hybrid Coordinate Ocean Model: http://hycom.org. The output used here is from Center for Ocean-Atmospheric Prediction Studies (COAPS) at Florida State University.

IOC, SCOR and IAPSO (2010), The international thermodynamic equation of seawater – 2010: Calculation and use of thermodynamic properties, Intergovernmental Oceanographic Commission, Manuals and Guides No. 56, UNESCO (English), www.teos-10.org/pubs/TEOS-10_Manual.pdf.

Isoguchi, O., and M. Shimada (2009), An L-band ocean geophysical model function derived from PALSAR, IEEE Transactions on Geoscience and Remote Sensing, 47(7), pp 1925 – 1936, doi:10.1109/TGRS.2008.2010864.

Jackson, T.J. and T.J. Schmugge (1991), Vegetation effects on the microwave emission of soils, Remote Sens. Environ. , 36, pp 203 – 212.

Joyce, R. J., J. E. Janowiak, P. A. Arkin, and P. Xie (2004), CMORPH: A method that produces global precipitation estimates from passive microwave and infrared data at high spatial and temporal resolution. J. Hydrometeorol., 5, pp 487 – 503. doi:10.1175/1525-541(2004)005<0487: CAMTPG >2.0.CO;2.

Le Vine, D. M., S. Abraham (2002) The effect of the ionosphere on remote sensing of sea surface salinity from space: Absorption and emission at L-band, IEEE Transactions on Geoscience and Remote Sensing, 40 (4), pp 771 – 782.

Le Vine, D. M., and S. Abraham (2004), Galactic noise and passive microwave remote sensing from space at L-band, IEEE Transactions on Geoscience and Remote Sensing, 42 (1), pp 119 – 129.

Le Vine, D.M., S. Abraham, F. Wentz and G.S.E. Lagerloef (2005), Impact of the sun on remote sensing of sea surface salinity from space, Proceedings of IGARSS, Seoul Korea, vol. 1, pp 288 – 291.

Le Vine, D.M., S. D. Jacob, E. P. Dinnat, P. de Matthaeis, and S. Abraham (2007a), The influence of antenna pattern on Faraday rotation in remote sensing at L-band, IEEE Transactions on Geoscience and Remote Sensing, 45(9), pp 2737 – 2746.

Le Vine, D.M, G. S. E. Lagerloef, F. R. Colomb, S. H. Yueh, and F. A. Pellerano (2007b), Aquarius: An instrument to monitor sea surface salinity from space, IEEE Trans. Geosci. Remote Sens., vol. 45, no. 7, pp. 2040 – 2050.

Le Vine, D.M., E. P. Dinnat, S. Abraham, P. de Matthaeis and F. Wentz (2011), The Aquarius Simulator and Cold Sky Calibration, IEEE Transactions on Geoscience and Remote Sensing, 49(9), pp 3198 – 3210.

Le Vine, D. and T. Meissner (2014), Proposal for Flags and Masks, AQ-014-PS-0006, February 2014.

Le Vine, D. M., S. Abraham and J. Peng (2016), Faraday Rotation Correction for the SMAP Radiometer, IEEE Transactions on Geoscience and Remote Sensing, vol. 54(4), pp. 2070-2081.

Liebe, H. J., P. W. Rosenkranz, and G. A. Hufford (1992), Atmospheric 60-GHz oxygen spectrum: New laboratory measurements and line parameters, J. Quant. Spectrosc. Radiat. Transfer, 48, pp 629 – 643.

McDougall, T.J., and P.M. Barker (2011), Getting started with TEOS-10 and the Gibbs Seawater (GSW) Oceanographic Toolbox, SCOR/IAPSO WG127, ISBN 978-0-646-55621-5, 28pp, www.teos-10.org/pubs/Getting_Started.pdf.

McDougall, T. J., and O. A. Krzysik (2015), Spiciness, J. Mar. Res., 73(5), 141-152.

Meissner, T. (2014a), Proposed APC Change from V2.0 to V3.0, RSS Technical Report 05192014.

Meissner, T. (2014b), Memo: Performance Degradation and Q/C Flagging of Aquarius L2 Salinity Retrievals, 01/20/2014, RSS Tech. Report 01202014, Version 3.

Meissner, T., and F. Wentz (2004), The complex dielectric constant of pure and sea water from microwave satellite observations, IEEE Transactions on Geoscience and Remote Sensing, vol. 42(9), pp 1836.

Meissner, T., and F. Wentz (2006), Polarization Rotation and the Third Stokes Parameter: The Effects of spacecraft attitude and Faraday rotation, IEEE Transactions on Geoscience and Remote Sensing, vol. 44(3), pp 506.

Meissner, T., and F. Wentz (2012), The emissivity of the ocean surface between 6 - 90 GHz over a large range of wind speeds and Earth incidence angles, IEEE Transactions on Geoscience and Remote Sensing, vol. 50(8), pp 3004.

Meissner, T., F. Wentz and D. Draper (2012), GMI Calibration Algorithm and Analysis Theoretical Basis Document (ATBD) Version G, report number 041912, Remote Sensing Systems, Santa Rosa, CA. [Available online at http://images.remss.com/papers/rsstech/2012_041912_Meissner_GMI_ATBD_vG.pdf].

Meissner, T., F. Wentz and L. Ricciardulli (2014), The emission and scattering of L-band microwave radiation from rough ocean surfaces and wind speed measurements from the Aquarius sensor, JGR Oceans, vol. 119, doi: 10.1002/2014JC009837.

Meissner, T., F. Wentz, J. Scott, and J. Vasquez-Cuervo (2016), Sensitivity of Ocean Surface Salinity Measurements from Spaceborne L-Band Radiometers to Ancillary Sea Surface Temperature, IEEE TGRS, vol. 54(12), pp 7105 - 7111, doi:10.1109/TGRS.2016.2596100.

Meissner, T., and F. Wentz (2016), Remote Sensing Systems SMAP Ocean Surface Salinities Level 2C, Version 2.0 validated release. Remote Sensing Systems, Santa Rosa, CA, USA. doi: 10.5067/SMP20- 2SOCS. [Available online at www.remss.com/missions/smap/salinity].

Mironov, V., L. Kosolapova, and S. Fomin (2009), Physically and mineralogically based spectroscopic dielectric model for moist soils, IEEE Transactions on Geoscience and Remote Sensing, 47(7), pp 2059 – 2070.

Misra, S. and S. T. Brown (2017), Enabling the Extraction of Climate-Scale Temporal Salinity Variations from Aquarius: An Instrument Based Long-Term Radiometer Drift Correction, IEEE Transactions on Geoscience and Remote Sensing, vol. 55 (5), pp. 2913 – 2923.

Mo, T., B. J. Choudhury, T. J. Schmugge, J. R. Wang, and T. J. Jackson (1982), A model for microwave emission from vegetation-covered fields, Journal of Geophysical Research: Oceans, vol. 87(C13), pp. 11229-11237.

O'Neill, P., S. Chan, E. Njoku, T. Jackson, and R. Bindlish (2015), Soil Moisture Active Passive (SMAP) Algorithm Theoretical Basis Document, Level 2 & 3 Soil Moisture (Passive) Data Products, Revision B, September 14, JPL D-66480, http://smap.jpl.nasa.gov/cal-val-data/.

Patton, J. and B. Hornbuckle (2014), Comparison of SMOS-retrieved and NDVI climatology-derived vegetation optical thickness, 2014 IEEE Geoscience and Remote Sensing Symposium, Quebec City, QC, pp. 2554-2557.

Pawlowicz, R. (2010), What every oceanographer needs to know about TEOS-10 (The TEOS-10 Primer, Web document, http://www.teos-10.org/pubs/TEOS-10_Primer.pdf.

Pellarin, T., et al. (2003), Two-year global simulation of L-band brightness temperatures over land, IEEE Transactions on Geoscience and Remote Sensing, vol. 41(9), pp 2135 – 2139 .

Preston-Thomas, H. (1990), The International Temperature Scale of 1990 (ITS-90). Metrologia, 27(1), pp 3 – 10, http://www.omega.com/temperature/z/pdf/z186-193.pdf.

Piepmeier, J. (2004), Calibration of passive microwave polarimeters that use hybrid coupler-based correlators, IEEE Transactions on Geoscience and Remote Sensing, vol. 43(2), pp 391 – 400.

Piepmeier, J., D. Long, and E. Njoku (2008), Stokes Antenna Temperatures, Transactions on Geoscience and Remote Sensing, vol. 46(2), pp 516 – 527.

Piepmeier, J., P. Mohammed, J. Peng, E. J. Kim, G. De Amici, and C. Ruf (2016), SMAP L1B Radiometer Half-Orbit Time-Ordered Brightness Temperatures, Version 3. [RFI-filtered antenna temperatures], Boulder, Colorado USA. [Available online at NASA National Snow and Ice Data Center Distributed Active Archive Center, http://dx.doi.org/10.5067/YV5VOWY5V446].

Piepmeier, J., F. Pellerano, B. Wilson and S. Yueh (2005), Aquarius Algorithm Theoretical Basis Document: Calibrated Antenna Temperatures.

Randa, J. et al., (2008), Recommended terminology for Microwave Radiometry, NIST Technical Note 1551, U.S. Gov. Printing Office.

Rienecker, M. M., R. Todling, J. Bacmeister, L. Takacs, H.C. Liu, W. Gu, M. Sienkiewicz, R.D. Koster, R. Gelaro, and I. Stajner, (2008), The GEOS-5 Data Assimilation System-Documentation of Versions 5.0. 1, 5.1. 0, and 5.2. 0., NASA Technical Report.

Rosenkranz, P. (1998), Water vapor microwave continuum absorption: A comparison of measurements and models, Radio Science, 33(4), pp 919 – 928.

Santos-Garcia, A., H. Ebrahimi, Y. Hejazin, M. M. Jacob, W. L. Jones, and W. Asher (2014a), Application of the AQ rain accumulation product for investigation of rain effects on AQ Sea Surface Salinity measurements. Microwave Radiometry and Remote Sensing of the Environment (MicroRad), 2014 13th Specialist Meeting on, (pp. 72-77). Pasadena, CA. Doi:10.1109/MicroRad.2014.6878911.

Santos-Garcia, A., M. M. Jacob, W. L. Jones, W. Asher, Y. Hejazin, H. Ebrahimi, and M. Rabolli (2014b), Investigation of rain effects on Aquarius Sea Surface Salinity measurements. J. Geophys. Research Oceans, 119, 7605-7624. doi:10.1002/2014JC010137.

Santos-Garcia, A., M. M. Jacob, and W. L. Jones (2016), SMOS Near-Surface Salinity Stratification Under Rainy Conditions. IEEE Journal of Selected Topics in Applied Earth Observations and Remote Sensing, 1-7. doi:10.1109/JSTARS.2016.2527038.

Ulaby, F.T., R.K. Moore and A.K. Fung (1986), Microwave Remote Sensing: Active and Passive, Volume I, II, and III, Artech Inc., Norwood.

UNESCO (1981), The Practical Salinity Scale 1978 and the International Equation of State of Seawater 1980. UNESCO technical papers in marine science 36, http://www.jodc.go.jp/info/ioc_doc/UNESCO_tech/046148eb.pdf.

Wang, J.R. and B.J. Choudhury (1981), Remote Sensing of Soil Moisture Content Over Bare Field at 1.4 GHz Frequency, J. Geophys. Research, vol. 86, C6, pp 5277 – 5282.

Wentz, F. J. (1978), The forward scattering of microwave solar radiation from a water surface, Radio Science 13 (1), pp 131 – 138.

Wentz, F. J. (1983), A model function for ocean microwave brightness temperatures, J. Geophys. Res., vol. 88, pp 1892 – 1908.

Wentz, F. (1991), A simplified wind vector algorithm for satellite scatterometers, J. Atmos. Oceanic Technol. 8(5), pp 697 – 704, doi: http://dx.doi.org/10.1175/1520-0426(1991)008<0697:ASWVAF>2.0.CO;2.

Wentz, F. J. (2005), Simulation of Solar Contamination for Aquarius, RSS Technical Report 060305.

Wentz, F. J. (2006), The Estimation of TOA T_B from Aquarius Observations, RSS Technical Report 013006.

Wentz, F. J. (2007), Update to Simulation of Solar Contamination for Aquarius: Results from Scale-Model Antenna Patterns, RSS Technical Report 020907.

Wentz, F. J. and T. Meissner (2000), Algorithm Theoretical Basis Document (ATBD), Version 2, AMSR Ocean Algorithm, RSS Tech. Report 121599A-1.

Wentz, F. J. and D. M Le Vine (2011), Algorithm Theoretical Basis Document (ATBD), Aquarius Salinity Retrieval Algorithm: Final Pre-Launch Version, RSS Tech. Report 011811, January 18, 2011.

Wentz, F.J., K.A. Hilburn, and D.K. Smith (2012), Remote Sensing Systems DMSP [SSM/I or SSMIS, Environmental Suite on 0.25 deg grid, Version 7. Remote Sensing Systems, Santa Rosa, CA. Available online at www.remss.com/missions/ssmi.

Wentz, F.J., L. Ricciardulli, C. Gentemann, T. Meissner, K.A. Hilburn, J. Scott (2013), Remote Sensing Systems Coriolis WindSat, Environmental Suite on 0.25 deg grid, Version 7.0.1. Remote Sensing Systems, Santa Rosa, CA. Available online at www.remss.com/missions/windsat.

Wentz, F., and T. Meissner (2016), Atmospheric Absorption Model for Dry Air and Water Vapor at Microwave Frequencies below 100 GHz Derived from Spaceborne Radiometer Observations, Radio Sci., 51, doi:10.1002/2015RS005858.

Wilheit, T.T., and A. T. C. Chang (1980), An algorithm for retrieval of ocean surface and atmospheric parameters from the observations of the scanning multichannel microwave radiometer, Radio Science, 15(3), pp 525 – 544.

Yueh, S. (2000), Estimates of Faraday rotation with passive microwave polarimetry for microwave remote sensing of Earth surfaces, IEEE Transactions on Geoscience and Remote Sensing, vol. 38(5), pp 2434 – 2438.

Yueh, S., S. Dinardo, A. Fore, and F. Li (2010), Passive and active L-band microwave observations and modeling of ocean surface winds, IEEE Transactions on Geoscience and Remote Sensing, 48(8), pp 3087 – 3100, doi:10.1109/36.752213.

Yueh, S. et al. (2013), Aquarius Scatterometer Algorithm Theoretical Basis Document, [Avail at JPL PO.DAAC: http://podaac.jpl.nasa.gov/aquarius].

11. Acknowledgements

We acknowledge the help from several members of the Aquarius Cal/Val team with writing this ATBD:

Emmanuel Dinnat (Section 4.7 and Appendix B), Joel Gales (Appendix B), Liang Hong (Sections 7.1.3, 7.1.4 and Appendix B), Andrea Santos Garcia (Section 4.9), Julian Schanze (Appendix C) and Yan Soldo (Appendix B).

Appendix A. Scatterometer Model Function $\sigma_{0,p}^{GMF}(W,\varphi_r)$

The geophysical model functions for the scatterometer σ_0 can be expanded into a Fourier series of even harmonic functions in the relative wind direction, φ_r (Wentz, 1991; Isoguchi and Shimada, 2009; Yueh et al. 2010). Keeping terms up to 2nd order:

$$\sigma_{0,p}^{GMF}(W,\varphi_r) = B_{0,p}(W) + B_{1,p}(W)\cdot\cos(\varphi_r) + B_{2,p}(W)\cdot\cos(2\cdot\varphi_r) \qquad (103)$$

where W is the surface wind speed and p =VV, HH, VH, HV is the scatterometer polarization. The coefficients, $B_{k,p}$ depend on incidence angle and polarization and therefore are different for each scatterometer channel. The harmonic coefficients $B_{k,p}(W)$ are expressed as a 5th order polynomial in W:

$$B_{k,p}(W) = \sum_{i=1}^{5} b_{ki,p}\cdot W^i \qquad (104)$$

where the sum runs over i = {1…5}. In (103) the wind direction, $\varphi_r = \varphi_W - \alpha$ where φ_W is the geographical wind direction relative to North and α is the azimuthal direction. An upwind observation has $\varphi_r = 0°$, a downwind observation has $\varphi_r = 180°$ and crosswind observations have $\varphi_r = +/- 90°$. The value for φ_w comes from the ancillary NCEP GDAS field.

The coefficients $b_{ki,p}$ {i=1, ...5} , k={0,1,2} p={VV,HH} were empirically determined in Meissner et al. 2014 from a match-up data set consisting of the Aquarius scatterometer $\sigma_{0,VV}$ observations and wind speed measurements from WindSat (Wentz et al. 2012) and F17 SSMIS (Wentz et al. 2012). Formatted ASCII files for the coefficients $b_{ki,p}$ are provided in the supplementary files (Appendix D).

For each $B_{k,p}$ there is a maximum wind speed $W_{k,p}^{\max}$ above which the values of $B_{k,p}(W)$ are calculated by linear extrapolation instead of equation (104). The values of $W_{k,p}^{\max}$ are also listed in the supplementary files (Appendix D).

Appendix B. Surface Brightness Temperatures over Land and Frozen Surfaces

This appendix briefly summarizes the computation of TB for land and frozen surfaces. The emissivity model has been revised for V5.0. The changes were made to bring the model closer to that used by SMAP. The description below applies to V5.0 and not to earlier versions.

General Approach

When the scene is not entirely ocean (i.e., land fraction + ice fraction >= 0.002), the following expressions are used:

$$T_B = f_{water} \cdot E_{P,water} \cdot T_{water} + f_{sea\_ice} \cdot R_{P,sea\_ice} \cdot T_{sea\_ice} + f_{land} \cdot R_{P,land} \cdot T_{land} + f_{frozen\_land} \cdot R_{P,\,frozen\_land} \cdot T_{frozen\_land} \quad (105)$$

Here, R denotes the reflectivity, f denotes the fractional area weighted by the antenna pattern, E the emissivity and T_S the thermodynamic temperature at the surface. The subscript P denotes the polarization.

The surface temperatures over land are from GEOS version 5.12.4 (Rienecker et al., 2008) and the distribution of sea ice is from NCEP.

Land and water are separated using the same 1 km land mask as employed in Section 4.6 of the main text of this ATBD to compute g_{land} . Then the surface temperature is used to separate each pixel defined as land into frozen (f_{frozen_land}) and non-frozen(f_{land}) portions. Land is defined to be frozen when the surface temperature is < 0 ^{o}C. That is, $f_{land\_tot} = f_{land} + f_{frozen\_land}$. Finally, the fraction of water is defined as $f_{water} = f_{land\_tot} - f_{sea\_ice}$.

Emissivity

The emissivity in (105) is given in terms of the surface reflectivity R , in the form $E_P = 1 - R_P$.

In the case of a "flat" surface (i.e. no roughness) the reflectivity is given by the Fresnel reflection coefficients and the dielectric constant of the material (e.g. land or water) in the form:

$$R_V = \left| \frac{\varepsilon \cos\theta - \sqrt{\varepsilon - \sin^2\theta}}{\varepsilon \cos\theta + \sqrt{\varepsilon - \sin^2\theta}} \right|^2$$
$$R_H = \left| \frac{\cos\theta - \sqrt{\varepsilon - \sin^2\theta}}{\cos\theta + \sqrt{\varepsilon - \sin^2\theta}} \right|^2 \quad (106)$$

where ε is the dielectric constant and θ the incidence angle computed at the location of the antenna boresight.

Water

The dielectric constant of ocean is as described in detail in the ATBD. Non-ocean water bodies are treated same as ocean and, when not defined, salinity is assumed equal to 35 psu. NCEP winds are then used to account for the surface roughness (see Section 5 of the ATBD main text).

Sea Ice

The dielectric constant of sea ice is set to:

$$\varepsilon = 3 - i \quad (107)$$

which is based on data for freshwater ice (Ulaby et al. 1986, pp 2026-2027). This is used in (106) to compute the corresponding reflectivity. Snow and roughness are not taken into account.

Land

The model uses the land cover classification provided by MODIS-IGBP products (Channan et al., 2014). The dielectric constant is obtained using the Mironov dielectric mixing model (Mironov et al. 2009) and the soil characteristics provided by HWSD (Harmonized World Soil Database) (FAO, 2012). The dielectric constant is then used in equations (106) to obtain the reflectivity of a smooth surface.

The effect of roughness is to decrease the reflectivity of the smooth surface. This effect is modeled through the following relationship (Wang and Choudhury, 1981; Pellarin et al., 2003):

$$R_{P,rough} = R_p \cdot e^{-h} \quad (108)$$

where h is an empirical value related to the roughness of the surface and R_p is from (106). The values of h depend on the land cover class, and they are set equal to the values used by the SMAP mission (O'Neill et al. 2015, SMAP ATBD L2&3 Passive, version 4.0, Table 3).

The vegetation canopy attenuates the radiation emitted from soil and emits its own radiation. The effect of vegetation is modeled with the tau-omega model (Mo et al., 1982), which assumes that the vegetation is a homogeneous layer with negligible scattering overlying the soil layer. The equation is given by (Jackson and Schmugge, 1991):

$$R_{P,obs} = 1 - (1-\omega)\cdot(1-\gamma)\cdot(1+R_{P,rough}\gamma) - (1-R_{P,rough})\cdot\gamma \tag{109}$$

where ω is the vegetation single-scattering albedo and γ is the vegetation transmissivity, which is defined as:

$$\gamma = e^{-\tau\cdot\sec(\theta)} \tag{110}$$

θ is the incidence angle, and τ_{veg} the vegetation opacity. Jackson and Schmugge (1991) have shown that the vegetation opacity depends on the vegetation water content (W) and on the vegetation structure. This dependency is expressed in the form:

$$\tau_{veg} = b\cdot W \tag{111}$$

where b is a coefficient that depends on the vegetation type. The values of b and ω depend on the land cover class and they are set equal to the values in Table 3 of the SMAP ATBD L2&3 Passive, version 4.0. The estimation of the vegetation water content is done from MODIS NDVI retrievals (Didan et al., 2015) following equation (1) in Patton and Hurnbuckle (2014).

Frozen Land

Observations have shown that the freezing of soil substantially changes its reflectivity and for this reason it is treated separately from non-frozen land. However, the dielectric constant of frozen soil, snow and ice are difficult to model, in part because the penetration depth increases significantly in dry conditions.

From Aquarius measurements it can be seen that although the reflectivity of frozen soils depends on the geographic location, time and temperature do not have a significant impact, as long as the surface remains frozen. The approach adopted for V5.0 to obtain a realistic estimate of the soil reflectivity in frozen conditions, is to use the Aquarius observations themselves. In particular, (2) was applied to all 4 years of Aquarius measurements to obtain the emissivity of frozen land. The retrieved emissivities were then averaged and displayed in global maps with 1x1 degree resolution. Each map corresponds to one channel and included the entire duration of the mission (the retrieved emissivities are very stable in time). Figure 28 shows the retrieved emissivities for beam1 and V-pol. The data for all channels (3 beams and two polarizations) exists in static lookup tables in the code.

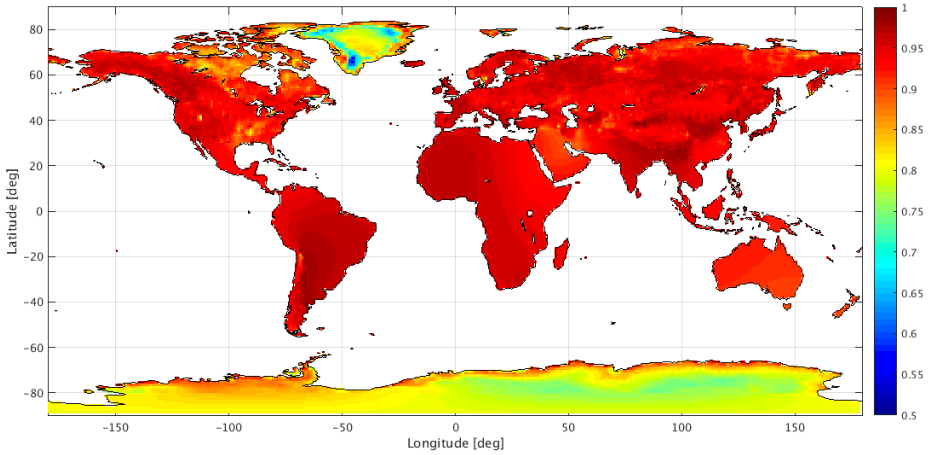

Figure 28: Map of the average retrieved emissivities of frozen land surfaces. A linear interpolation has been used to fill empty cells (where freezing never occurs).

Some grid cells had very few footprints with temperatures lower than -2°C. To avoid averaging (drop in a bucket) the retrieved emissivities using too few samples, averages were made only if there were at least 5 footprints with temperatures lower than -2°C. This created some empty grid cells. To fill the voids, a linear interpolation that relies on the grid cells with valid averages was employed. From a coding point of view, computing the interpolation on all the empty grid cells was less time-consuming than selecting the grid cells that had less than 5 footprints. Hence, the maps show emissivity for all land cells, but these values are only used in those cells when the surface temperature is below 0° C.

Propagation to the Sensor: Atmosphere and Ionosphere

The atmosphere attenuates the emissions for the ground. Its effect is accounted for as spelled out in the forward model (Section 2.3.2, equation (26)).

The Faraday rotation in the Earth's ionosphere is treated as described in Section 3.4. However, a change is necessary in the treatment of Faraday rotation over land. Over the ocean, the Faraday Rotation Angles (FRA) retrieved from Aquarius measurements are accurate enough to estimate the effect of the ionosphere in the forward model. However, over land, the FRA retrievals are much noisier (e.g. Le Vine et al., 2016). For this reason, when the water fraction in the footprint is lower than 0.998 (which corresponds roughly to 100-130 km away from the coastline), the FRA for the forward model is obtained from theory (Le Vine and Abraham, 2002) using the Earth magnetic field (Barton, 1997) and IGS TEC (http:// www.igs.org).

Appendix C. Density and Spiciness

The V5.0 Aquarius L2 files contain a value for water density and spiciness.

Density is a highly non-linear derived variable which depends on temperature, salinity, and pressure. With the introduction of the Thermodynamic Equation of State in 2010 (TEOS-10), a new thermodynamically consistent formulation of temperature, salinity and density (amongst other variables) was introduced (IOC et al. 2010). TEOS-10 has been accepted by the Intergovernmental Oceanographic Commission and UNESCO to replace the previously used UNESCO Equation of State 1980 (EOS-80) (UNESCO 1981). TEOS-10 introduces a number of new variables that are required for the computation of density from *in-situ* measurements. The two relevant variables for the purposes of computing surface density from Aquarius Sea Surface Salinity (SSS) and the ancillary Sea Surface Temperature (SST) fields are Absolute Salinity (S_A) and Conservative Temperature (Θ).

Thus, to determine surface density from Aquarius-derived and ancillary data fields, S_A and Θ have to be computed prior to calculating the density. It should be noted that while S_A should be used in all scientific publications involving salinity, it is not recommended for archival purposes. For this reason, Aquarius data will continue to be distributed as practical salinity (S_P) as defined by the Practical Salinity Scale (PSS-78) (UNESCO 1981).

Conservative Temperature (Θ) is similar to potential temperature in EOS-80, but is designed to be conserved both under adiabatic mixing and changes in depth (IOC et al., 2010), which is fulfilled neither by potential or *in-situ* temperature. Absolute Salinity (S_A) is a true mass fraction, and defined as the mass fraction of the solute in standard seawater with a density that is identical to the sample. Consequently, S_A has units of g kg^{-1}. These definitions are explained in more detail in IOC et al. (2010) as well as in Pawlowicz (2010).

All computations are performed using the Gibbs-Seawater (GSW) Oceanographic Toolbox (McDougall and Barker 2011) V3.03 for *C*. In the first step, S_A is computed from S_P using the subroutine *gsw_sa_from_sp*, which requires four inputs, S_P, pressure, longitude and latitude. In the next step, Θ is computed from sea surface temperature (ITS-90, Preston-Thomas 1990) using the subroutine *gsw_ct_from_t*, which requires S_A, pressure, and temperature as inputs. Having computed all required input variables, density is then determined using the subroutine *gsw_rho*, which

requires S_A, Θ, and pressure as input variables. In all these computations, pressure is fixed to a value of 0, as pressure is defined relative to atmospheric pressure.

Spiciness is variable derived from density which is designed to maximize the contrast between water masses of equal density. The name spiciness arose from the notion that warm and salty water is 'spicy', while cold and fresh water is 'bland'. While the increase of spiciness due to increasing salinity is analogous to the increase of density due to increasing salinity, spiciness is also increased by increasing temperature, unlike density, where this effect is negative. It is thus a useful tracer of water masses, particularly in areas of high freshwater content, but also in salinity maximum areas.

The definition used for spiciness is taken from (McDougall & Krzysik, 2015) and implemented using the Gibbs-Seawater (GSW) Oceanographic Toolbox (McDougall and Barker, 2011) V3.05 for C. Using this toolbox, spiciness is computed using the function *gsw_spiciness_0*, which requires two inputs, Absolute Salinity (S_A) and Conservative Temperature (Θ). The fields of S_A and Θ which were derived in the computation of density in Section **6.** are used for the computation of spiciness. No pressure term is needed, as the function *gsw_spiciness_0* is defined for the ocean surface at 0m depth.

Appendix D. Supplementary Files for Surface Roughness Correction

The supplementary files include table in ASCII format containing various coefficients that enter the geophysical model function of the wind induced emissivity and the ancillary Aquarius wind speed retrievals (Section 5 and Appendix A).

1. ATBD_supplement_1.txt: The coefficients b_{ki} of the 5th order polynomial fit to the harmonic coefficients of the scatterometer GMF (Appendix A). k=0,1,2 indicates the order of the harmonic and i=1, … ,5 the order of the power in the polynomial. The values are provided for all 3 radiometers and polarizations VV, HH, and VH. The value for i=1…,5 is the 1st column and the value for b_{ki} is the 2nd column. At the end of file, the values of the maximum wind speeds $W_{k,p}^{\max}$ are listed, above which linear extrapolation is used.
2. ATBD_supplement_2.txt: The coefficients a_{ki} of the 5th order polynomial fit to the harmonic coefficients of the wind induced emissivity GMF (Section 5.1.2). k=0,1,2 indicates the order of the harmonic and i=1, … ,5 the order of the power in the polynomial. The values are provided for all 3 radiometers and V-pol and H-pol. The value for i=1…,5 is the 1st column and the value for a_{ki} is the 2nd column. At the end of file, the values of the maximum wind speeds $W_{k,p}^{\max}$ are listed, above which linear extrapolation is used.
3. ATBD_supplement_3.txt: Tabulated values for the SST dependence of $\rho'(T_S)$ in Section 5.1.3 equation (59) for all Aquarius channels. The units are dimensionless.
4. ATBD_supplement_4.txt: The correction $\Delta E_{W1}(W_{HHH}, \sigma'_{0VV})$ to the wind induced emissivity (Section 5.1.4). The values are provided for all 3 radiometers and polarizations V-pol and H-pol. The 1st column is the HHH wind speed W_{HHH} [in m/s]. The 2nd column is the scatterometer VV-pol cross section σ'_{0VV} after removing the wind direction signal [in real units]. The 3rd column is the number of observation in each bin. The 4th column is the value of ΔE_{W1} for v-pol (times 290 K). The 5th and last column is the value of ΔE_{W1} for h-pol (times 290 K). If the values of W or $\sigma'_{0,VV}$ fall outside the values listed in the table, then the value of ΔE_{W1} is set to the lowest or highest end listed in the table, respectively.
5. ATBD_supplement_5.txt: Expected errors for the channels (scatterometer HH and radiometer H-pol) that are used in the MLE as a function of surface wind speed (Section 5.2). The 1st column is the wind speed. The next 3 columns are the expected standard deviations of σ_{0HH} [in real units], T_{BH} [in K] and the NCEP background wind speed W_{NCEP} (in m/s) for radiometer 1, 2 and 3, respectively.